

COMPUTER-AIDED DESIGN OF AXIAL GAS TURBINE METER BLADES

by

Cem Günaydın

B.S., in M.E., Boğaziçi University, 2003

Submitted to the Institute for Graduate Studies in
Science and Engineering in partial fulfillment of
the requirements for the degree of
Master of Science

Graduate Program in Mechanical Engineering
Boğaziçi University

2006

ACKNOWLEDGEMENTS

I would like to express my deepest gratitude to Dr. Haluk Örs for supervising my thesis, and his invaluable guidance above all.

Thanks to Dr. Osman Börekçi and Dr. Kunt Atalık for accepting to be in the committee and the valuable time they spent for this thesis.

I also would like to thank Kale Kalıp A.Ş. for their support and broadening my view of turbine meters by the data they provide. Special thanks to Yiğit Erzan for his valuable support, interest and his friendly attitude.

I can not forget the contributions of Selim Sancı with his comments and thinking way. Server Levent Yılmaz has provided me with very important sources, I am also very thankful to him.

I would like to thank my friends and my family for their encouragement and trust throughout my study.

ABSTRACT

COMPUTER-AIDED DESIGN OF AXIAL GAS TURBINE METER BLADES

Designing a gas turbine meter (GTM) to maintain certain levels of performance features is usually done by manufacturing and testing prototypes in experimental set-ups. However an experimentally supported Computational Fluid Dynamics (CFD) analysis may drastically reduce the cost and time in the design process of GTMs.

One of the most important design parameters effecting the performance of GTMs is the blade geometry. Many variables may be defined in the geometry of the blades. Blade pitch angle, number of blades and the tip clearance are the three essential design variables studied in this thesis considering the results from CFD tools such as Fluent.

Firstly blade pitch angle and number of blades are taken as design variables for different design approaches. Then the chosen blade shape is improved regarding the tip clearance and trailing edge shape; afterwards the final GTM is linearized according to the different Reynolds numbers.

OptGTM3D, which is a user-interface Matlab computer program capable of commanding Gambit and Fluent for GTM blade design, is written. A methodology which is also quite demanding in problems involving rotating parts and flow induced torque, is adapted into this program for externally converging the moment coefficient in Fluent to find the angular speed for specified flow rates. Producing geometry and mesh, running it in Fluent is automatically done through OptGTM3D for the specified geometries. The geometry is generated as a volume around one blade in Gambit and run in Fluent by making use of Multiple Rotating Reference Frame to save computational time.

ÖZET

YATAY EKSENLİ GAZ TÜRBİN SAYAÇ PALALARININ BİLGİSAYAR DESTEKLİ TASARIMI

Belirli performans özelliklerini sağlayacak gaz türbin sayaçlarının tasarımı genelde, üretilen prototiplerin deneysel düzeneklerde test edilmesi sonucu yapılır. Halbuki deneysel olarak desteklenmiş bir Hesaplamalı Akışkanlar Dinamiği analizi gaz türbin sayaç tasarımında harcanan para ve zamanı büyük ölçüde azaltabilir.

Türbin metrelerin performansını etkileyen en önemli dizayn parametrelerinden biri palaların geometrisidir. Palaların geometrisinde birçok değişken tanımlanabilir. Bu tezde palaların açısı, pala sayısı ve pala uç toleransı; Fluent gibi Hesaplamalı Akışkanlar Dinamiği araçlarıyla elde edilen sonuçlar dikkate alınarak incelenmiştir.

İlk olarak pala açısı ve sayısı değişken alınarak değişik dizayn yaklaşımları kullanılıp bir pala şekli seçilmiştir. Sonrasında seçilen pala şekli, pala uç toleransı ve pala arka uç şekli dikkate alınarak geliştirilmiş ve elde edilen türbin sayacının farklı Reynolds sayıları için linearizasyonu yapılmıştır.

Gaz türbin sayaç palalarının tasarımına yönelik, kullanıcı arayüzüne sahip, OptGTM3D isimli, Fluent ve Gambit'i yönetebilen bir Matlab bilgisayar kodu yazılmıştır. Akıştan dolayı oluşan torkla dönen katıları içeren problemlerde çokça istenen bir metod bu programa adapte edilmiş ve böylece sabit akış debilerinde açısal hızı bulmak için Fluent'teki moment katsayısı dışardan yakınsatılmıştır. Geometriyi oluşturmak, gridlere bölmek, sonrasında elde edilen sonucu Fluent'te çalıştırmak OptGTM3D tarafından belli geometriler için otomatik olarak yapılmaktadır. Geometri tek bir pala etrafında hacim olarak Gambit'te modellenip, hesaplama zamanını azaltmak için Fluent'te Multiple Rotating Reference Frame modeliyle çalıştırılmaktadır.

TABLE OF CONTENTS

ACKNOWLEDGEMENTS	iii
ABSTRACT	iv
ÖZET	v
LIST OF FIGURES	x
LIST OF TABLES	xv
LIST OF SYMBOLS/ABBREVIATIONS	xviii
1. INTRODUCTION	1
1.1. Objective	1
1.2. Flow Measurement History	3
1.2.1. Historical Development of Turbine Meters	6
1.3. Classification of Flowmeters	8
1.3.1. Turbine Flowmeter Types	10
1.3.1.1. Precision liquid meters	10
1.3.1.2. Gas Turbine Meter	10
1.3.1.3. Water Meters	11
1.3.1.4. Dual Rotor Turbine Meter	11
1.3.1.5. Quantum Dynamic Flowmeter	12
1.3.1.6. Spirometer	12
1.3.1.7. Pelton Wheel (Multijet Turbine Flowmeter)	12
1.3.1.8. Insertion Axial Turbine Meter	12
1.3.1.9. Paddle Wheel Flowmeter	13
2. Gas Turbine Meter	14
2.1. Operating Principle	14
2.2. General Performance Characteristics	15
2.3. Calibration	16
2.3.1. Frequency vs. Flowrate	18
2.3.2. K Factor vs. Flowrate	18
2.3.3. Universal Viscosity Curve	19
2.3.4. K-Factor vs. Reynolds number	20

2.3.5.	Strouhal Number vs. Reynolds Number	20
2.4.	Flow Straighteners and Flow Conditioners:	23
2.5.	Design and Construction	26
2.6.	Standards	30
2.7.	Installation and Maintenance	31
3.	Theory	33
3.1.	Basic Flow Phenomena	33
3.1.1.	Drag	33
3.1.1.1.	Pressure Drag	35
3.1.1.2.	Friction Drag	36
3.1.2.	Basics of The Boundary Layer Theory	37
3.1.2.1.	Linear Sublayer	38
3.1.2.2.	Log-law layer	39
3.1.2.3.	Outer layer	39
3.1.3.	Secondary Flows	40
3.1.4.	Separation and Wake	41
3.1.5.	Stall	42
3.1.6.	Tip Leakage Flow	42
3.2.	Turbine Meter Theories	43
3.2.1.	Ideal Gas Turbine Meter	44
3.2.2.	Momentum Theory	45
3.2.3.	Airfoil Theory	49
3.3.	Governing Equations of Fluid Dynamics	51
3.3.1.	Navier-Stokes Equations	53
3.3.2.	General Transport Equations	54
4.	Numerical Simulation Approach	56
4.1.	CFD	56
4.1.1.	Spatial Discretisation	56
4.1.1.1.	Finite Difference	57
4.1.1.2.	Finite Element	57
4.1.1.3.	Finite Volume	58
4.1.2.	Grid Generation	58

4.1.2.1.	Structured Grid	58
4.1.2.2.	Unstructured Grid	59
4.2.	GTM Model	60
4.3.	Gambit as a Preprocessor	63
4.4.	Fluent as a Solver	66
4.4.1.	Rotating Reference Frames	68
4.4.1.1.	Multiple Reference Frame Model	70
4.4.1.2.	Mixing Plane Model	71
4.4.1.3.	Sliding Mesh Model	72
4.4.2.	The Flow Model in Fluent	72
5.	Validation of Numerical Simulations	75
5.1.	Numerical Simulation of a Turbine Meter in Air Flow	75
5.1.1.	The Numerical Simulations	78
6.	The Computational Tool OptGTM3D	86
6.1.	Pre-Processor (Gambit)	87
6.2.	Solver (Fluent)	89
6.3.	Post-Processor	92
7.	Design of GTM	93
8.	Conclusion	107
8.1.	Suggestions for Further Study	108
APPENDIX A:	Flow Meter Specification Terms	110
A.1.	Accuracy	110
A.2.	Rangeability	110
A.3.	Linearity	111
A.4.	Repeatability	112
A.5.	Hysteresis	112
A.6.	Meter Factor	112
APPENDIX B:	Discretization in Fluent	113
B.1.	First Order Upwind Scheme	114
B.2.	Second Order Upwind Scheme	114
B.3.	Under-Relaxation	115
B.4.	Pressure Interpolation Schemes	115

APPENDIX C: Turbulence Modeling in Fluent	117
C.1. Reynolds (Ensemble) Averaging	118
C.2. The $k-\epsilon$ Model	120
C.2.1. The Realizable $k-\epsilon$ Model	120
C.3. Wall Treatment	123
C.3.1. Standard Wall Functions	123
C.3.2. Non-Equilibrium Wall Functions	123
C.3.3. Enhanced Wall Treatment	124
REFERENCES	125

LIST OF FIGURES

Figure 1.1.	World natural gas consumption [1]	1
Figure 1.2.	Turkey’s natural gas network [4]	2
Figure 1.3.	Egyptian and Roman form of Archimedean [5]	4
Figure 1.4.	Roman pipe installation [5]	5
Figure 1.5.	Sketch by Leonardo of flow over a contacted weir [5]	6
Figure 1.6.	Horizontal mill [5]	7
Figure 1.7.	Endress & Hauser corrosion-resistant meter design [8]	10
Figure 1.8.	Gas and Water Meter Manufacturers Ltd meter [8]	11
Figure 1.9.	Quantum Technology meter [5]	12
Figure 1.10.	Pelton Wheel Meter by Data Industrial Corporation [8]	13
Figure 2.1.	Gas Turbine Meter [14]	14
Figure 2.2.	Schematic view of a GTM components: flow conditioner (1), flow channel (2), turbine rotor blading (3), flow ring (4), gear train (5), magnetic coupling (6), counter (7) [15]	15
Figure 2.3.	Maximum allowable error and characteristic of an Instromet Gas Meter [8]	17

Figure 2.4.	Calibration curve for a low-viscosity fluid with principal alternative presentations [12]	17
Figure 2.5.	Frequency vs. flowrate for different viscosities [17]	18
Figure 2.6.	K Factor vs. flowrate diagram [18]	18
Figure 2.7.	Universal viscosity calibration [5]	19
Figure 2.8.	Strouhal number vs. Reynolds number [19]	20
Figure 2.9.	Meter calibration results [5]	23
Figure 2.10.	Flow profiles for different Reynolds numbers [21]	25
Figure 2.11.	Effect of a single elbow on the profile [7]	26
Figure 2.12.	Some types of devices used for improving flow profiles [5]	27
Figure 2.13.	Velocity profile approaching the blade [5]	28
Figure 2.14.	Rotor rpm vs. flowrate [9]	29
Figure 2.15.	Piping configuration to test the sensitivity for installation conditions. [5]	32
Figure 3.1.	Forces from the surrounding fluid on a two dimensional object a)pressure force b)viscous force c) resultant force (lift and drag) [25]	34
Figure 3.2.	Pressure and shear forces on a small element of the surface of a body [25]	35

Figure 3.3.	Secondary flow and its formation [27]	40
Figure 3.4.	Effect of trailing edge on calibration [8]	42
Figure 3.5.	Flow past progressively more streamlined bodies [28]	43
Figure 3.6.	Vector diagram for a flat-bladed axial turbine rotor [12]	44
Figure 3.7.	General view of a turbine rotor and torques on the rotor [23]	47
Figure 3.8.	Cascade angles, dimensions and forces [23]	49
Figure 3.9.	General transport equation: balance of flows [34]	55
Figure 4.1.	Transformation from physical to computational domain [40]	59
Figure 4.2.	Structured grid in 2D [40]	59
Figure 4.3.	Unstructured grid in 2D [41]	60
Figure 4.4.	Main components of the GTM model provided from the industry	61
Figure 4.5.	A closer look to the provided rotor model and the conditioners around it. (16 twisted blades with 30 degrees blade pitch angle)	62
Figure 4.6.	Cell types available in Gambit	64
Figure 4.7.	GTM model in Gambit	65
Figure 4.8.	Basic program structure [41]	67
Figure 4.9.	a) Segregated solver structure b) Coupled solver structure [41]	68

Figure 4.10.	Coordinate system for relative velocity [41]	69
Figure 5.1.	Schematic lay out of the experimental set-up for air flow [42]	75
Figure 5.2.	Turbine flow meter with tube type straightener [42]	76
Figure 5.3.	Characteristics of the turbine meter for undisturbed flow conditions [42]	77
Figure 5.4.	Pressure drop across turbine meter for undisturbed flow conditions. [42]	78
Figure 5.5.	Volume around one blade used in the numerical simulation	79
Figure 5.6.	Volumes generated in the numerical model for meshing purposes . . .	80
Figure 5.7.	Volume meshed with 590816 hexahedral elements and the boundary layer	81
Figure 5.8.	Flowrate vs. K-factor plot for realizable $k-\epsilon$ model	84
Figure 5.9.	Velocity contours at the inlet for 465 Pa pressure inlet	85
Figure 5.10.	Velocity contours at the inlet for 20 Pa pressure inlet	85
Figure 6.1.	Pre-processor part of OptGTM3D	89
Figure 6.2.	Solver part of OptGTM3D	91
Figure 6.3.	Post-processor part of OptGTM3D	92
Figure 7.1.	A part of the moment convergence plot for a 12 bladed rotor	95

Figure 7.2. The comparison of the flowrate vs. K-factor plots for different blade pitch angles for the 16 bladed rotor 98

Figure 7.3. The comparison of the flowrate vs. K-factor plots for different blade numbers for the blade pitch angle of 30° 100

Figure 7.4. The velocity profile for a 12-bladed rotor for 5 Pa inlet pressure boundary condition 101

Figure 7.5. The velocity profile for a 12-bladed rotor for 250 Pa inlet pressure boundary condition 102

Figure 7.6. The comparison of the flowrate vs. K-factor plots for different trailing edge shapes for the 12-bladed rotor with the blade pitch angle of 30° 103

Figure 7.7. The comparison of the flowrate vs. K-factor plots for different tip clearances for the curved trailing edge with 30° blade pitch angle for the 12-bladed rotor 105

Figure 7.8. The Reynolds' number vs. K-factor plots for the chosen geometry 106

Figure A.1. Linearity error 111

Figure B.1. Control volume used to illustrate discretization of a scalar transport equation [41] 113

LIST OF TABLES

Table 1.1.	Turkey's total natural gas transportation (million m^3) [4]	2
Table 1.2.	Flowmeters by physical quantity measured [11]	9
Table 4.1.	Fixed and variable design parameters	66
Table 5.1.	Details of the turbine meter.	76
Table 5.2.	Number of meshes used in the numerical model	80
Table 5.3.	Turbine meter characteristic values derived from figure 5.3	82
Table 5.4.	Comparison of Realizable k- ϵ and Reynolds Stress models	83
Table 5.5.	Realizable k- ϵ turbulence model without stopping moment	83
Table 5.6.	Realizable k- ϵ turbulence model with stopping moment	84
Table 7.1.	Numerical results taken for 30° blade pitch angle with 16-bladed rotor	96
Table 7.2.	Numerical results taken for 35° blade pitch angle with 16-bladed rotor	96
Table 7.3.	Numerical results taken for 40° blade pitch angle with 16-bladed rotor	97
Table 7.4.	Numerical results taken for 45° blade pitch angle with 16-bladed rotor	97
Table 7.5.	Polynomial approximations for different blade pitch angles with the 16-bladed rotor	97

Table 7.6.	Comparison of results taken for different blade pitch angles with the 16-bladed rotor	98
Table 7.7.	Numerical results taken for 12 blades for the blade pitch angle of 30°	99
Table 7.8.	Numerical results taken for 20 blades for the blade pitch angle of 30°	99
Table 7.9.	Polynomial approximations for different blade numbers for the blade pitch angle of 30°	99
Table 7.10.	Comparison of results taken for different blade numbers for the blade pitch angle of 30°	100
Table 7.11.	Numerical results taken for the curved trailing edge with 30° blade pitch angle for the 12-bladed rotor	102
Table 7.12.	Polynomial approximations for different trailing edge shapes for the 12-bladed rotor with the blade pitch angle of 30°	102
Table 7.13.	Comparison of results taken for different trailing edge shapes for the 12-bladed rotor with the blade pitch angle of 30°	103
Table 7.14.	Numerical results taken for a tip clearance of 0.5 mm for the curved trailing edge with 30° blade pitch angle for the 12-bladed rotor . . .	104
Table 7.15.	Numerical results taken for a tip clearance of 2.5 mm for the curved trailing edge with 30° blade pitch angle for the 12-bladed rotor . . .	104
Table 7.16.	Polynomial approximations for different tip clearances for the curved trailing edge with 30° blade pitch angle for the 12-bladed rotor . . .	104

Table 7.17. Comparison of results taken for different tip clearances for the curved trailing edge with 30° blade pitch angle for the 12-bladed rotor . . .	105
---	-----

LIST OF SYMBOLS/ABBREVIATIONS

α	Linear coefficient of expansion of meter body
a	Inner blade radius
A	Annular flow area
β	Blade pitch angle
β_1	Relative inlet angle of flow
β_2	Relative outlet angle of flow
C_{Df}	Friction drag coefficient
C_D	Drag coefficient
C_f	Local friction coefficient or surface (skin) friction coefficient
C_p	Pressure coefficient
c	Blade chord
C_L	Lift coefficient
δ	Deflection of flow at blade outlet from blade angle
D_f	Friction drag
D_p	Pressure drag
D_o	Meter diameter at reference temperature
D	Turbine meter diameter
F	Flow induced drag force
f	Reference diameter of meter
F	Force
ϕ	Transported quantity
i	Incidence angle
μ	Absolute viscosity of fluid
N_T	Total retarding torque
n	Blade numbers
ν	Kinematic viscosity
p	Pressure
Q	Volume flow rate
r	Rotor radius vector; Rotor radius variable; Radial distance

R	Outer blade radius; Hydraulic radius
\bar{r}	Root mean square of the inner and outer blade radius
r_c	Casing radius
r_h	Hub radius
Re	Reynolds number
Re_y	Wall distance based Reynolds number
ρ	Density of fluid
s	Blade spacing along the hub
S	Blade surface area per side
St	Strouhal number
S_{Mx}	Body forces
θ	Exit flow swirl angle due to rotor retarding torques
t	Time; Thickness of the blades
T	Temperature
τ_w	Wall shear stress
T_B	Bearing drag
T_d	Driving torque
T_h	Hub fluid drag torque
T_o	Reference temperature
T_s	Rotation sensor's drag torque
T_t	Blade tip clearance drag torque
T_w	Hub disc friction drag torque
U	Mean flow velocity
u_τ	Friction velocity
V	Velocity at the specific point; Incident fluid velocity vector
v	Velocity of the fluid through the reference diameter
V_{av}	Average velocity
V_E	Exit fluid velocity vector
V_o	Maximum speed
w_i	Ideal rotational speed of the rotor
w	Rotational speed of the rotor

$\bar{\omega}$	Rotor angular velocity vector
W	Width of rotor
y	Distance
AGA	American Gas Association
API	American Petroleum Institute
ASME	American Society of Mechanical Engineers
CFD	Computational Fluid Dynamics
GTM	Gas Turbine Meter
GUI	Graphical User Interface
IEO2005	International Energy Outlook 2005
ISA	Instrument Society of America
MRF	Multiple Reference Frame
NIST	National Institute of Standards and Technology
NRBC	Non-Reflecting Boundary Condition
RANS	Reynolds-averaged Navier Stokes
rpm	Revolution per minute
RSM	Reynolds Stress Model
SRF	Single Reference Frame
udf	User defined function

1. INTRODUCTION

1.1. Objective

Natural gas has been the fastest growing primary energy source in the world. According to the forecast of IEO2005 [1] (International Energy Outlook 2005), worldwide consumption of natural gas increases by an average of 2.3 percent annually from 2002 to 2025. The importance of natural gas can be well understood when this number is compared with projected annual growth rates of 1.9 percent for oil consumption and 2.0 percent for coal consumption. From 2002 to 2025, the world natural gas consumption (Figure 1.1) is projected to increase by almost 70 percent, from 92 trillion cubic feet (2.6 trillion cubic meter) to 156 trillion cubic feet (4.4 trillion cubic meter).

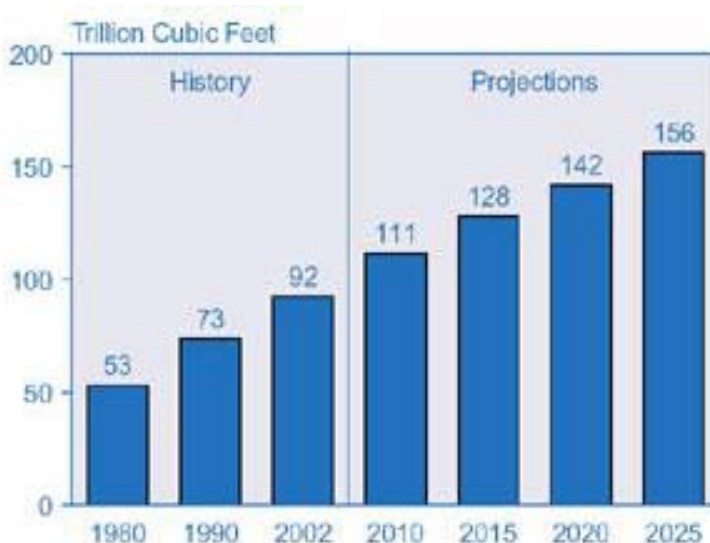


Figure 1.1. World natural gas consumption [1]

Worldwide gas consumption is still increasing, as is clearly shown by the continuous increase in number of commercial transactions and in the quantities of gas dealt with. That is the most important reason to measure the big quantities of natural gas bought by a company correctly [2]. It is worth remembering that in 2002, the worldwide natural gas production was more than 3.2 billion m^3 and consequently the world natural gas market was about 640 milliard \$ (assuming an average unitary price of 0.20 \$/ m^3).

The increased use of natural gas as the primary source of energy in countries in all stages of economic development from all over the world is creating an intricate network for gas transportation and trade of energy that is demanding more accurate measurements of gas flows, specially in aspects such as fair buy and sell and custody transfer[3].

Table 1.1. Turkey's total natural gas transportation (million m^3) [4]

1987	1988	1989	1990	1991	1992	1993	1994	1995
520	1,178	3,102	3,357	4,097	4,461	4,975	5,377	6,858
1996	1997	1998	1999	2000	2001	2002	2003	2004
8,040	9,874	10,384	12,656	14,975	16,368	17,625	21,180	22,173

Although Turkey is not a major natural gas producer and does not have significant reserves, it is strategically important because of its location on a possible east-west gas transportation corridor linking Europe with the Caspian region. As world's natural gas consumption increases each year, Turkey's natural gas transportation also increases as it can be seen above in Table 1.1.

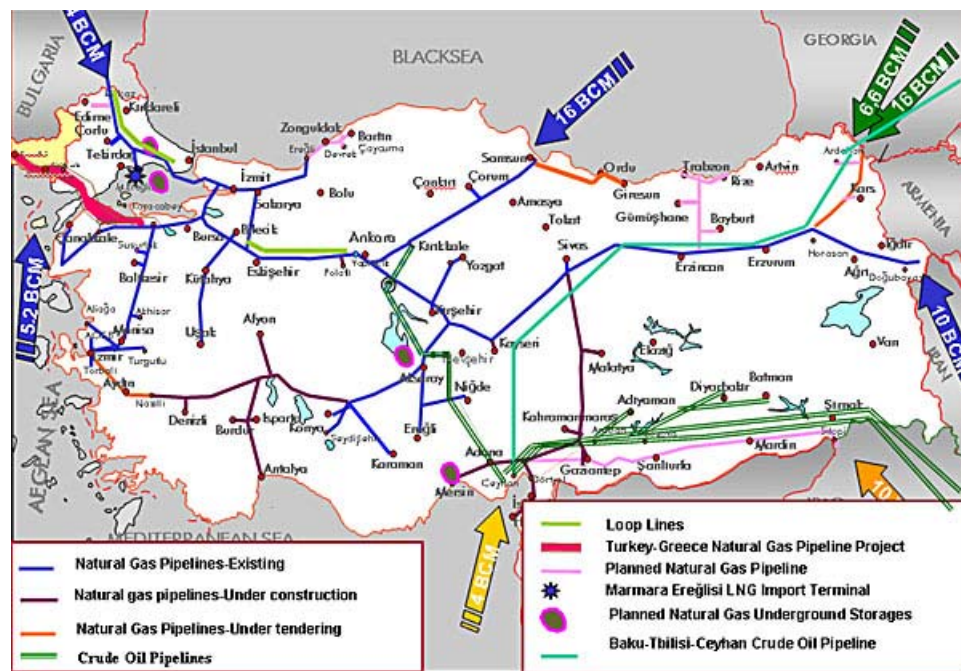


Figure 1.2. Turkey's natural gas network [4]

Obviously as a result of the growing natural gas network in our country (Figure 1.2), turbine gas meters will be widely used in the industry. Those turbine meters that are imported from foreign countries are ahead of the other turbine meters with their high sensitivities. Natural gas is a natural resource that is expensive and highly consumed in the industry. Even 1 % of error may cause hundred thousands of dollars of overcharge or undercharge. For this reason the production of those turbine meters which can only be imported for very high prices is important not only for the general balance of our country in international trade but also for the growth of national equipment industry.

The aim of this study is to improve the blade geometry of a gas turbine meter for a specific diameter by using CFD tools and also to provide a computer user-interface that can be used in the improvement process of gas turbine meter blades through sufficiently accurate flow simulations in the turbine gas meter cascade.

1.2. Flow Measurement History

Flow measurement has probably existed in some form since man started handling fluids. Although it is very difficult to clearly point out the first flow measurement experience of the primitive man in the history, a few stories describe that handfuls of water could have been the first defined volume of liquid. After the discovery of pottery making, wine and water were sold by measuring the liquid volume. In ancient times control over the process was the prime reason for flow measurement. Flow measurement for billing purposes developed later. It is possible to find information about the history of hydraulics and fluid mechanics but very little is known about the actual flow measurement. It was not a popular subject in the history as it is not a popular subject today. Today people pay very little attention on it, when they purchase their natural gas, domestic water, and gasoline through this technology.

In early history the Chinese, the Egyptians, and the Romans showed a great degree of understanding of hydraulics. The Egyptians, with their massive irrigation ditches and the weirs they used to distribute the flow to the fields. In some cases when

irrigation was required in fields higher than the source they were required to use bailers (Figure 1.3) which may be considered as the precursor of modern day displacement meters [5]. The first screw pump and also a water clock operating with filling up the bowls of water are among the highlights invented by the Egyptians.

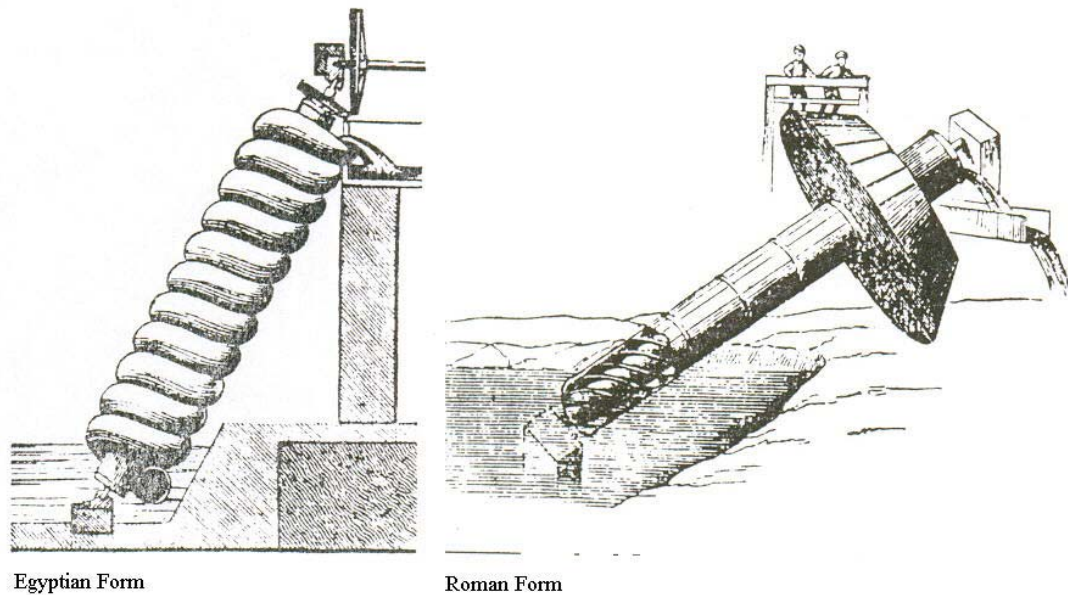
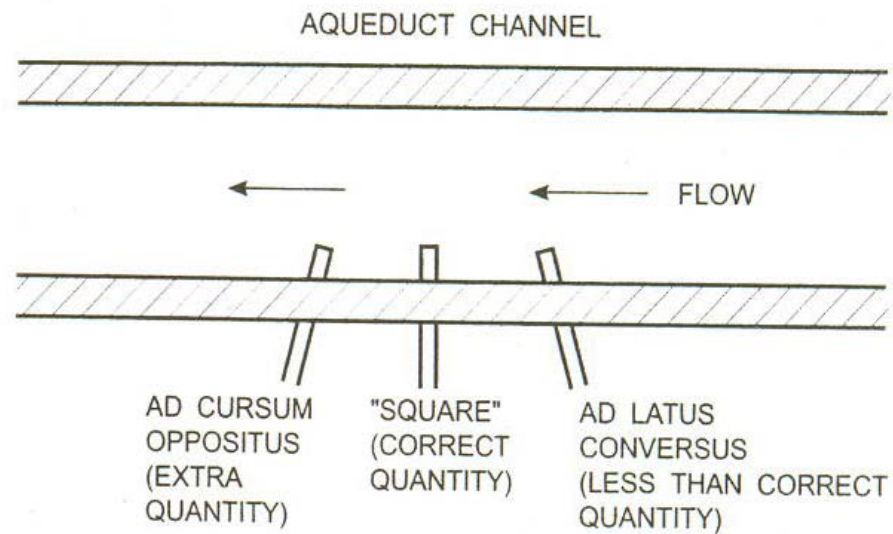
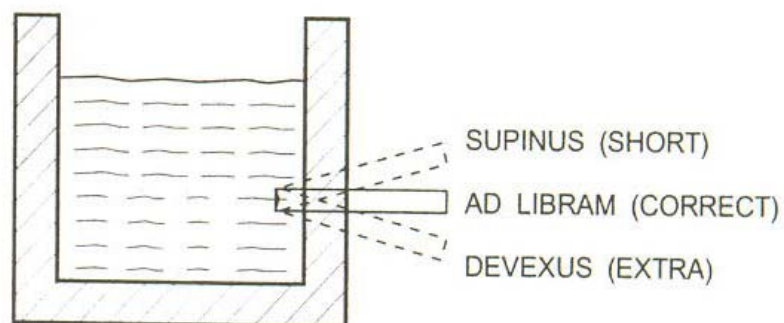


Figure 1.3. Egyptian and Roman form of Archimedean [5]

The Chinese needed to have some knowledge of the amount of flow in their rivers to design their reservoirs and massive canal systems. Today the same systems are used in the same way to prevent floods as they were in 1500 B.C. The Romans, in order to design their famous aqueducts, needed to know something about flow measurement since they supplied water equivalent to the amount a modern city of 700 000 uses today. Although Romans didn't have the necessary understanding for accurate flow measurement, they did know that installing the pipe perpendicular to the aqueduct was essential. They fully understood that if it faced upstream, more flow would go through the tap, and conversely, if it faced downstream, less flow would occur (Figure 1.4). For pumping water Romans also adapted their form of Archimedean screw pump (Figure 1.3) which is the first time that blades in the form of a screw were used to move a fluid from one place to another.



(a) PLAN



(b) SECTION

Figure 1.4. Roman pipe installation [5]

Before the early 1600's when the developers of the head meter, Castelli and Tonicelli, determined that the rate of flow was equal to the flow velocity times the area, and that discharge through an orifice varies with the square root of the head; Hero of Alexandria (ca 150 B.C.) clearly understood the modern concept of the continuity equation for the flow of an incompressible fluid. His statements can be found in the references (see Reference [6]). Leonardo da Vinci (1452-1519), among a myriad of other topics, was also interested in hydraulics. His works are collected in a nine-part treatise called "Del moto e misura dell' acqua" In this work he discusses floating bodies, water waves, eddies, the movement of water, and a host of other topics [5]. Figure 1.5 shows a sketch of flow over a contracted weir by Leonardo.

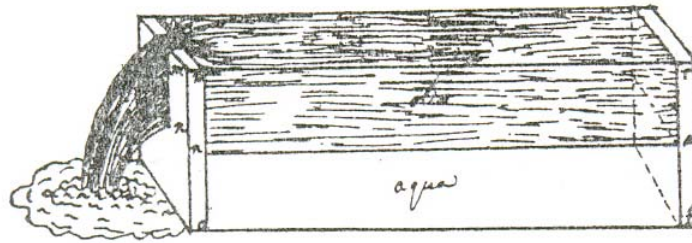


Figure 1.5. Sketch by Leonardo of flow over a contracted weir [5]

Professor Poleni, in the early 1700's, provided additional work on understanding discharge of an orifice. At about the same time, Bernoulli developed the theorem upon which hydraulic equations of head meters have been based ever since. In the 1730's, pitot published a paper on a meter he had developed. Venturi did the same in the late 1790's, as did Herschel in 1887. In London, in the mid 1800's, positive displacement meters began to take form for commercial use. In the early 1900's, the fuel-gas industry started development in the United States with Baltimore GasLight Company [7].

In early 1900's Rotary meters became available. In 1912 Weymouth calibrated a number of thin plate orifices and reported his work as a paper named "Measurement of Natural Gas" to the American Society of Mechanical Engineers (ASME) In the same time period Metric Metal Works, the Foxboro Company and Pittsburg Equitable, were the forerunner meter companies which conducted their own tests.

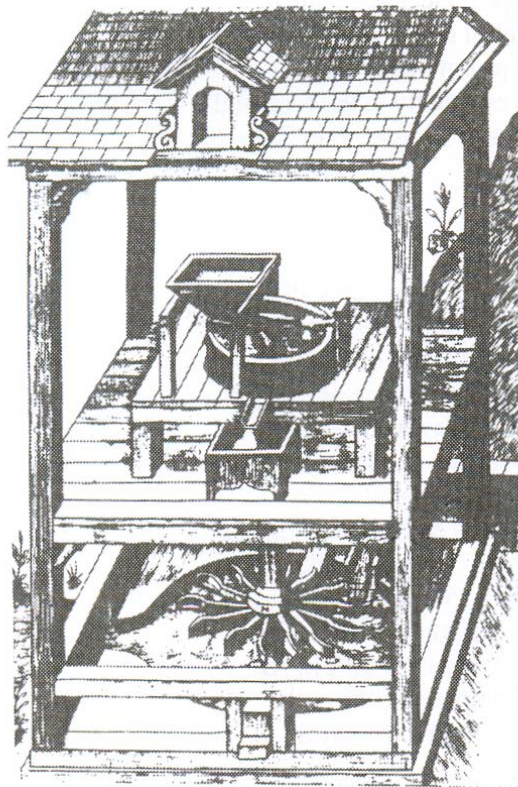
Different meters for use in different areas of flow measurement developed very fast in 20th century, such as vortex shedding, ultrasonic, magnetic and laser flowmeters. On the other side with the growing gas industry, gas flow measurement became an important topic. Although different flowmeters are available for gas flow measurement today, turbine flowmeters are still the most commonly used ones among the others.

1.2.1. Historical Development of Turbine Meters

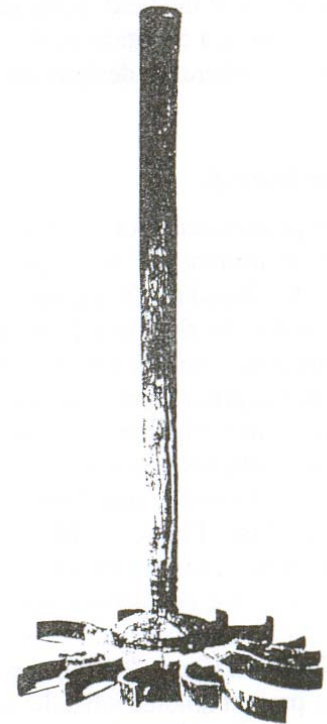
Today, different designs of axial turbine flowmeter are used for a variety of applications where accuracy, reliability, and rangeability are required in major industries like

water, natural gas, oil, petrochemical, chemical process, cryogenics, milk and beverage, aerospace, and biomedical. The modern axial turbine flowmeter, which is a reliable device providing the highest accuracies attainable by a flow sensor for both liquid and gas volumetric flow measurement, dates back to the ancient times.

In ancient Greece, a horizontal turbine wheel working with water power was used to grind flour. Also the Irish used one in the fourth century when King Cormac macArt sent for a skilled man to build a mill (Figure 1.6 a). In circa 1588, a horizontal mill (Figure 1.6 b) was designed similar to the impulse turbine of Pelton (1829-1908) [5]. In 1681, Robert Hook proposed a small windmill for measuring air velocity. Captain Phipps in 1773 employed the principle that a spiral in turning moves through the length of one turn of the spiral [8].



(a) A HORIZONTAL MILL FROM
LE DIVERSE ET ARTIFICIOSE MACHINE
BY AGOSTINO RAMELLI, 1588



(b) THE MOYCRAIG TIRL,
BELFAST MUSEUM

Figure 1.6. Horizontal mill [5]

Although the principle of using a vane to impart motion to a fluid dates back to the Archimedes' screw pump, this principle was not used to measure velocity until 1790. As a result of intensive innovation and refinements to the original axial vaned flowmeter principle, Woltman developed the first known meter and applied this to measure water flow in 1790.

After one and a half centuries later of this development, the first modern meters consisting of a helically bladed rotor and simple bearings were developed in the USA for fuel measurement in airborne applications [8]. Actually, modern development activity was largely driven by the US natural gas industry in the late 1940s and 1950s, with the need to accurately measure the flow in large-diameter, high-pressure, interstate natural gas lines. After turbine meters were introduced in the United States, they became popular in the short run as a reference standard at recognized calibration facilities in the US and Europe.

In the 1990's, multipath ultrasonic metering technology with a set of potential attributes were introduced. Lastly, evolutionary changes in turbine meter design made in 1997 resulted in extension of capacity ratings, in-line transfer proving capability and operating and maintenance expense reduction [9].

1.3. Classification of Flowmeters

Flowmeters may be classified by the general method in which flow information is extracted from the fluid system. They may be inferential, in which a physically measurable parameter of the flow stream other than flow or velocity is used to indicate the flow rate. Velocity may also be directly measured. Alternatively, energy additive flowmeters inject additional energy into the flow stream to create a useful, measurable parameter [10].

On the other side it may be confusing to classify flowmeters under a family name since even under the same category of the flowmeters it is possible to find significant differences. An example could be the orifice and the flow nozzle which belong to the

inferential category of flowmeters. Instead of classifying them under the common family names it could be more correct to give a list of all the available flowmeters keeping the flow information extracted from the fluid system as the classification parameter. Table 1.2 gives a list of flowmeters according to the physical quantity measured. This list can be re-categorized by the technology employed (Technology), the instrumentation configuration (Instrument) and also by flow quantity converted (Result) .

Table 1.2. Flowmeters by physical quantity measured [11]

	Measure	Result	Technology	Technology	Instrument
1.	Acceleration	Mass	Coriolis		Misc.
2.	Acoustic Waves	Velocity	Ultrasonic	Doppler	Electronic
3.		Velocity		Transit Time	Electronic
4.	E. Magn. Field	Velocity	Magnetic		Electronic
5.	Force	Velocity	Target		Mechanical
6.	Frequency	Velocity	Vortex		Mechanical
7.	Heat Transfer	Velocity	Thermal		Misc.
8.	Pressure	Volume	Dif. Pressure	Elbow	Pressure
9.		Volume		Flow Nozzle	Pressure
10.		Volume		Orifice	Pressure
11.		Volume		Pitot Tube	Pressure
12.		Volume		Pitot Tube	Pressure
13.		Volume		Venturi	Pressure
14.		Volume		Wedge	Pressure
15.		Volume	Variable Area	Movable Vane	Pressure
16.		Volume		Rotameter	Pressure
17.		Volume		Weir, Flume	Pressure
18.	Volume	Volume	Pos. Displacement	Nutating Disc	Mechanical
19.		Volume		Osc. Piston	Mechanical
20.		Volume		Oval Gear	Mechanical
21.		Volume		Roots	Mechanical
22.		Volume	Turbine		Mechanical

1.3.1. Turbine Flowmeter Types

The operating principle for all the turbine meters are the same, however it is possible to classify them according to some design and application differences for different turbine meters. Below the main characteristics are described briefly for any flowmeter belonging to the turbine meter family of flowmeters.

1.3.1.1. Precision liquid meters. As it is obvious by the name, it is designed for liquid measurement and are highly precise when compared with the other turbine flowmeters. The rotor which can be helical or straight is the most important part of the flowmeter. Figure 1.7 shows the components of such a turbine meter.

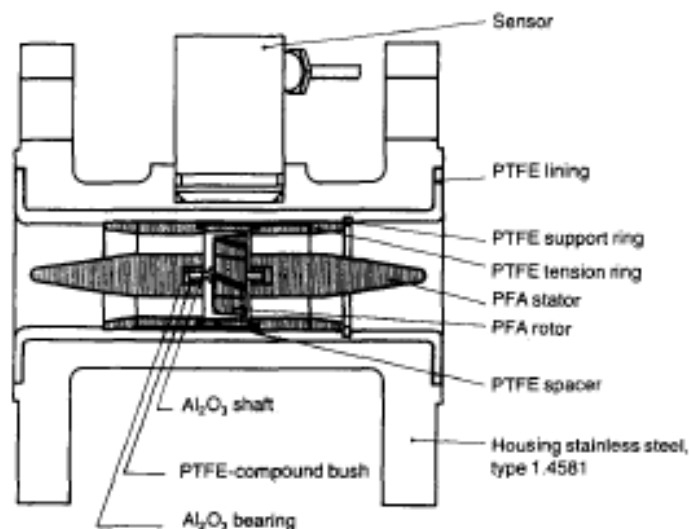


Figure 1.7. Endress & Hauser corrosion-resistant meter design [8]

1.3.1.2. Gas Turbine Meter. It is similar to the precision liquid flowmeters but there are also significant design differences which is an adaptation for gases. The most obvious of these is the large hub and comparatively small flow passage in order to impart as large a torque as possible on the rotor by moving the flow to the maximum radius and increasing the flow velocity [8]. Details of this type of turbine flowmeters will be given in chapter 2.

1.3.1.3. Water Meters. A common design of this meter is for a complete mechanical insert to be designed to fit into a flanged iron section of pipe with a specially made central containment section. The insert consists of: flow straighteners, which also incorporate the upstream bearing; the rotor, which is usually of helical design and may have a substantial clearance between the blade tips and the casing; the rotor shaft, the motion of which is transmitted via a right-angle worm gear assembly into a watertight gear box; and a rudder (or trimming vane) upstream of the rotor, which provides a mechanical calibration adjustment by altering the angle at which the inlet flow stream hits the rotor blades [8]. Diagram of a water meter is shown in Figure 1.8.

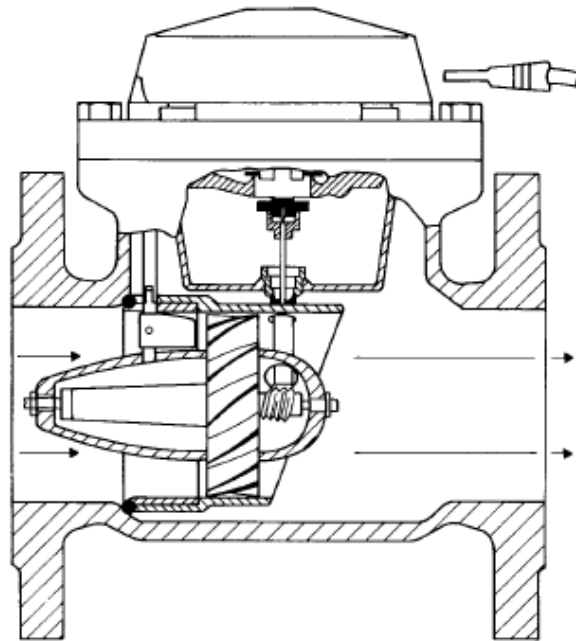


Figure 1.8. Gas and Water Meter Manufacturers Ltd meter [8]

1.3.1.4. Dual Rotor Turbine Meter. This is a high accuracy flowmeter primarily intended for use on large natural gas lines. It incorporates two closely coupled turbine rotors which rotate in the same direction. The upstream rotor is the main rotor and the second rotor, which has a much shallower blade angle, is the sensor rotor. Continuous and automatic correction of measurement errors due to varying bearing friction is achieved by calculating the flow rate based on the difference between the rotor speeds. This turbine meter is sold as self correcting [12].

1.3.1.5. Quantum Dynamic Flowmeter. This design (Figure 1.9) also uses a patented twin turbine configuration. The downstream slave turbine drives the shaft on which the indicator turbine bearings rotate freely. Under normal conditions the rotational speeds of the indicator and slave turbines are closely matched. At high flowrates the rotational speeds of the indicator turbine and the slave turbine shaft assembly will begin to diverge. The integral flow-straightening device upstream of the indicator turbine reduces swirl and hence the effect of upstream flow distortion [8].

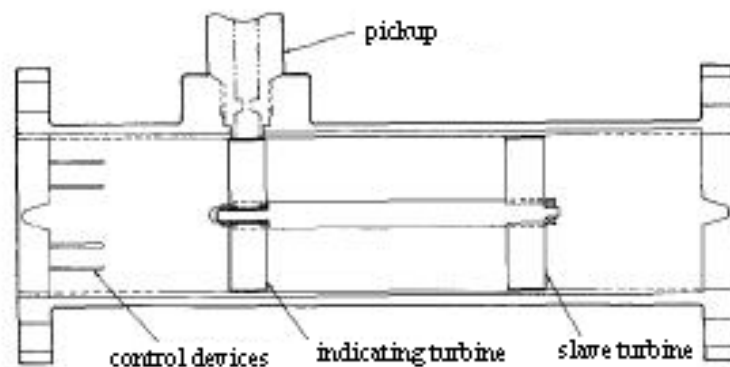


Figure 1.9. Quantum Technology meter [5]

1.3.1.6. Spirometer. Monitoring spirometers measure the volumes of gas flows entering and leaving the lungs and may also be incorporated in ventilator circuits. Diagnostic spirometers are used to monitor the degree and nature of respiration. With these a clinician may determine patient respiratory condition by various measures and clinical maneuvers. Low cost, light weight, speed of response and patient safety are major considerations [5].

1.3.1.7. Pelton Wheel (Multijet Turbine Flowmeter). This operates like a hydraulic pelton wheel by using the impulse due to the fluid jet momentum. To achieve this the flow is constricted to a small outlet and hence forms a high-speed jet. It is designed for use with liquids. Figure 1.10 shows the typical design [8].

1.3.1.8. Insertion Axial Turbine Meter. These flowmeters comprise a small axial rotor mounted on a stem which is inserted radially through the conduit wall, often through a shut-off valve. They measure the flow velocity at the rotor position from which the

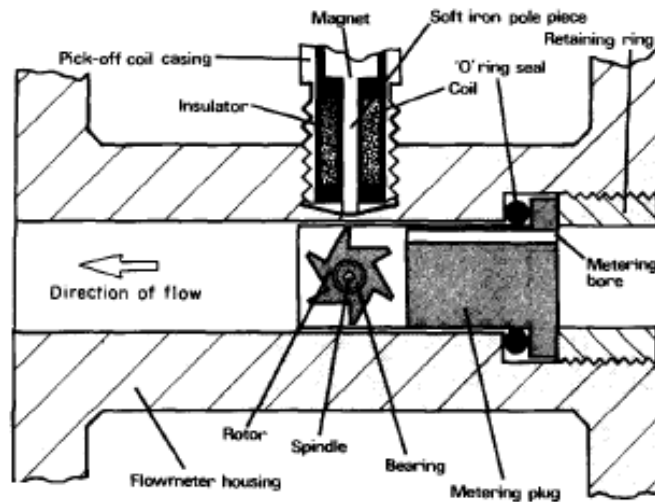


Figure 1.10. Pelton Wheel Meter by Data Industrial Corporation [8]

volumetric flow rate is inferred. They are an economical solution to flow measurement problems where pipe diameters are high and accuracy requirements are moderate, and also may be technically preferred where negligible pressure drop is an advantage, as in high speed flows. They are typically more linear than insertion tangential turbine flowmeters and compete also with magnetic and vortex shedding insertion flowmeters [12].

1.3.1.9. Paddle Wheel Flowmeter. The members of this family are not high-precision instruments and the description inferential sometimes applied to turbine flowmeters is probably appropriate for these because the flow of fluid through the meter is inferred from the effect on the rotor of its interaction with a proportion of the fluid flow [8].

2. Gas Turbine Meter

The need of accurately measuring natural gas increased as in the late 1940's and 50's with the development of US natural gas industry. The principal used to measure the gas flow rate was very successful and today gas turbine meters are still one of the most accurate meters for gas measurement. GTMs belong to the family of volumetric flowmeters and are known with their good measurement precision and repeatability. They are available for a range of operating pressure and temperature in different sizes for different flow rate capabilities. Figure 2.1 shows an overall picture of the instrument.



Figure 2.1. Gas Turbine Meter [14]

2.1. Operating Principle

Basically GTMs consist of a rotor wheel, bearings, a machined housing, and a sensor for registering the rotational speed of the rotor. The rotor wheel mounted on a shaft spins freely around its rotational axis and has at least two but usually more blades. The gas flows through a cylindrical housing causing the rotor to turn with a rotational speed proportional to the velocity of the flow. That also makes the frequency

of the pulses proportional to the volumetric flow rate through the meter. Additionally almost every GTM has flow straighteners on other sides of the rotor in order to impose an evenly distributed flow profile, impacting on the turbine wheel. The contraction of the volume increases the flow velocity so that more torque can be exerted from the flowing gas. The passing flow rate is actually the mean velocity of the fluid multiplied by the area of the annular slot. Every time the rotor wheel completes one revolution a certain amount of volume passes. That brings about the turbine meter coefficient which is also called as the K factor. K factor is expressed in terms of pulses per volume or revolution per volume.

The sensor for the registration of the GTM can be in various forms. It may be a gear driven counter connected to the turbine wheel, an electric sensor or a magnetic sensor. However when the rotor wheel is registered, any kind of sensor produces a retarding force on the rotor while registering the rotor wheel frequency. The main components of a turbine meter is given in Figure 2.2

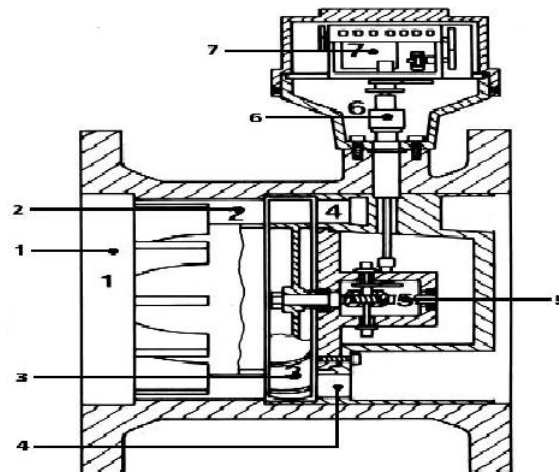


Figure 2.2. Schematic view of a GTM components: flow conditioner (1), flow channel (2), turbine rotor blading (3), flow ring (4), gear train (5), magnetic coupling (6), counter (7) [15]

2.2. General Performance Characteristics

- Best performance while measuring clean, conditioned, steady flows of gases with low kinematic viscosities (below about $10^{-5} \text{ m}^2\text{s}^{-1}$, 10 cSt, although they are

used up to $10^{-4} \text{ m}^2\text{s}^{-1}$, 100 cSt), and are linear for subsonic, turbulent flows.

- Internal diameter range from 6 to 760 mm , (1/4" - 30").
- Maximum measurement capacities range from 0.025 Am^3/hr to 25,500 Am^3/hr , (0.015 ACFM to 15,000 ACFM), for gases, where A denotes actual.
- Typical measurement repeatability is $\pm 0.25\%$ with up to 0.02% for high accuracy meters. Typical linearities, are between 0.5% and 1.0%. High accuracy meters have linearities of 0.25%, usually specified over a 10:1 dynamic range below maximum rated flow. 0.25% for air.
- Rangeability, when defined as the ratio of flow rates over which the linearity specification applies, is typically between 10:1 and 100:1.
- Operating temperature ranges span -270°C to 650°C , (-450°F to 1200°F).
- Operating pressure ranges span coarse vacuum to 414 MPa, (60,000 psi).
- Pressure drop at the maximum rated flow rate ranges from around 0.3 kPa (0.05 psi) [16].
- Normally the blade count varies from 6 to 20 or more depending on the pitch angle and the blade radius ratio.
- " The blade pitch angle, which primarily determines the rotor speed, is typically 30 to 45 degrees but may be lower in flowmeters designed for low density gas applications [12].
- A typical specification for the uncertainty is $\pm 2\%$ from the minimum flow rate, Q_{min} to 20% of the maximum flow rate, Q_{max} , and $\pm 1\%$ from 20% of Q_{max} to Q_{max} .
- Maximum flow velocities can be up to 60 m/s [8].

2.3. Calibration

The best of meter designs, the most appropriately sized meter, and the most properly installed meter are all but worthless if the calibration of the meter is not also appropriate and correct. The ideal calibration for any meter would be traceable to a NIST (National Institute of Standards and Technology) primary calibration system at the exact temperature and pressure on the exact fluid that the meter will be used to measure. Unfortunately this is not always possible or practical.

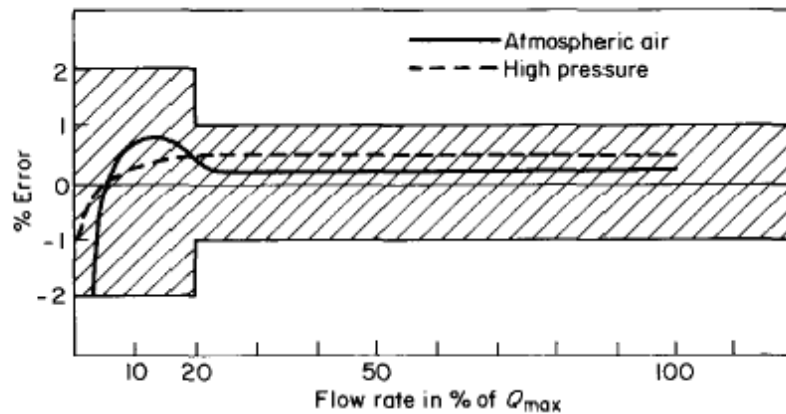


Figure 2.3. Maximum allowable error and characteristic of an Instronet Gas Meter [8]

Like any transducer, a turbine flowmeter is sensitive to physical parameters other than which is of interest. While designed to measure flow, a turbine meter responds to the viscosity of a fluid as well as its velocity [17]. In general it is more complete to say that a turbine meter responds to any variable that may directly or indirectly change the Reynolds number. A set of parameters can be correlated in order to calibrate a GTM but the most complete correlation parameters would be Strouhal number vs. Reynolds number.

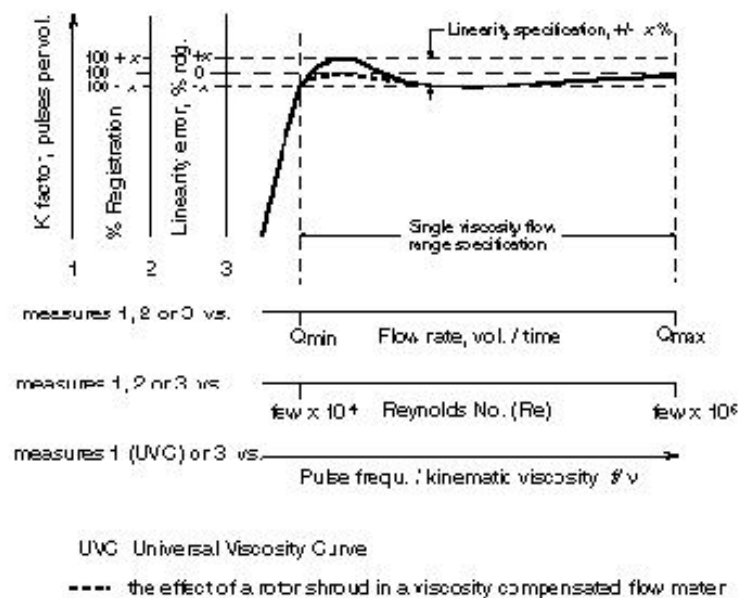


Figure 2.4. Calibration curve for a low-viscosity fluid with principal alternative presentations [12]

2.3.1. Frequency vs. Flowrate

The calibration of a turbine flowmeter consists of observing the output frequency of the meter for specific rates of flow as determined by the particular calibrator being used. The result is a linear curve as illustrated in Figure 2.5. However, this curve is valid only for fluids with a kinematic viscosity similar to that of the fluid used in calibration. The curves change for different viscosity fluids [5].

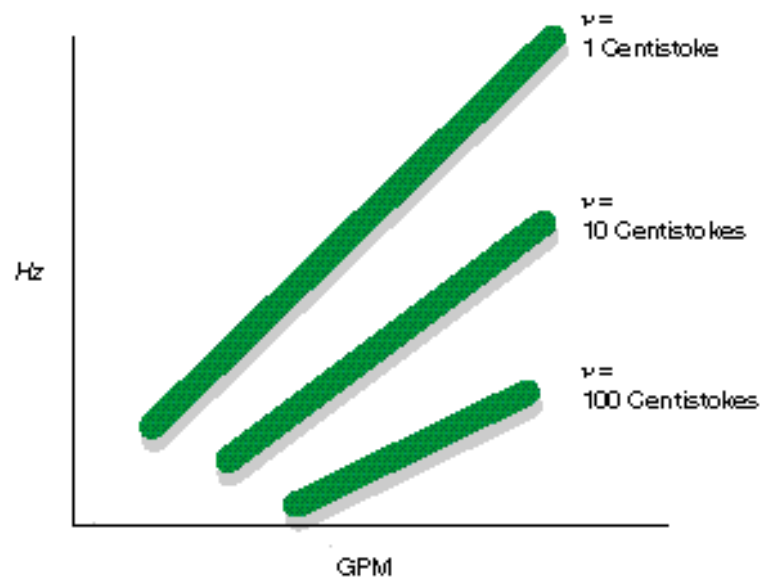


Figure 2.5. Frequency vs. flowrate for different viscosities [17]

2.3.2. K Factor vs. Flowrate

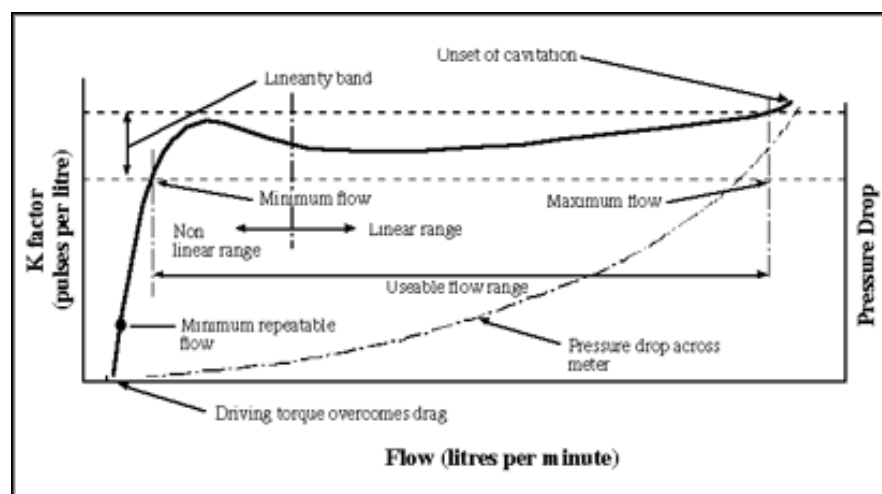


Figure 2.6. K Factor vs. flowrate diagram [18]

Although this kind of calibration (Figure 2.6) is limited to the kinematic viscosity, it is commonly used for applications in which the meter is calibrated at the same conditions as the application. This could be considered as a practical and better way to represent the data, but this calibration only counts for the conditions where temperature and pressure do not change.

2.3.3. Universal Viscosity Curve

Another calibration method is called Universal Viscosity Curve which is the ratio of the output frequency to the kinematic viscosity. This method is commonly used for a wide range of viscosities. With the help of this calibration method the calibration is possible for a wide range of fluids through the experiments conducted on air.

The rationale for using the ratio $\frac{Hz}{\nu}$ may be seen by observing that it is directly proportional to the Reynolds Number for the flow through the meter. In other words it is an abbreviated form of Reynolds number. Hence the Universal Viscosity Curve is essentially a plot of Meter Sensitivity vs. Reynolds Number. As such, it reflects the combined effects of velocity, density and absolute viscosity acting on the meter. The latter two are combined into a single parameter by using kinematic viscosity (ν) [17].

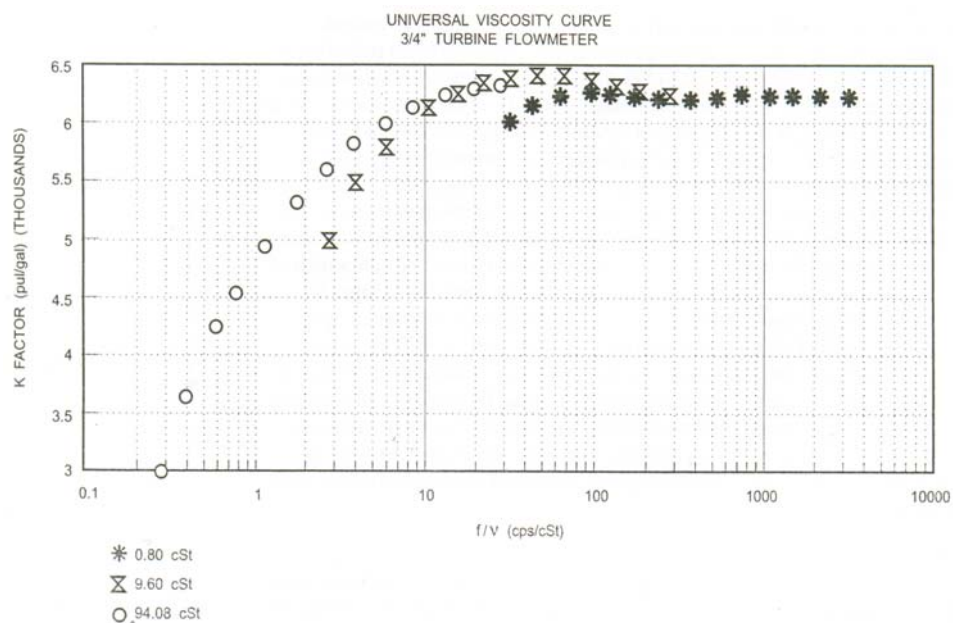


Figure 2.7. Universal viscosity calibration [5]

2.3.4. K-Factor vs. Reynolds number

Reynolds number Calibration of Turbine Meters refers to the calibration of the meter under conditions replicating those under which the meter will undergo in service. Obviously turbine meters are affected by different flow conditions. Reynolds Number has been shown to encompass the variables fluid density, and absolute viscosity that impact turbine performance. As such Reynolds Number calibration (Figure 2.8) has been recognized as one of the most desirable methods to ensure that as many unknown variables have been eliminated through a calibration. Several methods of achieving this have been used with success [19].

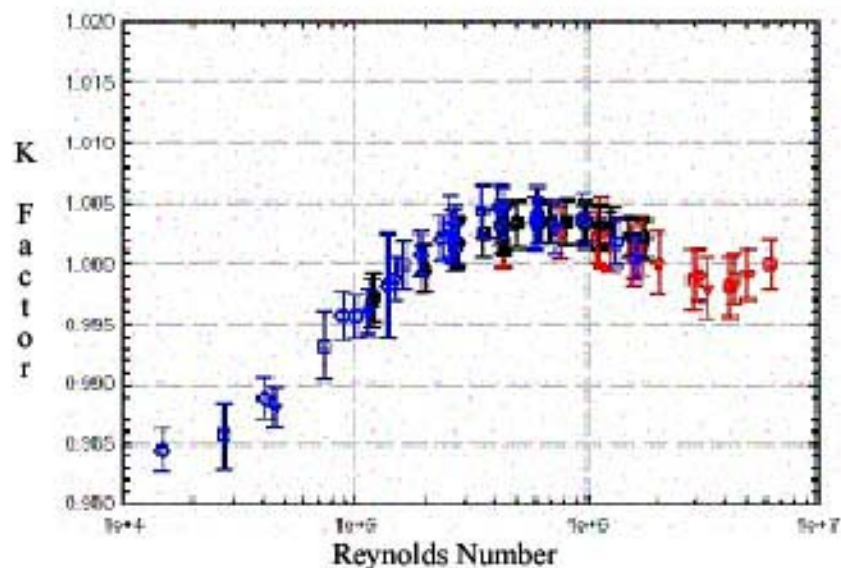


Figure 2.8. Strouhal number vs. Reynolds number [19]

2.3.5. Strouhal Number vs. Reynolds Number

The best way to present the data for a turbine meter is Strouhal number as a function of Reynolds number. The $St.$ vs. Re presentation (Figure 2.9) takes into account all of the secondary affects to which the meter is sensitive. It is very important for gas calibrations, since the density and kinematic viscosity are a function of both temperature and pressure. Using K factor in the above mentioned calibration methods ignores the effect of temperature on the meter body, since the meter will change diameter when the temperature changes. Using Strouhal number instead of K

factor will account for this temperature affect. A mathematical model of $St.$ vs. Re calibration is given below. Both dimensionless terms contain a form of the variable being determined by the measurement.

For f = meter output frequency, D = reference diameter of meter, v = velocity of the fluid through the reference diameter, and St = Strouhal number

$$St = \frac{fD}{v} \quad (2.1)$$

For ρ = density of fluid, μ =absolute viscosity of fluid, Re = Reynolds number

$$Re = \frac{Dv\rho}{\mu} \quad (2.2)$$

$$\nu = \frac{\mu}{\rho} \quad (2.3)$$

So for ν = kinematic viscosity

$$Re = \frac{Dv}{\nu} \quad (2.4)$$

Since both Re and St contain velocity as a term and the velocity is directly proportional to flowrate, it is difficult to use these forms of dimensionless parameters. More usable forms could be the following.

K factor is defined as frequency/flowrate

$$K = \frac{f}{Q} \quad (2.5)$$

But $Q=Av$, so Q is proportional to D^2v Then,

$$K = \frac{f}{vD^2} \quad (2.6)$$

Multiplying by D^3 will yield the dimensionless parameter Strouhal number.

$$St = \frac{fD^3}{vD^2} = \frac{fD}{v} = KD^3 \quad (2.7)$$

The diameter of the meter will change as a function of temperature as for D_o = meter diameter at reference temperature, α = linear coefficient of expansion of meter body, T_o = reference temperature

$$D = D_o[1 + \alpha(T - T_o)] \quad (2.8)$$

Substituting equation 2.8 in equation 2.7 yields:

$$St = \frac{fD}{v} = KD_o[1 + \alpha(T - T_o)]^3 \cong KD_o^3[1 + 3\alpha(T - T_o)] \quad (2.9)$$

Multiplying Re by St:

$$ReSt = \frac{vD}{v} \frac{fD}{v} = \frac{fD^2}{v} = \frac{fD_o[1 + \alpha(T - T_o)]^2}{v} \cong \frac{fD_o^2[1 + 2\alpha(T - T_o)]}{v} \quad (2.10)$$

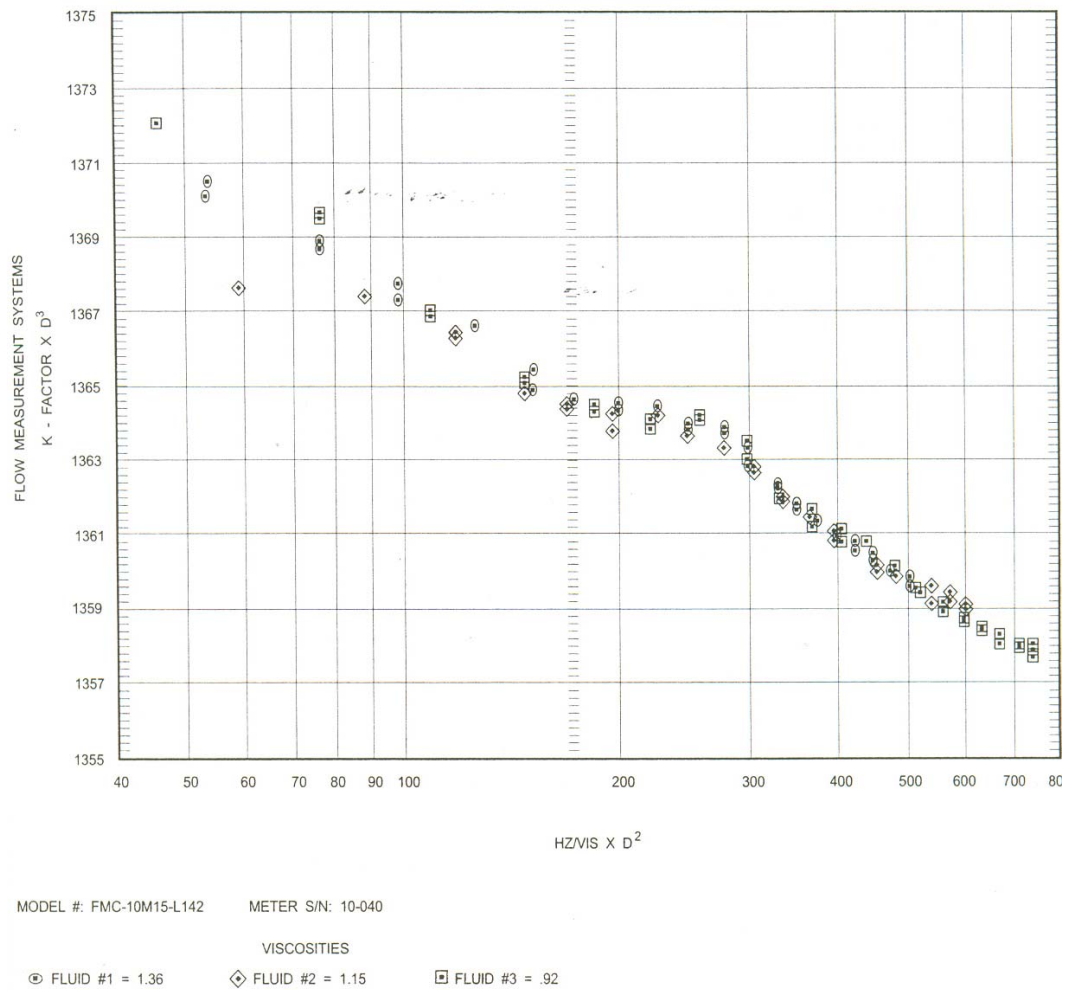


Figure 2.9. Meter calibration results [5]

2.4. Flow Straighteners and Flow Conditioners:

The velocity flow profile is the most important topic under flow conditioning. The velocity profile of the fluid depends on the Reynolds number developed in the pipe or the closed conduit. For laminar flow the velocity profile makes a parabola whereas for turbulent fully developed flows the profile is very close to uniform. As the Reynolds number increases, the flow profile becomes more and more uniform since the viscous effects near the wall become negligible. A mathematical description of the velocity profile for different Reynolds number is described below.

In a pipe flow When $Re < 2100$ the flow is laminar. In laminar flows for V_o =the maximum speed, r =the radial distance of the specific point from the middle axis, R =the hydraulic radius, V is the velocity at the specific point, V_{av} =the average velocity

$$V = V_o \left(1 - \frac{r^2}{R^2}\right) \quad (2.11)$$

$$V_{av} = \frac{V_o}{2} \quad (2.12)$$

When $2100 < Re < 4000$ The flow is in transitional region and no specific equation for the flow profile is possible, however this region may be considered as a part of the turbulent flow and the same equation may be used in order to determine the flow profile in this region.

When $Re > 4000$ the flow is turbulent. In turbulent flows where n is a coefficient and f is the friction factor

$$V = V_o \left(1 - \frac{r}{R}\right)^{1/n} \quad (2.13)$$

$$n = \frac{1}{\sqrt{f}} \quad (2.14)$$

f is a function of Reynolds number and can be obtained from the Moody Chart. Another way to calculate f is the through the following equations.

For wholly turbulent condition where D is the pipe diameter or hydraulic diameter, ϵ is the roughness element.

$$\frac{1}{\sqrt{f}} = 2 \log_{10}(D/\epsilon) + 1.14 \quad (2.15)$$

For transition region the following equation is recommended[20].

$$1/\sqrt{(f)} = 1.14 - 2\log_{10}((\epsilon/D) + 9.35/Re\sqrt{(f)}) \quad (2.16)$$

$$V_{av} = 2n^2V_o/(1 + 2n)(1 + n) \quad (2.17)$$

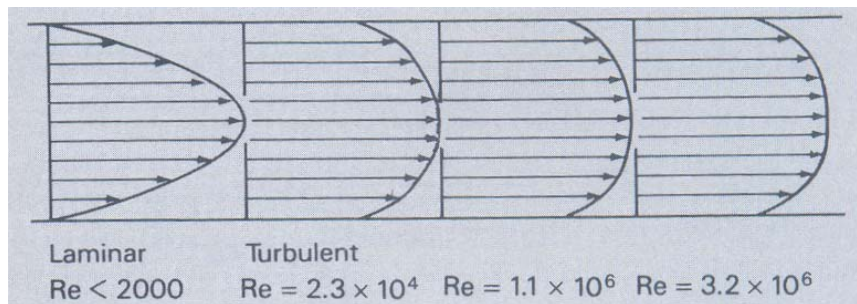


Figure 2.10. Flow profiles for different Reynolds numbers [21]

The most important-and most difficult to measure-aspects of flow measurement are flow conditions within a pipe upstream of a meter. Flow conditions refer to: the gas velocity profile, irregularities in the profile, varying turbulence levels within the velocity or turbulence intensity profile, swirl and any other fluid flow characteristics which will cause the meter to register flow different than that expected. This will cause the meter to differ from the original Calibration State referred to as reference conditions that are free of installation effects [22].

The distinction between a flow straightener and a conditioner is that the flow straightener only removes swirl where as flow conditioner creates a standard flow profile whatever the inlet profile shape is. Some types of flow profile improving devices are given in Figure 2.12.

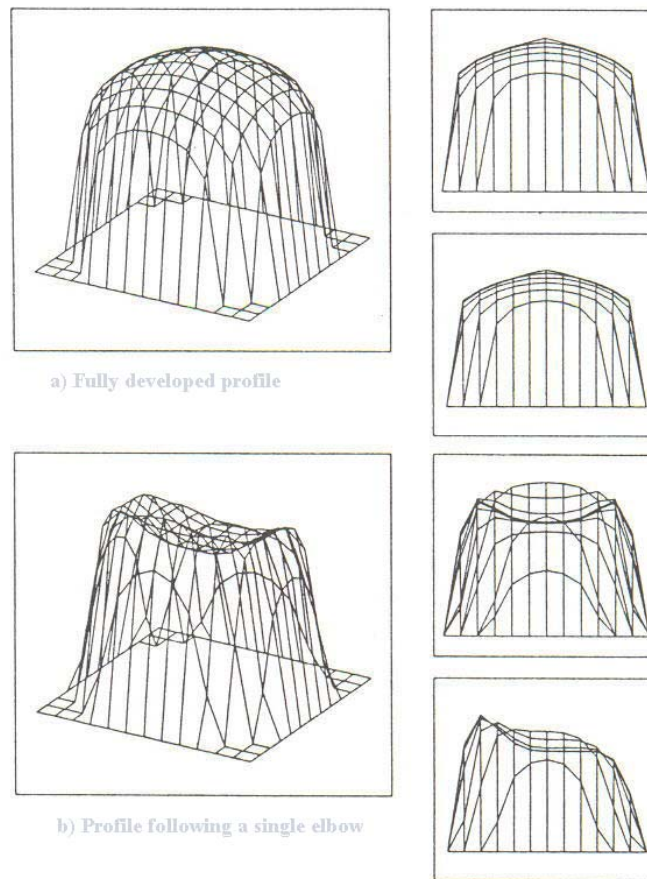


Figure 2.11. Effect of a single elbow on the profile [7]

Installation effects which cause flow conditions within the pipe to vary from reference conditions are: insufficient straight pipe, exceptional pipe roughness or smoothness, elbows, valves, tees and reducers, just to name a few. Flow Conditioning refers to the process of artificially generating a reference, fully-developed flow profile and is essential to enable accurate measurement while maintaining a cost-competitive meter standard design [22]. Shape of the profile and the swirl in the upstream of a turbine meter should be removed with the help of flow conditioners and straighteners. However swirl is a more effective factor than the profile for incorrect meter registration.

2.5. Design and Construction

There are different design considerations one can consider in order to obtain an optimum gas turbine meter. Different turbine meter parts can be a target for a better performance of the turbine meter. Mostly the parts in consideration would be the rotor

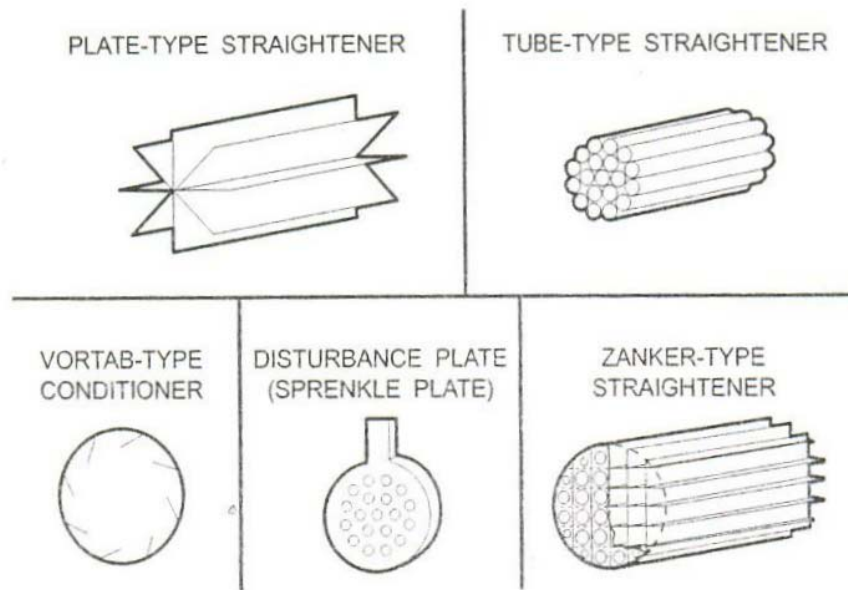


Figure 2.12. Some types of devices used for improving flow profiles [5]

wheel geometry, different diameters, bearings, sensors and flow conditioners. Since the blade design is the main subject of this thesis, only the design consideration for the rotor wheel will be discussed. For designing the other parts of the turbine meter please refer to Spitzer et. al. [5].

Commonly most of the turbine meter design focus on the rotor considering different constraints and aspects. It is not possible to find only one correct design which is suitable for all conditions, but there are key points one should keep in mind during the process of turbine meter design.

The most important design characteristic of the turbine meter rotor is stability, not efficiency as with a drive turbine. A good turbine flowmeter must transform an axial velocity into a rotational velocity as precisely and repeatably as possible. It is not necessary to produce the highest free-spin speed possible but to produce the most stable representation of the axial velocity and one that is the least affected by the secondary influences [5],[8],[23].

If the flow velocity profile were uniform, the correct blade angle distribution would be according to the following equation [23].

$$\tan(\beta)/r = \text{constant} \quad (2.18)$$

where β is the blade pitch angle and r is the radius at the specific point

If the radial profile is not flat which is in reality the case then in order to maintain a proportionally relative tangential velocity relationship, the radial twist of the blade would be proportionally biased [5].

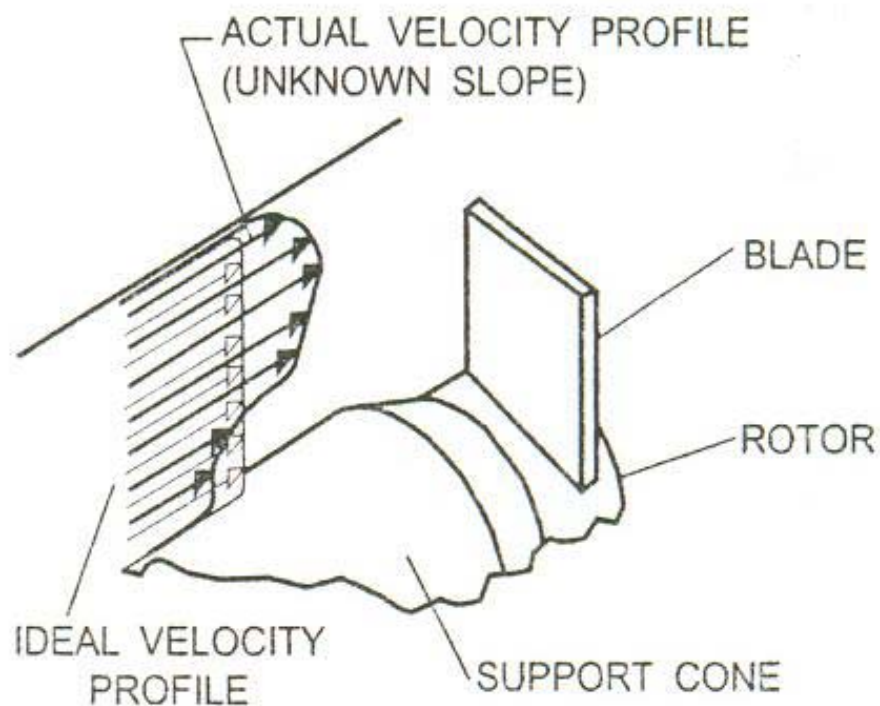


Figure 2.13. Velocity profile approaching the blade [5]

Another factor that would be taken into account in designing an efficient blade is the shape of the blade in terms of the airfoil shape to produce the least drag (resulting in the lowest axial force component) and the highest tangential force component (resulting in the highest torque or rotational speed). A study about two different shapes of the trailing edge can be found in the reference by Baker et. al. [8].

The blade pitch angle is another characteristic to play with. The angular velocity of the rotor is a trigonometric function of that blade angle, as shown in Figure 2.14.

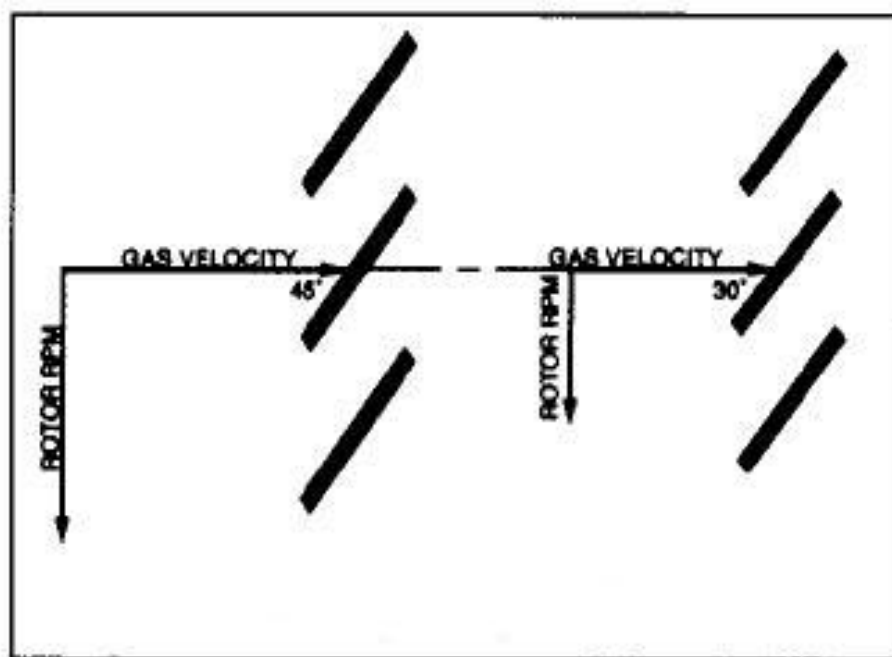


Figure 2.14. Rotor rpm vs. flowrate [9]

It can be seen that the angular velocity of the rotor is proportional to the tangent of the blade angle and the linear velocity of the gas flowing through the rotor blades [9]. Reducing the angle results in a decrease in the rotational speed of the rotor which increases the maximum capacity of the turbine meter, considering the maximum speed limit for a turbine rotor which is commonly 30000 rpm.

Tip clearance is also a design variable to optimize in turbine meter design. The minimum the tip clearance is the more drag is exerted on the rotor blade, while increasing the tip clearance more than enough results in the passing of the fluid without registering.

Another desirable characteristic of a turbine meter is to maintain the meter constant (K factor) at the same value over as wide a range in flow as possible. A highly efficient blade tends to vary in efficiency as a function of speed (flow rate), resulting in a significant decrease in meter constant as a function of flow rate.

In reality the inefficient blade designs are better for a turbine meter. A blade design that does not change its efficiency with operating conditions, such as velocity, velocity profile, temperature, or density is best. In other words, a design that is minimally sensitive to changes in Reynolds number is optimum [5].

Briefly mentioning about the rest of the parts other than the rotor, swirl is one of the biggest problems to deal with and it should be removed from the flow in the upstream of the turbine meter using the flow straighteners. On the other side drags imposed by the sensors and the friction of the bearings affect the operation of turbine meter greatly. As the drag is reduced, it can operate in a greater range and becomes more linear. As the size of the turbine increases, the drag forces become less important, but drag may drastically limit the operating range of the small turbine meters.

2.6. Standards

Today many standards are applicable for the measurement of flow through the use of turbine flowmeters. The list below gives the most important standards counting for turbine flowmeter measurements.

- AGA Measurement of fuel gas by turbine meters, Transmission Measurement Committee Report, No 7, American Gas Association (1981) (Note first revision November 1984)
- ANSI/ASME MFC-4M-1986 Measurement of gas flow by turbine meters
- ANSI/ISA RP31.1 Recommended practice specification, installation and calibration of turbine flowmeters, Instrument Society of America (1977)
- API Manual of petroleum measurement standards, Chapter 5 - Metering Section 3 - turbine meters, American Petroleum Institute, 1st Ed. (1976)

- API Bull 2509B, Chapter 5.3, turbine meters, 2nd Ed. (1987)
- API Std 2543, Chapter 12.2, calculation of liquid petroleum quantities measured by turbine or displacement meters, 1st Ed. September 1981
- BS 4161 : Part 6:1987 Specification for rotary displacement and turbine meters for gas pressures up to 100 bar
- BS 6866: Part 3:1987 (ISO 7278/3) Methods for pulse interpolation. Three methods commonly used in conjunction with pipe provers and turbine or displacement meters. Test procedures for checking satisfactory operation
- CEN TC237,WG3 1994 European standard for turbine meters. (a mixture of OIML and ISO standards.)
- EEC July 1971: directive 71/318/EEC on gas volume flowmeters including turbine meters.
- IR32 Rotary piston gas meters and turbine gas meters
- ISA Recommended Practice Specification, 'Installation and calibration of turbine flowmeters'
- ISA-RP31.1, Instrument Society of America, Res. Tri. Pk., NC (1977)
- ISO 2715: Part 2:1984 (BS 6169) Turbine meter systems
- ISO/DIS 9951 - 1990, 'Measurement of gas flow in closed conduits - turbine meters' (1990)
- ISO/TC30/SC9, 'Methods of specifying flowmeter performance' (1990)
- ISO/TC30AIVG15 No 42, Draft proposal on: The measurement of gas volumes by turbine meters
- OIML 1974 Recommendation Number 32 for rotary piston and turbine meters.

2.7. Installation and Maintenance

Swirl or non-uniform velocity profiles, such as jetting, at the turbine meter inlet can cause undesirable accuracy performance changes. Sources of these types of flow disturbances can be from the installation piping configuration, an upstream regulator, a throttled valve, or a partial blockage upstream of the meter [24]. The standards mentioned above require a standard perturbation test with the piping configuration shown in Figure 2.15. Double bends out of plane produce swirling flow, with maximum

swirl angles of the order of 20° to 30° . Under this condition the requirement that the error curve will not shift by more than $\pm 0.33\%$ should be met .

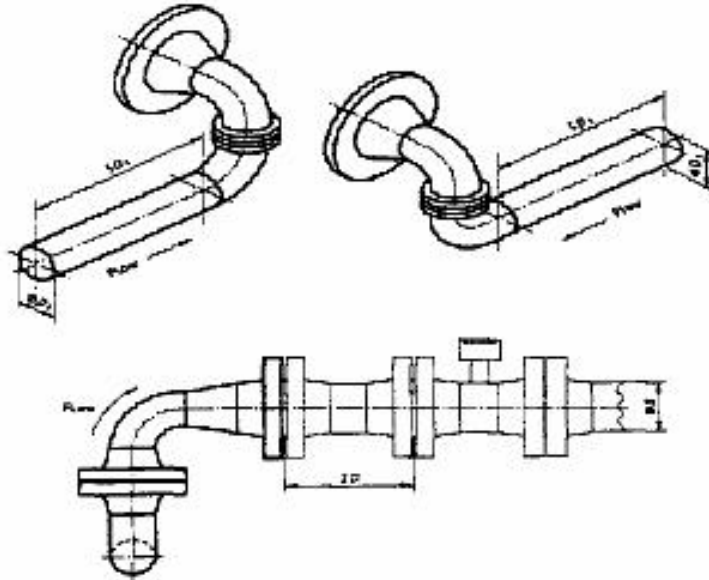


Figure 2.15. Piping configuration to test the sensitivity for installation conditions. [5]

Contamination in the bearings of a turbine flowmeter is the largest single source of poor meter performance. Residues can build up on the bearing surfaces over time and retard the bearings' freedom to rotate. In order to measure the rest of the bearings life a test called spin test is applied. This is also mentioned in different standards to figure out the wornout bearings. This test measures how freely the rotor rotates and how abruptly it stops. When a blow is given, if it takes a large blow to start the meter or it coasts quickly to a stop, the bearings are either worn out or contaminated.

3. Theory

3.1. Basic Flow Phenomena

3.1.1. Drag

As the fluid flows around solid bodies, it generates forces in the horizontal and perpendicular directions. Depending on the shape and the location of the body, these forces sometimes act in a useful manner but in some cases they are not desired. As a turbine meter is considered, drag forces act in both negative and positive manner. Unless the viscosity is considered, the drag caused by the pressure distribution around the blade creates a torque which will be the driving torque for the turbine meter. If this was the only force creating the torque on the blades and assuming no mechanical retarding torque, the turbine meter would be exactly linear. However another form of drag which is generated from the viscous forces on the walls of the blade acts in the way to slow down the blades. Along with the other retarding moments viscous drag reduces the ideal speed of the blades. Actually this is the most dominant retarding torque among the others.

The resultant force in the direction of the upstream velocity is termed the drag and the resultant force normal to the upstream velocity is termed the lift. These forces are calculated by integrating the pressure and shear stress along the surface of the object in three-dimensional bodies there may also be a side force that is perpendicular to the plane containing D and L [25].

In Figure 3.2 the shear and pressure forces are shown on a small surface element. The x and y components of the fluid force on the small element dA are

$$dF_x = (pdA) \cos \theta + (\tau_w dA) \sin \theta \quad (3.1)$$

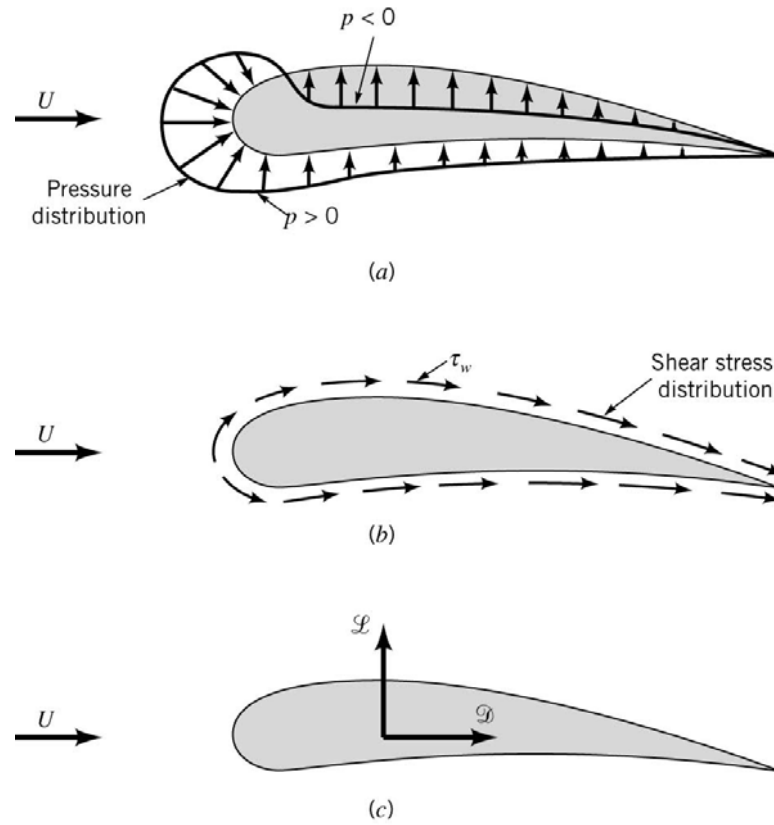


Figure 3.1. Forces from the surrounding fluid on a two dimensional object a)pressure force b)viscous force c) resultant force (lift and drag) [25]

and

$$dF_y = -(pdA) \sin \theta + (\tau_w dA) \cos \theta \quad (3.2)$$

and the net force components on the object are

$$D = \int dF_x = \int p \cos \theta dA + \int \tau_w \sin \theta dA \quad (3.3)$$

and

$$L = \int dF_y = - \int p \sin \theta dA + \int \tau_w \cos \theta dA \quad (3.4)$$

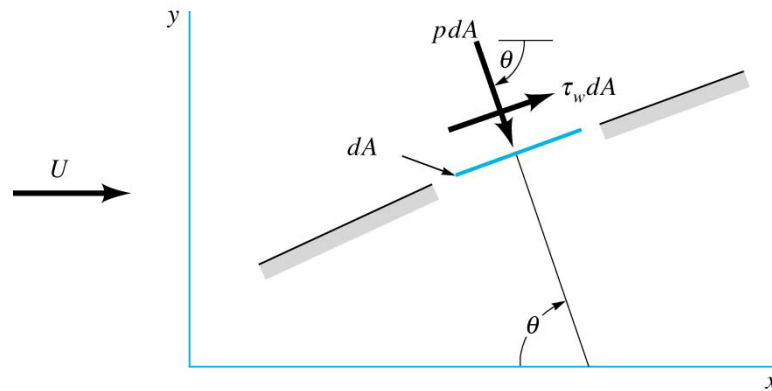


Figure 3.2. Pressure and shear forces on a small element of the surface of a body [25]

The drag coefficient and lift coefficient are defined as:

$$C_L = \frac{L}{\frac{1}{2}\rho U^2 A} \quad (3.5)$$

and

$$C_D = \frac{D}{\frac{1}{2}\rho U^2 A} \quad (3.6)$$

where A is the characteristic area of the object.

3.1.1.1. Pressure Drag. Pressure drag D_p , is the part of the drag that is due directly to the pressure, p , on an object. It is often referred to as form drag because of its strong dependency on the shape or form of the object. Pressure drag is a function of the magnitude of the pressure and the orientation of the surface element on which the pressure force acts [25]. The shape of the object over which the fluid flows is the most important design variable effecting the distribution and the magnitude of the pressure on the surface of the object. In other words creating a desired pressure drag force is possible by changing the geometry of the object which is in a flow field. This is a very common challenge generally calculated by numerical simulations.

In order to minimize the pressure drag in subsonic flows, smooth shapes with rounded noses and rear sections are required. If sharp corners exist on the object or cross section of the object changes too quickly, the boundary layer may separate causing the formation of a region of fluid known as the wake. Since the static pressure is lower than it would be, the drag is increased. The following are the basic equations describing the pressure drag.

The pressure drag can be obtained using equation 3.3 with a detailed information on distribution of pressure and the body shape.

$$D_p = \int \cos \theta dA \quad (3.7)$$

Introducing Equation 3.7 into the pressure drag coefficient gives,

$$C_{Dp} = \frac{D_p}{\frac{1}{2}\rho U^2 A} = \frac{\int \cos \theta dA}{\frac{1}{2}\rho U^2 A} = \frac{\int C_p \cos \theta dA}{A} \quad (3.8)$$

where C_p is the pressure coefficient.

$$C_p = \frac{(p - p_0)}{\frac{1}{2}\rho U^2} \quad (3.9)$$

3.1.1.2. Friction Drag . Friction drag, D_f , is that part of the drag that is due directly to the shear stress, τ_w , on the object. It is a function of not only the magnitude of the wall shear stress, but also of the orientation of the surface on which it acts. This is indicated by the factor $\tau_w \sin \theta$ in equation 3.1. If the surface is parallel to the upstream velocity, the entire shear force contributes directly to the drag [25]. This kind of drag is also called as skin-friction drag or viscous drag because of its dependency on the viscosity.

The pipe flow is divided into two distinct categories; laminar or turbulent; with a transitional regime connecting them. The drag coefficient, C_{Df} , is not a function of the plate roughness if the flow is laminar. However, for turbulent flow the roughness

does considerably affect the value of C_{Df} in pipe flow, this dependence is a result of the surface roughness elements protruding into or through the laminar sublayer [25].

The friction drag can be obtained from the wall shear stress distribution. The friction drag coefficient and local friction coefficient are as follows:

$$C_{Df} = \frac{D_f}{\frac{1}{2}\rho U^2 A} \quad (3.10)$$

and local friction coefficient is

$$C_f = \frac{\tau_w}{\frac{1}{2}\rho U^2} \quad (3.11)$$

3.1.2. Basics of The Boundary Layer Theory

In turbulent thin shear layer flows, a Reynolds number based on a length scale is very large (for a case $U = 1 \text{ m/s}$, $L = 0.1 \text{ m}$ and $\nu = 10^{-6} \text{ m}^2/\text{s}$, $Re_L = 10^5$). Since the definition of the Reynolds number is the ratio of inertial forces to viscous effects; at this value of Reynolds number the inertia forces will be dominant. If another Reynolds number based on a distance y away from the wall is formed ($Re_y = Uy/\nu$) then at a value near L the above argument will be valid such that far away from the wall, inertia forces dominate the flow. However, if y is chosen close to the wall Re_y will be small and viscous forces will dominate the flow. If the y is chosen so that $Re_y = 1$ viscous forces will be equal to inertial forces. Briefly, the region far away from the wall is inertial dominated while in the region close to wall viscous effects are dominant [26].

In the near wall region, the flow is affected by viscous effects and free stream relations are not valid. Dimensional analysis for mean flow velocity where $U = f(y, \rho, \mu, \tau_w)$ expresses the following relation

$$u^+ = \frac{U}{u_\tau} = f\left(\frac{\rho u_\tau y}{\mu}\right) = f(y^+) \quad (3.12)$$

This is called law of the wall and contains two new dimensionless groups u^+ and y^+ .

$$u_\tau = \sqrt{\tau_w/\rho} \quad (3.13)$$

$$y^+ = \frac{u_\tau y}{\nu} \quad (3.14)$$

where u_τ is called friction velocity.

Making a dimensional analysis yields

$$u^+ = \frac{U}{u_\tau} = g\left(\frac{y}{\delta}\right) \quad (3.15)$$

Relating the velocity deficit $U_{max} - U$ to the wall shear stress gives

$$\frac{U_{max} - U}{u_\tau} = g\left(\frac{y}{\delta}\right) \quad (3.16)$$

the so called velocity-defect law [26].

3.1.2.1. Linear Sublayer. At the wall, the fluid has no motion even that the turbulent eddying motions stop when they reach very close to the wall. Viscous shear is the only dominant parameter when there is no turbulent shear stress. In practice this layer is so thin that the shear stress is assumed almost constant and equal to the wall shear stress τ_w among the layer. Therefore

$$\tau(y) = \mu \frac{\partial U}{\partial y} \cong \tau_w \quad (3.17)$$

Integrating with respect to y with a boundary condition $U = 0$ at $y = 0$ gives a relationship between the mean velocity and the distance from the wall.

$$U = \frac{\tau_w y}{\mu} \quad (3.18)$$

which leads to $u^+ = y^+$. The linear relationship between velocity and distance from the wall makes this layer named as linear sub-layer [26].

3.1.2.2. Log-law layer. The region in $30 < y^+ < 500$ is exposed to both viscous and turbulent effects. The shear stress τ changes slowly as moving away from the wall and within this region it is assumed to be equal to the wall shear stress. One more assumption about the length scale of turbulence (mixing length $l_m = \kappa y$) leads to a relationship between u^+ and y^+

$$u^+ = \frac{1}{\kappa} \ln y^+ + B = \frac{1}{\kappa} \ln(Ey^+) \quad (3.19)$$

The relation is called the log-law and the region between $y^+ = 30$ and $y^+ = 500$ is called the log-law layer. For smooth walls $\kappa = 0.4$, $B = 5.5$ (or $E = 9.8$) and wall roughness makes B decreased [26].

3.1.2.3. Outer layer. It is seen from experiments that log-law is valid in the region $0.02 < y/\delta < 0.2$. For larger values of y Equation 3.16 (velocity-defect law) provides appropriate form. In the overlap region, the log-law and the velocity-defect law becomes equal. A matched overlap is obtained by assuming the following logarithmic form:

$$\frac{U_{\max} - U}{u_\tau} = \frac{1}{\kappa} \ln \left(\frac{y}{\delta} \right) + A \quad (3.20)$$

where A is constant. This law is called law of the wake.

The mean velocity is at its maximum value far away from the wall and due to no slip condition, it sharply decreases in the region $y/\delta \leq 0.2$. High values of $\overline{u'^2}$, $\overline{v'^2}$, $\overline{w'^2}$ and $\overline{u'v'}$ are found adjacent to the wall where the high turbulence production is ensured by large mean velocity gradients. Eddies and velocity fluctuations are affected from the no-slip condition at the wall. Since the production process mainly creates component $\overline{u'^2}$ the turbulence is anisotropic near the wall. The turbulence properties asymptotically vanishes as y/δ increases above a value of 0.8 . The rms values of all fluctuating

velocities become nearly equal which means the turbulence structure becomes more isotropic far away from the wall [26].

3.1.3. Secondary Flows

Secondary flows (Figure 3.3a) can be considered as small disturbances on a primary flow where the primary flow is the main flow. It can also be considered as unplanned three-dimensional flow effects in a turbine which lead to unexplained (secondary) losses. Whilst the secondary flow is often considered as a small flow superimposed on a larger flow, the secondary flow can be of the same order of magnitude as the primary flow [27].

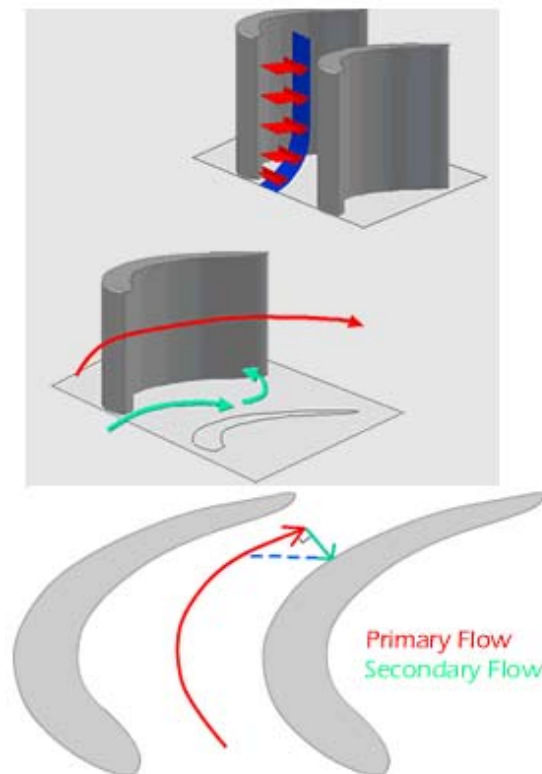


Figure 3.3. Secondary flow and its formation [27]

When a sheared flow such as a boundary layer (Figure 3.3) is forced around a turn the slower moving fluid follows a tighter radius of curvature, leading to a tangential flow across the passage. Then, in order to preserve continuity, a vortical flow is formed. The real situation in turbines is much more complicated but the passage vortex dominates the flow field [27]. Some effects of secondary flows are given below.

- Secondary flow alters the flow angle which causes power losses.
- A non-uniform flow is provided at exit of the blade row.
- Secondary flows can introduce unsteadiness into the flow.

3.1.4. Separation and Wake

When sometimes an object is in a flow field, the streamlines, which are the pathways of the flow and an expression of the flow field, can not attach to the surface of the object around which they align. This means that the streamlines do not completely surround the object and follow a different pathway. The fact that separates the flow field from the boundary of the object is separation [25]. Because of its Reynolds number dependency, it may not happen on the same geometry for different properties of the flow. In low Reynolds numbers where the viscous forces has a strong effect, the streamlines cover the shape of the object resulting in no separation. On the other hand as the Reynolds number increases viscous forces become less dominant and separates from the path of the body.

Since sharp edges cause more separation at the rear part of the blades, secondary flows which effects the sensitivity and the accuracy of the turbine meter, generate at the rear part of the blades. Using rounded shapes instead of a sharp trailing edge not only decrease the flow disturbance by the secondary flows but also results in the increase of turbine meter coefficient (K factor). Figure 3.4 shows the effect of the trailing edges on the flow field.

The separation of the boundary layer initiates the creation of a wake and a wake region with low pressure magnitudes causing the form drag to increase [25]. Wake regions are highly turbulent regions in the downstream. As sharp edges or sudden changes in the shape of the object decrease, narrower wake regions occur. (See figure 3.5)

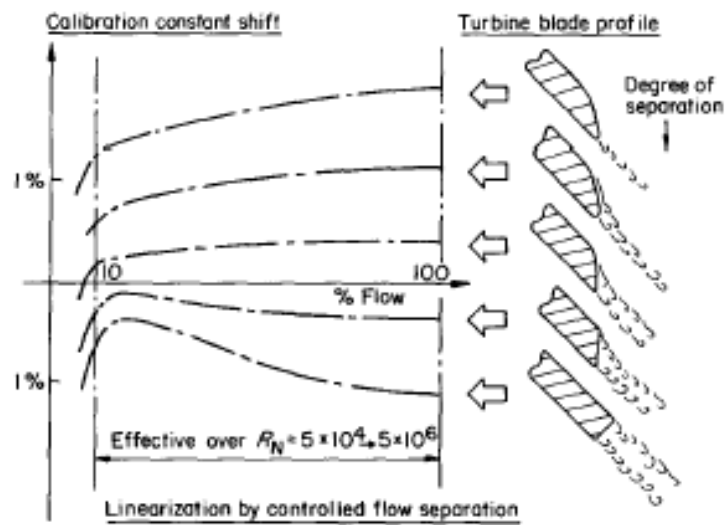


Figure 3.4. Effect of trailing edge on calibration [8]

3.1.5. Stall

Stall happens because of abnormal fluid flow. When the actual incidence angle is greater than the angle of attack, it is possible that blade stall may be occurring in a turbine meter. When large negative incidences occur in the wall boundary layer, those sections of the blade near the tip may be pumping at the tip [28].

There are two general types of compressor stall. The first one is the "axis-symmetric stall", which is mostly a momentary halt of the rotation. The second kind of stall is called "rotational stall" where the flow disruption of the stall causes standing pockets of fluid to rotate within the turbine without moving along the axis.

3.1.6. Tip Leakage Flow

Tip leakage flow is a great interest for many researchers mostly with the aim of increasing the efficiency of a power turbine. Unfortunately due to the wall and the boundary layer of the blade it is very difficult to document and there is not much written about it. It occurs because of the pressure gradient over each blade, so fluid does not follow the intended path of the flow, instead it escapes through the main passages of the turbine and leaks through this clearance gap.

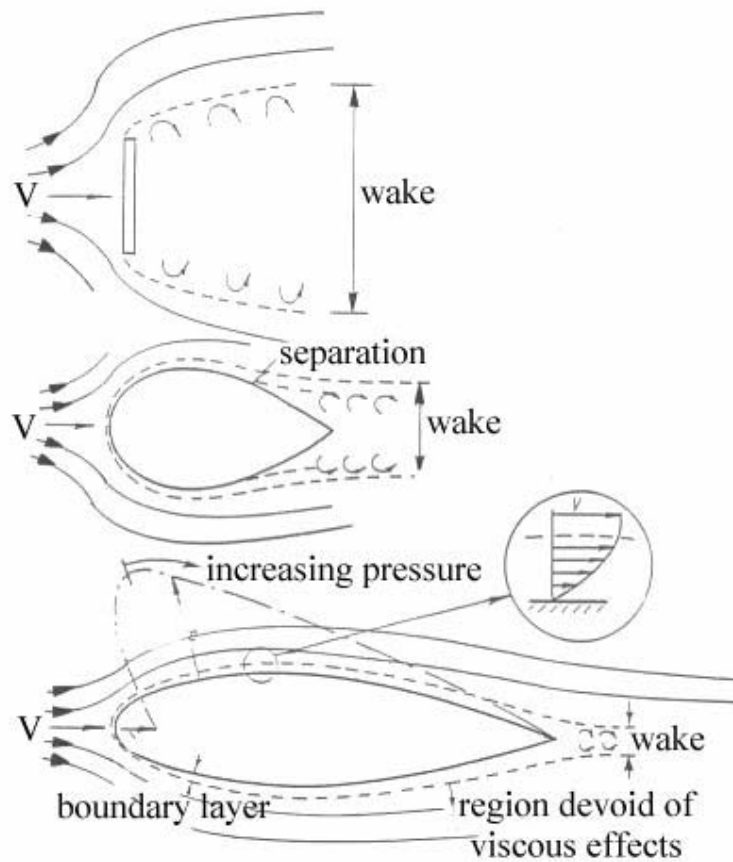


Figure 3.5. Flow past progressively more streamlined bodies [28]

The relative motion between blades and casing leads to the development of a scraping vortex that, along with the secondary flow, reduces the propagation of the tip leakage flow into the main flow. The rotational effects and coriolis forces modify the turbulence structure in the tip leakage flow and secondary flow as compared to cascades [29].

3.2. Turbine Meter Theories

There are two approaches described in the current literature for analyzing axial turbine performance. The first approach describes the fluid driving torque in terms of momentum exchange, while the second describes it in terms of aerodynamic lift via airfoil theory. The former approach has the advantage that it readily produces analytical results describing basic operation, some of which have not appeared via airfoil analysis. The latter approach has the advantage that it allows more complete descriptions using

fewer approximations. However, it is mathematically intensive and leads rapidly into computer generated solutions. One prominent pioneer of the momentum approach is Lee [35] who, using this approach, later went on to invent one of the few, currently successful, dual rotor turbine flowmeters, while Thompson and Grey [36] provided one of the most comprehensive models currently available using the airfoil approach [12]. Before going into details of the two approaches, an ideal gas turbine meter model may be very useful to introduce since it makes up the basics of both models.

3.2.1. Ideal Gas Turbine Meter

The ideal turbine meter would have no retarding forces, infinitely thin rotor blades, total driving force concentrated at the mean blade radius and a uniform fluid velocity distribution entering the blades in an axial direction [14]. This is the case when an inviscid flow is around the blade and all the mechanical friction forces are assumed to be zero.

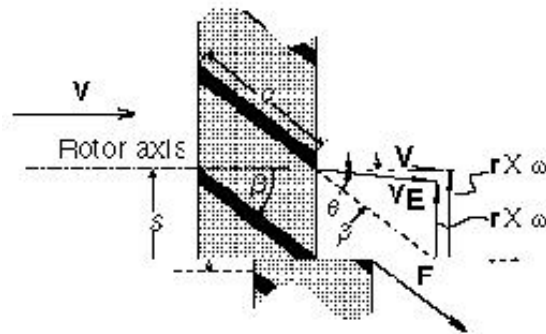


Figure 3.6. Vector diagram for a flat-bladed axial turbine rotor [12]

From the velocity diagram (Figure 3.6) it can be seen that for the ideal turbine meter, the rotational speed of the rotor would be:

$$w_i = \frac{\tan \beta Q}{\bar{r}A} \quad (3.21)$$

where \bar{r} = root mean square of the inner and outer blade radius, (R, a) , A= Annular flow area, β = the blade angle, Q = the volume flow rate, w_i = the ideal rotational speed of the rotor.

If the real turbine meter is considered, it would rotate slower than the ideal one due to the mechanical frictions as well as fluid drag on the blades. The ratio w/w_i would indicate the percent registration of the actual meter to the ideal meter. This percent registration can be equated to the ratio of the driving forces to the retarding forces [14].

$$\frac{w}{w_i} = PR = 1 - \frac{KN_T}{T_d} \text{ where } T_d \propto \rho Q^2 \text{ and } K \text{ is a constant} \quad (3.22)$$

3.2.2. Momentum Theory

This theory is also referred to as cascade theory. The most important pioneers of this approach are Lee, Tsukamoto and Hutton. First the meter factor will be derived as it is derived by Lee [35] then the mathematical model of the driving torque will be given as it is explained by Tsukamoto and Hutton [37].

The difference between the ideal (subscript i) and actual tangential velocity vectors is the rotor slip velocity and is caused by the net effect of the rotor retarding torques. This gives rise to linearity errors and creates swirl in the exit flow. V incident fluid velocity vector; V_E exit fluid velocity vector; θ exit flow swirl angle due to rotor retarding torques; β blade pitch angle, same as angle of attack for parallel flow; ω rotor angular velocity vector; r rotor radius vector; F flow induced drag force acting on each blade surface; c blade chord; s blade spacing along the hub; c/s rotor solidity factor [12].

Eliminating the time dimension from the left hand side quantity reduces it to the number of rotor rotations per unit fluid volume, which is essentially the flowmeter K factor specified by most manufacturers. Hence, according to equation 3.21 , in the ideal situation the meter response is perfectly linear and determined only by geometry. (In some flowmeter designs the rotor blades are helically twisted to improve efficiency. This is especially true of blades with large radius ratios, (R/a) . If the flow velocity profile is assumed to be flat, then the blade angle in this case may be described by $\frac{\tan \beta}{r} = \text{constant}$. This is sometimes called the 'ideal' helical blade.) In practice, there are instead a number of rotor retarding torques of varying relative magnitudes [12]. Under steady flow the rotor assumes a speed which satisfies the following equilibrium:

$$T_d = T_B + T_w + T_t + T_h + T_s \quad (3.23)$$

where T_d is the driving torque, T_B is the bearing drag, T_w is the hub disc friction drag torque, T_t is the blade tip clearance drag torque, T_h is the hub fluid drag torque, T_s is the rotation sensor's drag torque. This equation (Equation 3.23) is true for both theories and make the basis for both of them. As the rotation speed increases T_B , T_w , T_t and T_s will be less important and can be ignored in calculations [23].

Because of the retarding forces the blade rotates slower than it would, this causes the rotor slip velocity which is the difference between the actual rotational speed and the ideal one. Because of the retarding forces described in equation 3.23 and shown in figure 3.9 the fluid velocity vector is deflected through an exit or swirl angle, θ . Denoting the radius variable by r , and equating the total rate of change of angular momentum of the fluid passing through the rotor to the retarding torque, one obtains:

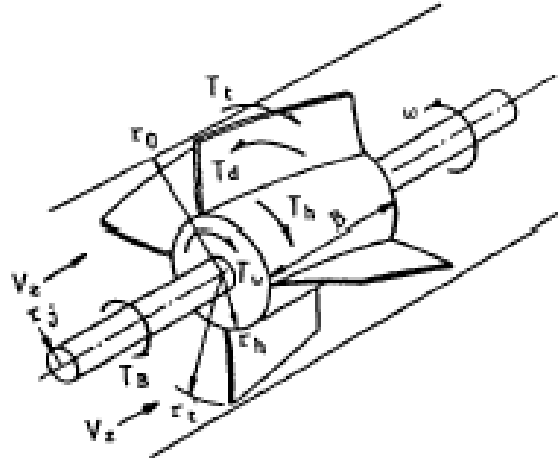


Figure 3.7. General view of a turbine rotor and torques on the rotor [23]

$$\int_a^R \frac{\rho Q 2\pi r^2 (r w_i - r w)}{\pi(R^2 - a^2)} dr = N_T \quad (3.24)$$

$$\text{which yields: } r^{-2} \rho Q (w_i - w) = N_T \quad (3.25)$$

where ρ is the fluid density and N_T is the total retarding torque. Combining equations 3.21 and 3.25 and rearranging, yields:

$$\frac{w}{Q} = \frac{\tan \beta}{\bar{r} A} - \frac{N_T}{\bar{r}^2 \rho Q^2} \quad (3.26)$$

Under normal operating conditions T_B , T_w , T_t and T_s will be so small compared with the torque due to induced drag across the blade surfaces. As shown in figure 3.6, the force, F , due to this effect acts in a direction along the blade surface and has a

magnitude given by:

$$F = \frac{\rho V^2}{2} C_D S \quad (3.27)$$

where C_D is the drag coefficient and S is the blade surface area per side. Using the expression for drag coefficient corresponding to turbulent flow, selected by Pate et al. [38] and others, this force may be estimated by:

$$F = \rho V^2 0.074 Re^{-0.2} S \sin \beta \quad (3.28)$$

where Re is the flow Reynolds number based on the blade chord shown as dimension c in figure 3.6. Assuming θ is small compared with β , then after integration, the magnitude of the retarding torque due to the induced drag along the blade surfaces of a rotor with n blades is found to be:

$$N_D = n(R + a)\rho V^2 0.037 Re^{-0.2} S \sin \beta \quad (3.29)$$

Combining equations 3.28 and 3.26, and rearranging yields:

$$\frac{w}{Q} = \frac{\tan \beta}{\bar{r}A} - \frac{0.036n(R + a)SA^2 Re^{-0.2} \sin \beta}{\bar{r}^2 \rho Q^2} \quad (3.30)$$

In order to find the driving torque on the rotor Tsukamoto and Hutton [37] gives the following equation.

$$T_d = \int_{r_h}^{r_t} r V_z^2 s (\tan \beta_2 - \tan \beta_1) dr \quad (3.31)$$

where β_1 is the relative inlet angle of flow, β_2 is the relative outlet angle of flow and s is the blade spacing. Replacing β_1 by $\beta - i$ and β_2 by $\beta - \delta$, noting both δ (deflection of flow at blade outlet from blade angle) and i (incidence angle) are small.

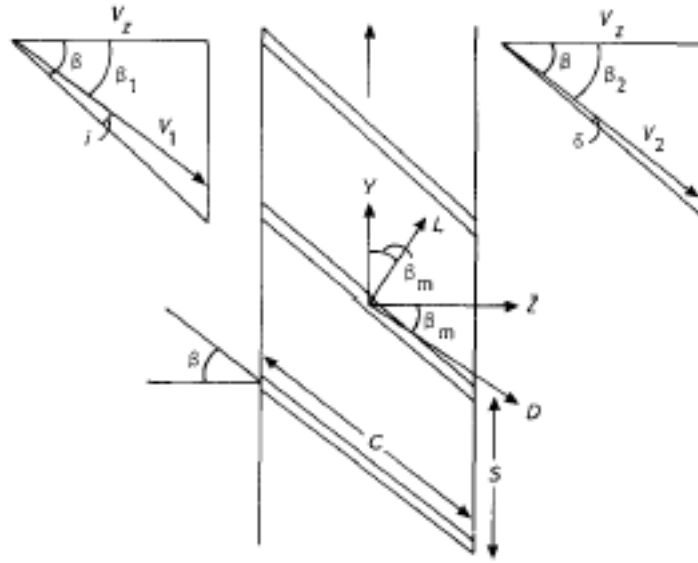


Figure 3.8. Cascade angles, dimensions and forces [23]

The equation may be re-written as:

$$T_d = \rho N \int_{r_h}^{r_t} r V_z^2 s (i - \delta) (1 + \tan^2 \beta) dr \quad (3.32)$$

The derivation of this equation is shown in details in the reference of Baker et. al. [23].

3.2.3. Airfoil Theory

The alternative airfoil theory approach is to use lift and drag coefficients. These are given per unit length of the blade.

$$L = \frac{1}{2} \rho c K C_L \left(\frac{V_z}{\cos \beta_m} \right)^2 \quad \text{and} \quad D = \frac{1}{2} \rho c K C_D \left(\frac{V_z}{\cos \beta_m} \right)^2 \quad (3.33)$$

where K is the factor which allows for the change in lift coefficient between an isolated aerofoil and a cascade. The torque on the rotor is now given by:

$$T_d = \frac{1}{2} \rho N \int_{r_h}^{r_t} \frac{r V_z^2 c}{\cos \beta_m} (K C_L - \tan \beta_m C_D) dr \quad (3.34)$$

Equation 3.34, which is written as the lift torque minus the drag torque, and equation 3.31 are considered to be the same. The derivation of their equality is given in details in the reference of Baker et. al. [23].

The theoretical expression given for the lift coefficient is:

$$C_L = 2\pi \sin \alpha \text{ and } C_L = 2\pi \sin i/2 \text{ for } \alpha = i/2 \quad (3.35)$$

$$K C_L = \frac{s}{c} \frac{4 \sin i/2}{\cos \beta} \cong \frac{s}{c} \frac{2i}{\cos \beta} \text{ for } K = \frac{s}{c} \frac{2}{\pi \cos \beta} \quad (3.36)$$

$$\frac{\tan(\beta - i) + \tan(\beta - \delta)}{2} = \tan \beta_m \text{ so that } \beta_m \cong \beta - \frac{i + \delta}{2} \quad (3.37)$$

$$\beta - \alpha = \beta_m \text{ so } \alpha = \frac{i + \delta}{2} \text{ and } C_L = 2\pi \left(\frac{i + \delta}{2} \right) = \pi(i + \delta) \quad (3.38)$$

$$\text{Hence } T_d = \frac{1}{2} \rho N \int_{r_h}^{r_t} \frac{r V_z^2 c}{\cos \beta_m} [K \pi (i + \delta) - \tan \beta_m C_D] dr \quad (3.39)$$

For a well designed turbine meter C_D is small and δ may also be neglected. So the equation simplifies to:

$$T_d = \frac{\pi}{2} \rho N \int_{r_h}^{r_t} \frac{r V_z^2 c K(r) i(r)}{\cos \beta_m} dr \quad (3.40)$$

A detailed derivation without neglecting C_D and δ can be found in the reference of Baker et. al. [23].

3.3. Governing Equations of Fluid Dynamics

The conservation laws of fluid dynamics are the basis for the governing equations of fluid motion. The principle of continuity which is the conservation of mass, the momentum equations from the Newton's second law, and the energy equation from the first law of thermodynamics make up the governing fluid dynamics equations.

The law of conservation of mass forms the basis of what is called the principle of continuity. This principle states that the rate of increase of the fluid mass contained within a given space must be equal to the difference between the rates of influx into and efflux out of space. The assumption of a continuous fluid medium then permits this principle to be expressed in differential form. In cartesian coordinates the exact equation becomes equation 3.41 [30]. Equation 3.42 is a more compact representation in vector notation.

$$\frac{\partial(\rho u)}{\partial x} + \frac{\partial(\rho v)}{\partial y} + \frac{\partial(\rho w)}{\partial z} = -\frac{\partial \rho}{\partial t} \quad (3.41)$$

$$\frac{\partial \rho}{\partial t} = -div(\rho u) \quad (3.42)$$

Assuming the rates of increase of x, y and z momentum per unit volume of a fluid particle are $\rho \frac{Du}{Dt}$, $\rho \frac{Dv}{Dt}$ and $\rho \frac{Dw}{Dt}$ respectively, the x-component of momentum equation is derived by setting the rate of change of x-momentum equal to the addition of the net force in x-direction on the element due to stresses with the rate of increases of x-momentum due to sources (S_{Mx} represents body forces, in literature it is also used as ρg_x). The y and z components of the momentum are shown in equations 3.43b and 3.43c respectively [26].

$$\rho \frac{Du}{Dt} = \frac{\partial(-p + \tau_{xx})}{\partial x} + \frac{\partial \tau_{yx}}{\partial y} + \frac{\partial \tau_{zx}}{\partial z} + S_{Mx} \quad (3.43a)$$

$$\rho \frac{Dv}{Dt} = \frac{\partial \tau_{xy}}{\partial x} + \frac{\partial(-p + \tau_{yy})}{\partial y} + \frac{\partial \tau_{zy}}{\partial z} + S_{My} \quad (3.43b)$$

$$\rho \frac{Dw}{Dt} = \frac{\partial \tau_{xz}}{\partial x} + \frac{\partial \tau_{yz}}{\partial y} + \frac{\partial(-p + \tau_{zz})}{\partial z} + S_{Mz} \quad (3.43c)$$

The principal of conservation of energy can be stated for the fluid within a control volume by considering the following energy changes and work occurring during a small time period in a control volume (C.V.) [31].

$$\left(\begin{array}{c} \text{Increase} \\ \text{of Energy} \\ \text{within C.V.} \end{array} \right) = \left(\begin{array}{c} \text{Net Energy} \\ \text{Transported} \\ \text{into the C.V.} \end{array} \right) + \left(\begin{array}{c} \text{Energy added} \\ \text{to the C.V. by} \\ \text{Heat Transfer} \end{array} \right) + \left(\begin{array}{c} \text{Energy increase by} \\ \text{work done on the} \\ \text{fluid in the C.V.} \end{array} \right)$$

The mathematical form of energy equation is shown in equation 3.44.

$$\rho \frac{DE}{Dt} = S_E + \frac{\partial}{\partial x}[u\tau_{xx} + v\tau_{xy} + w\tau_{xz}] + \frac{\partial}{\partial y}[u\tau_{yx} + v\tau_{yy} + w\tau_{yz}] + \frac{\partial}{\partial z}[u\tau_{zx} + v\tau_{zy} + w\tau_{zz}] - \text{div}(\rho u) + \text{div}(k \text{ grad } T) \quad (3.44)$$

3.3.1. Navier-Stokes Equations

The Navier-Stokes equations are a set of nonlinear partial differential equations that describe the flow of fluids. They are time-dependent and consist of a continuity equation for conservation of mass, three conservation of momentum equations and a conservation of energy equation. There are four independent variables in the equation - the x , y , and z spatial coordinates, and the time t ; six dependent variables - the pressure p , density ρ , temperature T , and three components of the velocity vector u . Together with the equation of state such as the ideal gas law $pV = nRT$, the six equations are just enough to determine the six dependent variables. In general, all of the dependent variables are functions of all four independent variables. Usually, the Navier-Stokes equations are too complicated to be solved in a closed form. However, in some special cases the equations can be simplified and may admit analytical solutions [32].

The viscous stresses originate from the friction between the fluid and the surface of an element. They depend on the dynamical properties of the medium. For fluids like air or water which are now called as Newtonian fluids, Isaac Newton stated that the shear stress is proportional to the velocity gradient. The viscous stresses are defined by the following relations [33].

$$\begin{aligned}
\tau_{xx} &= 2\mu \frac{\partial u}{\partial x} + \lambda \operatorname{div} \mathbf{u}, & \tau_{yy} &= 2\mu \frac{\partial v}{\partial y} + \lambda \operatorname{div} \mathbf{u}, \\
\tau_{zz} &= 2\mu \frac{\partial w}{\partial z} + \lambda \operatorname{div} \mathbf{u}, & \tau_{xy} &= \tau_{yx} = \mu \left(\frac{\partial u}{\partial y} + \frac{\partial v}{\partial x} \right), \\
\tau_{xz} &= \tau_{zx} = \mu \left(\frac{\partial u}{\partial z} + \frac{\partial w}{\partial x} \right), & \tau_{yz} &= \tau_{zy} = \mu \left(\frac{\partial v}{\partial z} + \frac{\partial w}{\partial y} \right),
\end{aligned} \tag{3.45}$$

Substituting the shear stresses of equation 3.45 into equations 3.43a, 3.43b and 3.43c gives the Navier-Stokes equations.

$$\begin{aligned}
\rho \frac{Du}{Dt} &= -\frac{\partial p}{\partial x} + \frac{\partial}{\partial x} \left[2\mu \frac{\partial u}{\partial x} + \lambda \operatorname{div} \mathbf{u} \right] + \frac{\partial}{\partial y} \left[\mu \left(\frac{\partial u}{\partial y} + \frac{\partial v}{\partial x} \right) \right] \\
&\quad + \frac{\partial}{\partial z} \left[\mu \left(\frac{\partial u}{\partial z} + \frac{\partial w}{\partial x} \right) \right] + S_{Mx}
\end{aligned} \tag{3.46a}$$

$$\begin{aligned}
\rho \frac{Dv}{Dt} &= -\frac{\partial p}{\partial y} + \frac{\partial}{\partial x} \left[\mu \left(\frac{\partial u}{\partial y} + \frac{\partial v}{\partial x} \right) \right] + \frac{\partial}{\partial y} \left[2\mu \frac{\partial v}{\partial y} + \lambda \operatorname{div} \mathbf{u} \right] \\
&\quad + \frac{\partial}{\partial z} \left[\mu \left(\frac{\partial v}{\partial z} + \frac{\partial w}{\partial y} \right) \right] + S_{My}
\end{aligned} \tag{3.46b}$$

$$\begin{aligned}
\rho \frac{Dw}{Dt} &= -\frac{\partial p}{\partial z} + \frac{\partial}{\partial x} \left[\mu \left(\frac{\partial u}{\partial z} + \frac{\partial w}{\partial x} \right) \right] + \frac{\partial}{\partial y} \left[\mu \left(\frac{\partial v}{\partial z} + \frac{\partial w}{\partial y} \right) \right] \\
&\quad + \frac{\partial}{\partial x} \left[2\mu \frac{\partial w}{\partial z} + \lambda \operatorname{div} \mathbf{u} \right] + S_{Mz}
\end{aligned} \tag{3.46c}$$

3.3.2. General Transport Equations

Basic conservation laws for mass, momentum, energy, etc. are described by differential equations. For any flow problem initial and boundary conditions have to be specified. In addition, empirical and problem-specific models are applied to describe phenomena like turbulence or combustion. One important equation that covers a wide

range of flow problems is the general transport equation which essentially states a balance of flows caused by different physical phenomena such as advection, diffusion, etc.; where ϕ is the transported quantity. As it is seen in figure 3.6 net rate of increase of ϕ plus net rate of decrease due to diffusion through the boundaries should be the same as the rate of decrease due to advection through the boundaries plus the net rate of creation of ϕ [34].

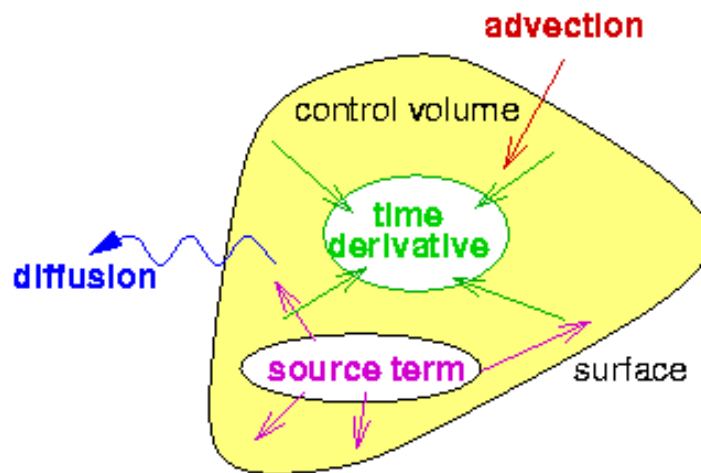


Figure 3.9. General transport equation: balance of flows [34]

$$\int_A \mathbf{n} \cdot (\rho \phi \mathbf{u}) dA + \int_{CV} (\rho \phi) dV t = \int_{CV} S_\phi dV + \int_A \mathbf{n} \cdot (\Gamma_\phi \text{grad } \phi) dA \quad (3.47)$$

4. Numerical Simulation Approach

4.1. CFD

CFD predicts fluid flows and their effects quantitatively making approximations. Its history started in the early 1970's. Since then it has been a powerful alternative besides analytical and experimental approaches in order to investigate the fluid flows.

The beginning of CFD was triggered by the availability of increasingly more powerful mainframes and the advances in CFD are still tightly coupled to the evolution of computer technology. Thanks to the rapidly increasing speed of supercomputers and due to the development of a variety of numerical acceleration techniques like multigrid , it was possible to compute inviscid flows past complete aircraft configurations or inside of turbomachines. With the mid 1980's, the focus started to shift to the significantly more demanding simulation of viscous flows governed by the Navier-Stokes equations. Together with this, a variety of turbulence models evolved with different degree of numerical complexity and accuracy [33].

Nowadays, CFD methodologies are routinely employed in the fields of aircraft, turbomachinery, car and ship design. CFD methods are concerned with the solution of equations of motion of the fluid as well as with the interaction of the fluid with solid bodies. The equations of motion of an inviscid fluid (Euler equations) and of viscous fluid (Navier-Stokes equations), the so-called governing equations, are formulated by different approaches [33].

4.1.1. Spatial Discretisation

Discretisation concerns the process of transferring continuous models and equations into discrete counterparts. When the discretisation of the domains concerned then it would be called spatial discretisation. Spatial discretisation process is usually carried out as a first step toward making them suitable for numerical evaluation.

As long as CFD is concerned the spatial discretisation of the Euler equations (inviscid fluid) and the Navier-Stokes (viscous fluid) equations are the main subjects. Many different methodologies were devised for this purpose in the past and the development still continues. Spatial discretisation schemes may be divided into three main categories: finite difference, finite element, finite volume. All these methods rely on some kind of grid in order to discretise the governing equations [33].

Except three main groups of spatial discretisation methods, there are also a few other methods which are not used often but superior in some special cases. Spectral Element method and Gridless method are two examples of such approaches.

4.1.1.1. Finite Difference. The finite difference method was among the first methods applied to the numerical solution of differential equations. It was first utilized by Euler, probably in 1768. The finite difference method is directly applied to the differential form of the governing equations. This principle is to employ a Taylor series expansion for the discretisation of the derivatives of the flow variables. An important advantage of the finite difference methodology is its simplicity. Another advantage is the possibility to easily obtain high order approximations, and hence to achieve high-order accuracy of the spatial discretisation. On the other hand, because the method requires a structured grid, the range of application is clearly restricted [33].

4.1.1.2. Finite Element. The finite element method (FEM) was originally employed for structural analysis only. It was first introduced by Turner in 1956. About ten years later, researchers started to use FEM also for the numerical solution of field equations in continuous media. However, only with the beginning of the 90's, did the finite element method gain popularity in the solution of the Euler and the Navier-Stokes equations. FEM as it is in general applied to the solution of the Euler/Navier-Stokes equations, starts with a subdivision of the physical space into triangular or into tetrahedral elements. Thus an unstructured grid has to be generated. FEM method is attractive because of its integral formulation and the use of unstructured grids, which are both preferable for flows in or around complex geometries [33].

4.1.1.3. Finite Volume. The finite volume method directly utilizes the conservation laws- the integral formulation of the Navier-Stokes/Euler equations. It was first employed by McDonald for the simulation of 2-D inviscid flows. The finite volume method discretises the governing equations by first dividing the physical space into a number of arbitrary polyhedral control volumes. The accuracy of the spatial discretisation depends on the particular scheme with which the fluxes are evaluated. The main advantage of the finite volume method is that the spatial discretisation is carried out directly in the physical space. Thus, there are no problems with any transformation between coordinate systems like in the case of the finite difference method. Moreover it is very flexible and can rather easily implemented on structured as well as on unstructured grids. This renders the finite volume method particularly suitable for the treatment of flows in complex geometries [33].

4.1.2. Grid Generation

The governing partial differential equations of fluid dynamics should be solved at each discrete point of the domain. Discretisation of a domain can be accomplished either directly in the physical space or on the transformed computational space. The choice primarily will depend on the numerical scheme to be utilized as well as the domains of solutions. Finite difference equations approximating the partial differential equations are solved within a rectangular, equally spaced grid system. For non-rectangular physical domain, a coordinate transformation to computational space is required. On the other side finite volume and finite element models are integral methods so that the original differential equations are integrated on the physical domain and subsequently, are solved numerically. Therefore, the grid system for the finite volume and the finite element schemes are usually generated directly within the physical space [39].

4.1.2.1. Structured Grid. The distinguishing feature of structured grids is that the grid points in the physical space are mapped in a unique way onto a continuous set of three integers i, j, k (one for each coordinate direction). The set of integers defines

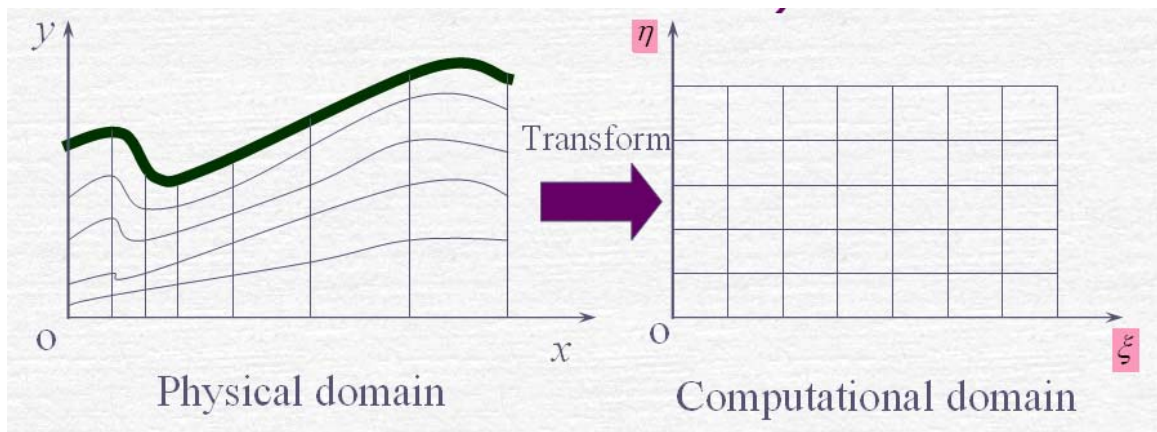


Figure 4.1. Transformation from physical to computational domain [40]

what is called the computational space. The generation of a structured grid starts by distributing grid points along boundary curves (boundaries of surface patches). The usual procedure is to place the nodes more dense in regions with high curvature. Using the point distribution on boundary curves, the surface grid can be generated. Based on the surface grids which enclose the physical domain, we can finally construct the volume grid [33].

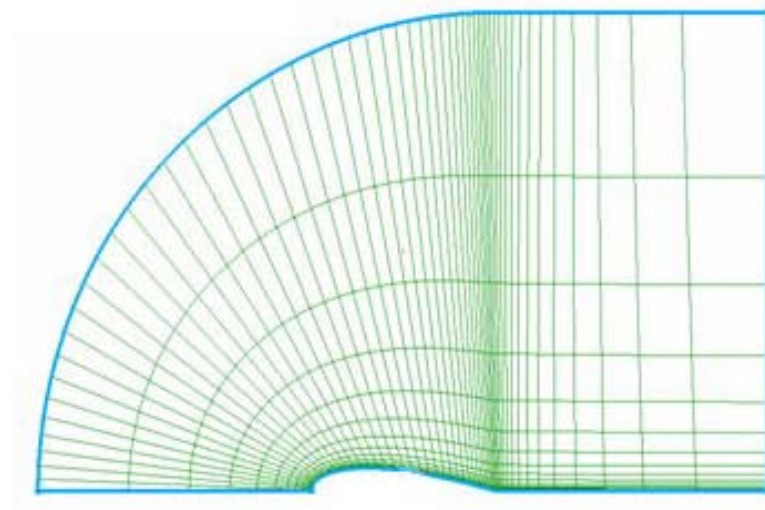


Figure 4.2. Structured grid in 2D [40]

4.1.2.2. Unstructured Grid. Unstructured grids are typically composed of triangles in 2D and of tetrahedra in 3D. However, nowadays it becomes increasingly popular to build unstructured grids from various element types. In figure 4.3 an unstructured

grid of quadrilateral elements is shown. There are also cases when a mixture of different elements are used. For example, hexahedra or prisms are employed to discretise boundary layers. The rest of the flow domain is filled with tetrahedra. Pyramids are used as transitional elements between the hexahedra or the prisms and the tetrahedra. Hence they are named as mixed element grids. In the case of unstructured grids, nodes and grid cells are quasi randomly ordered, i.e., neighbouring cells or grid points can not be directly identified by their indices. This leads to tremendous geometric flexibility of unstructured grids, since the grid does not need to conform to any pre-determined topology.. Furthermore, adaptation of the grid to the physical solution- grid refinement or coarsening - is much easier to accomplish on unstructured than on structured grids [33].

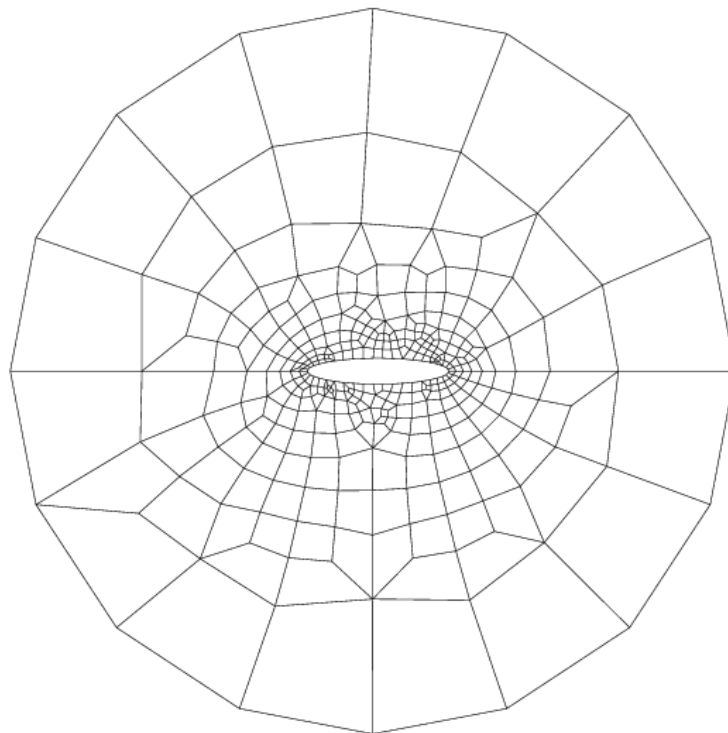


Figure 4.3. Unstructured grid in 2D [41]

4.2. GTM Model

As the aim of this study focuses on a GTM blade design using numerical simulation, it is necessary to create the GTM model as real as possible. Many thanks to Kale Kalip A.S., for providing a solid model of GTM in this study. Although the model is

not a manufactured one, it is very close to a real one as many GTM models in different sizes are produced under the name of Kale Kalip AS. The scope of this study covers an improvement of the 6" GTM blades which is shown in Figure 4.4. The hub radius and the inner casing radius are kept constant while blade pitch angle, the number of blades are the primary design parameters. The tip clearance and the edge profiles of the blades are the secondary design parameters. Unless the computational cost is considered, the best way would be to model and mesh the whole GTM in figure 4.4 and simulate the flow field inside it. Unfortunately it is not possible to simulate even a one flow case in such a model today because of the large computational effort. But some certain methods and simplifications can be applied focusing on the rotor blade design under steady state flow assumption.

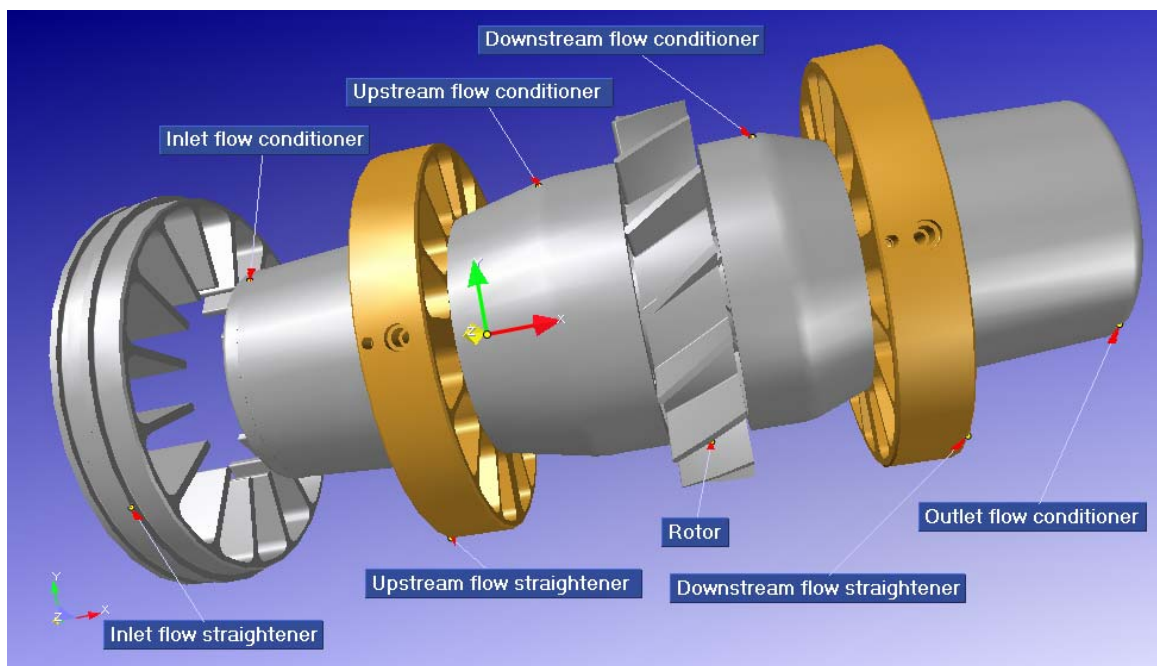


Figure 4.4. Main components of the GTM model provided from the industry

Firstly all the straighteners are designed to eliminate swirl from the flow as it is mentioned earlier in chapter 2. The flow conditioners are to ensure a uniform flow hitting the rotor blades. Since this is no flow straightener or conditioner design process, it is logical to assume a fully developed flow with zero swirl. But it should not be forgotten that the velocity profile changes with the decreasing Reynolds number. Although the flow profile changes in laminar or transitional flows, it is possible to simulate these situations numerically. The primary result of these simulations should be

the angular speed vs. flow rate information. For this purpose the rotor wheel and the conditioners around it are the parts that are enough to gather this information and to simulate the flow field in the rotor. Moreover only modeling the rotor part may give important results in GTM blade improvement process.

Even only modeling and meshing the rotor of the GTM require too much computational effort. As far as the turbomachinery is concerned, a common method in numerical simulation is assuming a periodic flow mostly for steady state cases. That means the flow field repeats itself periodically. This approach is very common in turbomachinery simulations since it only requires a volume around one blade. That drastically reduces the computational cost for the numerical simulation. So assuming a periodic flow field, a volume around one blade is created and meshed, including the tolerances in the rotor.

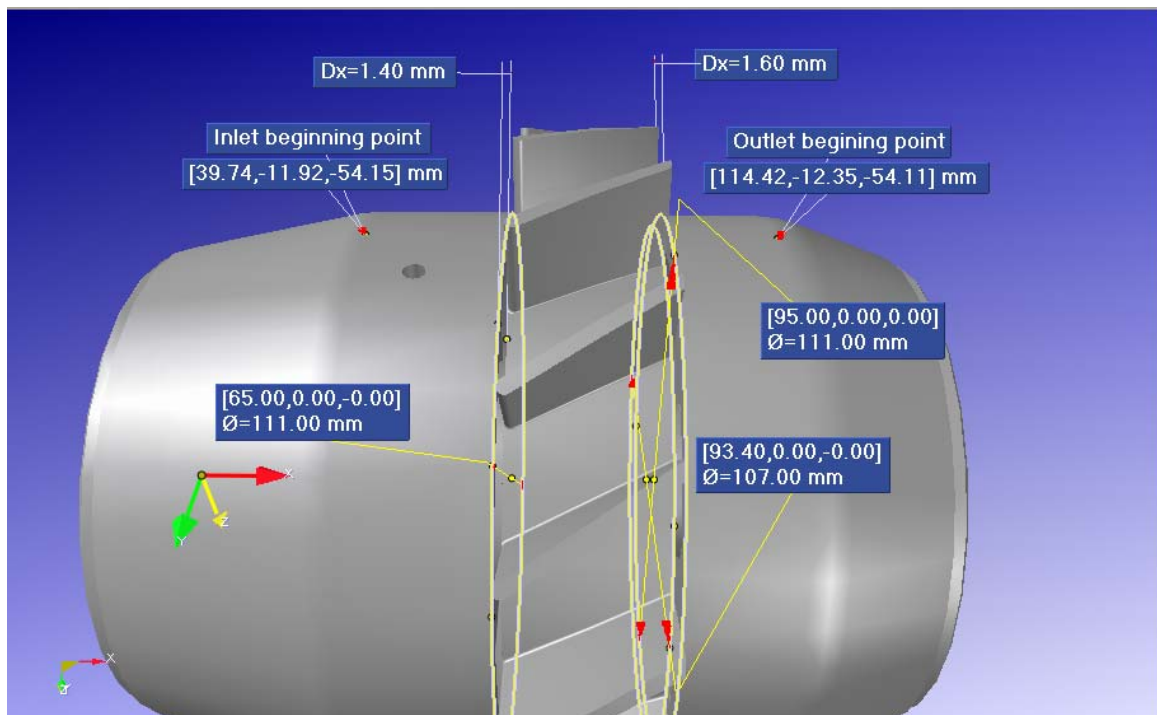


Figure 4.5. A closer look to the provided rotor model and the conditioners around it.
(16 twisted blades with 30 degrees blade pitch angle)

Looking at figure 4.5 one can see the tolerance values used in the rotor wheel. Those tolerances are actually the manufacturing tolerances to ensure the gas flowing through the rotor without hitting any obstacle. There are tolerances of 1.4 and 1.6

mm between the rotor and the upstream,downstream conditioners respectively. The rotor hub radius is smaller than the radius of the conditioners at the rotor side. there is actually a tolerance of 2 mm.

4.3. Gambit as a Preprocessor

GAMBIT is a software package designed to help analysts and designers build and mesh models for Computational Fluid Dynamics (CFD) and other scientific applications. GAMBIT receives user input by means of its graphical user interface (GUI). The GAMBIT GUI makes the basic steps of building, meshing, and assigning zone types to a model simple and intuitive [41]. Additionally it is also possible to write a program in Gambit and run it in batch mode. This property of Gambit makes it a very powerful tool in automated mesh and model generation for Fluent.

The common procedure in creating a mesh for Fluent covers creating the model, assigning zone types and generating the mesh accordingly. Gambit is designed as a pre-processor for Fluent that's why it has zone type assigning feature inside. In other words the boundary conditions such as inlet boundary or periodic boundary can be assigned in Gambit to be used in Fluent. Then the mesh should be generated according to the needs.

There are various tools and options in Gambit for turbomachinery models. There is a GUI option called Turbo which is constructed for turbomachinery models only. GAMBIT turbo operations allow you to model flow scenarios that involve turbomachinery components such as fans or turbochargers. The purpose of such operations is to create and mesh a turbo volume that is, a model composed of one or more real volumes which together represent the flow environment in the region surrounding an individual turbomachinery blade. The turbo volume always includes boundaries that represent the hub, casing, inlet, outlet, and blade and may also include boundaries that represent a splitter turbomachinery component attached to the hub, the purpose of which is to direct flow between the blades [41]. Although Turbo option is a very useful tool in turbomachinery models, it should be noted that it is designed in GUI

and has limitations if it is desired to be used in batch mode. Moreover it should not be forgotten that Turbo option is a result of the programming capability of Gambit.

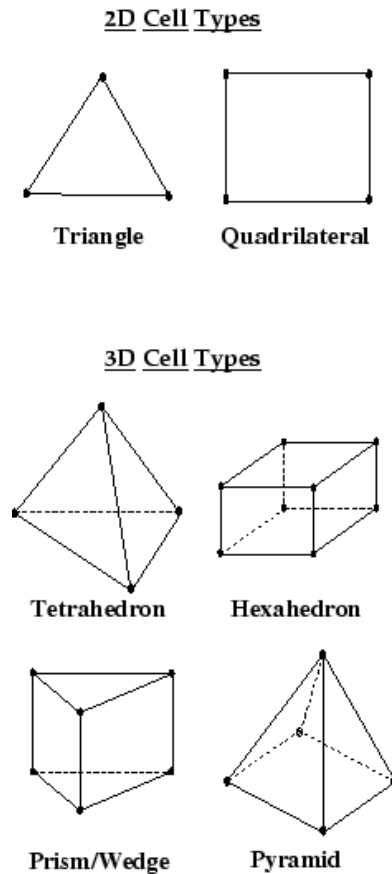


Figure 4.6. Cell types available in Gambit

Figure 4.6 shows the cell types that may be used in Gambit. In meshing geometries, Gambit has various tools such as boundary layers, size functions, and periodic links which are necessary for periodic boundary meshes. The historical order of the meshes are important in Gambit. The first meshes become the sources for the meshes that will be generated afterwards. Becoming a source means the desired mesh will be adapted to the meshes which already exist. If edges, faces and volumes are the elements to be meshed in Gambit, it may be advised starting the meshes on the edges, then on faces and lastly on volumes in order to have a full control of the meshing procedure.

Boundary layers are tools for near wall treatments. They ensure fine mesh elements in the near wall region. The near wall region has critical importance in turbulent flows since the boundary layer theory is applicable on that region. Furthermore, depending on the Reynolds number the boundary layer is usually very thin. Therefore,

the distance from the wall at the wall-adjacent cells must be determined by considering the range over which the log-law is valid. The distance is usually measured in the wall unit, y^+ ($= \rho u_\tau y / \mu$) or y^* . As the Reynolds number increases, the upper bound of the log-layer tends to increase so too large y^+ values are not desirable [41].

Size function is a powerful mesh control tool that may be applied both in GUI and batch mode. It is a kind of source assigning between different elements. It can also be considered as a kind of boundary layer applicable to any kind of geometry element. It is different from the boundary layer in the way that it does not necessarily form a structured grid. For the cases where boundary layers do not fit in the geometry size functions may be a solution.

If the use of periodic field is possible, it has the advantage of less computational cost. In this case a periodic boundary should be used, so that the faces or the edges should be linked for periodicity. This ensures to have the same mesh on either side of the periodic boundaries.

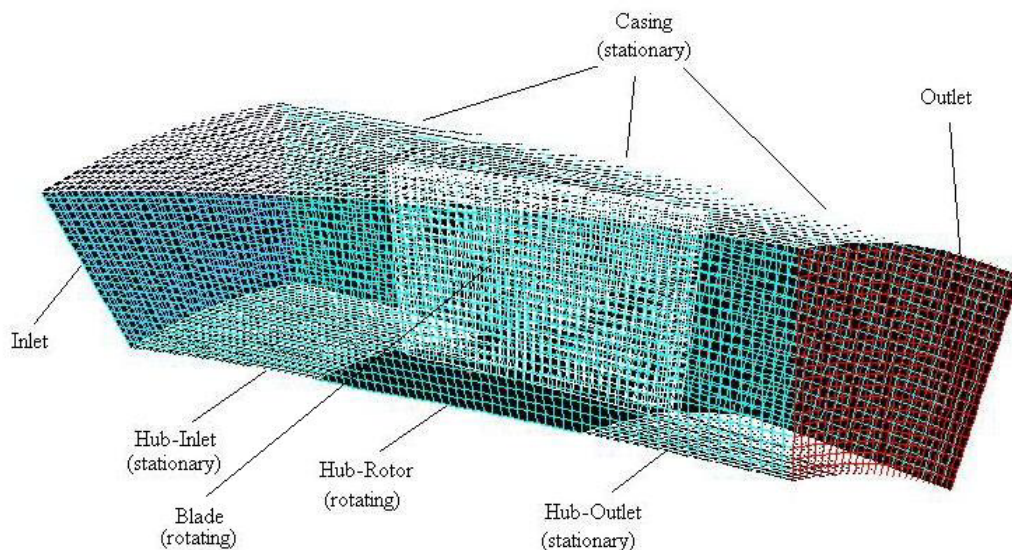


Figure 4.7. GTM model in Gambit

Figure 4.7 shows the GTM model re-drawn in Gambit. As it is compared with the original one, the gaps due to tolerances are omitted. It is easier to draw and mesh such a model. Those tolerances are for manufacturing purposes and have very little effect on the rotation of the rotor since most of the forces occur on the sides of the

blades. In a case where one to one real model is aimed then it is also necessary to draw the housing under the conditioners which is a very complicated structure having very little effect on the rotation of the rotor. Actually the gaps left by the tolerance values do fill up with the gas at the operating condition and stay static during the gas flow.

During the design of turbine meter, some parameters are taken as constant and some considered to be design variables. Table 4.1 shows both the fixed and the variable parameters in the turbine meter design process.

Table 4.1. Fixed and variable design parameters

Fixed Design Parameters	Variable Design Parameters
Hub radius ($r_h = 55.5$ mm)	Blade pitch angle (β)
Casing radius ($r_c = 74$ mm)	Blade numbers (n)
Width of rotor ($W = 30$ mm)	Tip clearance
Width of the conditioners	Trailing and leading edge profiles
Thickness of the blades ($t = 2.5$ mm)	

4.4. Fluent as a Solver

Fluent is a computer program, which is written in C computer language, for modeling fluid flow and heat transfer in complex geometries. It is not only a solver but also a post-processor. All functions required to compute a solution and display the results are accessible in Fluent through a menu-driven interface. The results can also be exported to other post-processor programs. Basically, Fluent has the following modeling capabilities : 2D planar, 2D axisymmetric, 2D axisymmetric with swirl (rotationally symmetric), and 3D flows ; quadrilateral, triangular, hexahedral (brick), tetrahedral, prism (wedge), pyramid, and mixed element meshes; inviscid, laminar, and turbulent flows; steady-state or transient flows; heat transfer, including forced, natural, and mixed convection, conjugate (solid/fluid) heat transfer and radiation [41].

For all flows Fluent solves conservation equations for mass and momentum. For flows involving heat transfer or compressibility, an additional equation for energy conservation is solved. For flows involving species mixing or reactions, a species

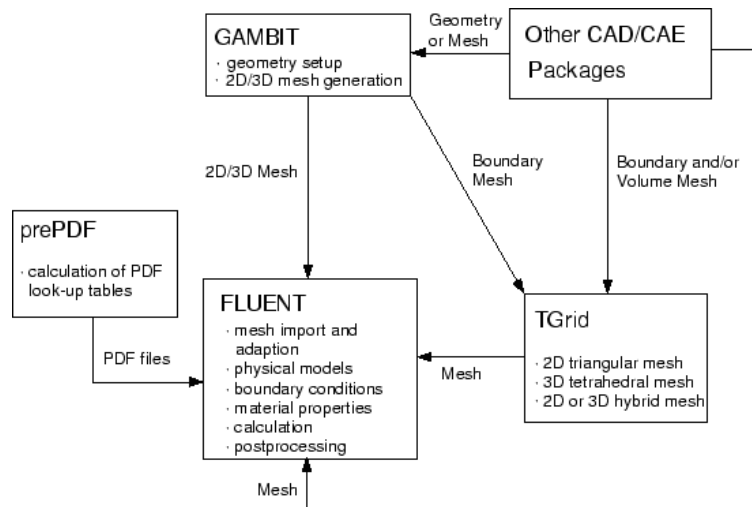


Figure 4.8. Basic program structure [41]

conservation-equation is solved or, if the non-premixed combustion model is used, conservation equations for the mixture fraction and its variance are solved. Additional transport equations are also solved when the flow is turbulent [41].

FLUENT provides three different solver formulations: segregated, coupled implicit, coupled explicit. The segregated and coupled approaches differ in the way that the continuity, momentum, and (where appropriate) energy and species equations are solved: the segregated solver solves these equations sequentially (i.e., segregated from one another), while the coupled solver solves them simultaneously (i.e., coupled together). Both formulations solve the equations for additional scalars (e.g., turbulence or radiation quantities) sequentially. The implicit and explicit coupled solvers differ in the way that they linearize the coupled equations. The segregated solver traditionally has been used for incompressible and mildly compressible flows. The coupled approach, on the other hand, was originally designed for high-speed compressible flows. [41].

For the cases when the mesh is not fine enough or y^+ values are above expected, it may be desired to refine the mesh near the walls. For this purpose a y^+ adaptation option can be used through an upper and lower limit for y^+ . It is also possible to coarsen the meshes if it is too fine.

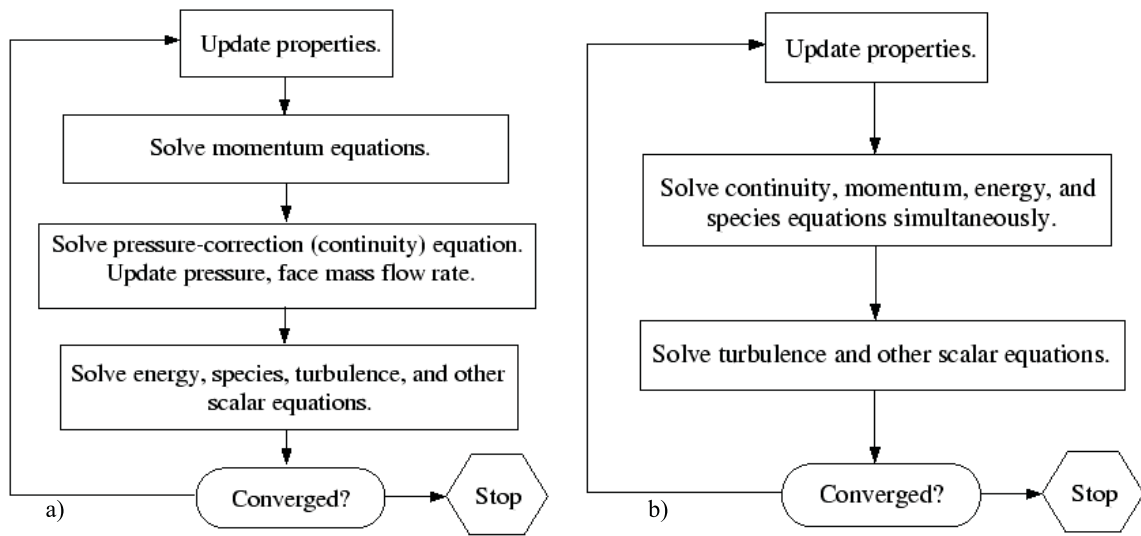


Figure 4.9. a) Segregated solver structure b) Coupled solver structure [41]

In turbomachinery applications rotational reference frames are very demanding approaches. In these approaches periodic boundaries should be generated beforehand. The following section deals with the rotating reference frame models in Fluent.

4.4.1. Rotating Reference Frames

When a model is created using FLUENT, it is typically modeling the flow in an inertial reference frame (i.e., in a non-accelerating coordinate system). However, FLUENT also has the ability to model flows in an accelerating reference frame. In this situation, the acceleration of the coordinate system is included in the equations of motion describing the flow. Many rotating flows can be modeled in a coordinate system that is moving with the rotating equipment and thus experiences a constant acceleration in the radial direction. There are 4 rotating reference frame models which are Single Reference Frame (SRF), Multiple Reference Frame (MRF), Mixing Plane, and Sliding Mesh. SRF is a simpler case of MRF and applied when there is no stator and rotor interaction. So MRF includes SRF. MRF, mixing plane and sliding mesh methods are actually the three rotating reference models available in Fluent [41].

When the equations of motion are solved in a rotating frame of reference, the acceleration of the fluid is augmented by additional terms that appear in the momentum

equations. FLUENT allows to solve rotating frame problems using either the absolute velocity, \bar{u} , or the relative velocity, \bar{u}_r , as the dependent variable. The two velocities are related by the following equation:

$$\bar{u}_r = \bar{u} - (\bar{\omega} \times \bar{r}) \quad \text{where } \bar{r} = \bar{x} - \bar{x}_o \quad (4.1)$$

where \bar{u}_r is the relative speed vector; \bar{u} is the velocity vector; $\bar{\omega}$ is the rotational speed and \bar{r} is the position vector.

The position vector relative to the origin of the zone rotation axis is shown in Figure 5.1

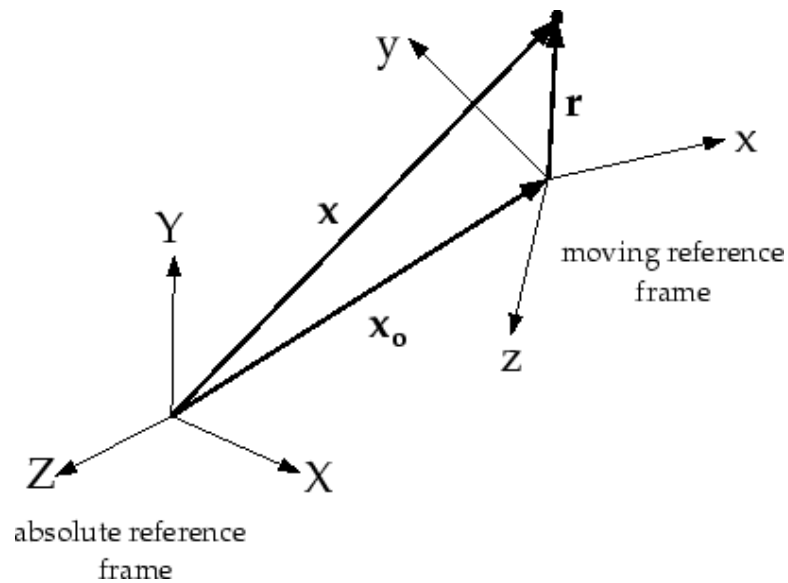


Figure 4.10. Coordinate system for relative velocity [41]

The left-hand side of the momentum equations appears as follows for an inertial reference frame:

$$\frac{\partial}{\partial t}(\rho \bar{u}) + \text{grad.}(\rho \bar{u} \bar{u}) \quad (4.2)$$

For a rotating reference frame, the left-hand side written in terms of absolute velocities becomes

$$\frac{\partial}{\partial t}(\rho\bar{u}) + grad.(\rho\bar{u}_r\bar{u}) + \rho(\bar{w}X\bar{u}) \quad (4.3)$$

In terms of relative velocities the left-hand side is given by

$$\frac{\partial}{\partial t}(\rho\bar{u}_r) + grad.(\rho\bar{u}_r\bar{u}_r) + \rho(2\bar{w}X\bar{u}_r + \bar{w}X\bar{w}X\bar{r}) + \rho\frac{\partial\bar{w}}{\partial t}X\bar{r} \quad (4.4)$$

For flows in rotating domains, the equation for conservation of mass, or continuity equation, can be written as follows for both the absolute and the relative velocity formulations:

$$\frac{\partial\rho}{\partial t} + grad.(\rho\bar{u}_r) = S_m \quad (4.5)$$

4.4.1.1. Multiple Reference Frame Model. The MRF model is the simplest of the three. It is a steady-state approximation in which individual cell zones move at different rotational/translational speeds. This approach is appropriate when the flow at the boundary between these zones is nearly uniform ("mixed out") [41].

While the multiple reference frame approach is clearly an approximation, it can provide a reasonable model of the time-averaged flow for many applications. For example, the MRF model can be used for a turbomachinery application in which rotor-stator

interaction is relatively weak. In mixing tanks, since the impeller-baffle interactions are relatively weak, large-scale transient effects are not present and the MRF model can be used. In general, any problems where transients due to rotor-stator interaction are small are candidates for the MRF model. Non-conformal mesh is allowed in the mixing boundary [41].

4.4.1.2. Mixing Plane Model. The mixing plane model in FLUENT provides an alternative to the multiple reference frame and sliding mesh models for simulating flow through domains with one or more regions in relative motion. The MRF model is applicable when the flow at the boundary between adjacent zones that move at different speeds is nearly uniform ("mixed out"). If the flow at this boundary is not uniform, the MRF model may not provide a physically meaningful solution. The sliding mesh model may be appropriate for such cases, but in many situations it is not practical to employ a sliding mesh. For example, in a multistage turbomachine, if the number of blades is different for each blade row, a large number of blade passages is required in order to maintain circumferential periodicity. Moreover, sliding mesh calculations are necessarily unsteady, and thus require significantly more computation to achieve a final, time-periodic solution. For situations where using the sliding mesh model is not feasible, the mixing plane model can be a cost-effective alternative [41].

In the mixing plane approach, each fluid zone is treated as a steady-state problem. Flow-field data from adjacent zones are passed as boundary conditions that are spatially averaged or "mixed" at the mixing plane interface. This mixing removes any unsteadiness that would arise due to circumferential variations in the passage-to-passage flow field (e.g., wakes, shock waves, separated flow), thus yielding a steady-state result. Despite the simplifications inherent in the mixing plane model, the resulting solutions can provide reasonable approximations of the time-averaged flow field. Non-conformal mesh may be used since an averaging method used for the calculations of the unknowns in the mixing plane area [41].

4.4.1.3. Sliding Mesh Model. When a time-accurate solution for rotor-stator interaction (rather than a time-averaged solution) is desired, the sliding mesh model should be used to compute the unsteady flow field. The sliding mesh model is the most accurate method for simulating flows in multiple moving reference frames, but also the most computationally demanding [41].

Most often, the unsteady solution that is sought in a sliding mesh simulation is time-periodic. That is, the unsteady solution repeats with a period related to the speeds of the moving domains. For flow situations where there is no interaction between stationary and moving parts (i.e., when there is only a rotor), the computational domain can be made stationary by using a rotating reference frame. When transient rotor-stator interaction is desired, sliding meshes must be used. If a steady state approximation of the interaction is desired, the multiple reference frame model or the mixing plane model may be used [41].

In the sliding mesh technique two or more cell zones are used. Each cell zone is bounded by at least one "interface zone" where it meets the opposing cell zone. The interface zones of adjacent cell zones are associated with one another to form a "grid interface". The two cell zones will move relative to each other along the grid interface. During the calculation, the cell zones slide (i.e., rotate or translate) relative to one another along the grid interface in discrete steps. A conformal mesh is a must in order to use this rotating reference frame. That means the cell nodes of the cells on both sides of the mixing plane should meet exactly in the mixing plane [41].

4.4.2. The Flow Model in Fluent

In order to solve the flow field there are so many options in Fluent. For a physical result the user should choose the appropriate ones that best fit the flow situation. Selecting the solver, material type, boundary conditions are some examples of such options.

In modeling the flow field in a GTM rotor wheel, segregated solver is a better choice considering the maximum flow speed, the steady state flow field and the Mach number. Maximum speed for GTMs is commonly not more than 60 m/s. This makes the flow subsonic and the Mach number below 0.3. Although the flowing fluid is a gas, compressibility effects are negligible and the variation of the gas density with pressure can safely be ignored in the model. So there is not much change between choosing an ideal gas model or incompressible ideal gas model. But to be on the safe side ideal gas model is taken in the numerical simulations.

Inlet and outlet boundary condition choices are also two important decisions to make. Inlet and outlet conditions are actually dependent on each other, so some combinations would not work together. Actually GTMs are volume flowmeters, they actually measure the average velocity and through that velocity the volume flow rate is calculated. It may make sense if the inlet is given as a uniform velocity distribution. But it should be noted that decreasing Reynolds number deflects the velocity profile from a uniform one, for laminar and transitional cases velocity profiles are clearly not uniform. At first glance the option of mass flow inlet may seem to be a best fit in this case, because mass flow rate may be considered as a fixed volume flow rate since the flow is steady state and subsonic. On the other hand this option generates a uniform flow profile at the inlet which is not desired for low Reynolds numbers. Pressure inlet is a superior choice among the other options that allow non-uniform velocity profiles at the inlet. For the outlet boundary condition the best fit for the mass flow rate inlet is the 0 gauge pressure outlet. The disadvantage of a pressure outlet boundary condition is that it forces a uniform pressure distribution at the outlet. As a result, pressure waves incident on the boundary would reflect in an un-physical manner, leading to local errors in compressible flows. In such cases Non-Reflecting Boundary Condition (NRBC), which is based on the Fourier transformation of solution variables at the non-reflecting boundary is a better choice. It permits waves to pass through the boundaries without spurious reflections but it is only available in coupled solver with structured mesh. Since the flow field in a turbine meter is subsonic and it is computationally costly to generate a structured mesh, pressure outlet boundary condition fits the best allowing some local errors at the outlet boundary.

For turbulent flow simulations, appropriate turbulence model should be chosen. If an inviscid flow is to be simulated then one should take care of the mesh. If the mesh is too fine, this may lead to non-converging flow results. On the contrary very fine mesh is needed near the wall zones in turbulent flows and also it should be noted that increasing the Reynolds number requires finer meshes. The best way to check the mesh independency of the model is through the y^+ values near the walls. It should be under 1 for enhanced wall treatments and around 1.3 for standard and non-equilibrium wall functions. At this point the choice of the turbulent model is also important. For turbulent flows with rotation two turbulence models are widely used, realizable k-epsilon and Reynolds Stress models. Both models use Reynolds-averaged Navier Stokes (RANS) equations. Realizable k-epsilon model is a two equation model. Although it produces non-physical turbulent viscosities in multiple reference frames, it shows superior behavior in single reference frames (SRF). On the other hand Reynolds Stress Model closes the Reynolds-averaged Navier-Stokes equations by solving 7 additional transport equations for the Reynolds stresses in 3D. It accounts for the effects of streamline curvature, swirl, rotation and rapid changes in strain rate in a more rigorous manner than two-equation models.

For the cases where y^+ is not in the desired range, a y^+ adaptation is used to have finer meshes around the walls. Since different operating conditions and flow rates are used it is not an easy task to create a model which has y^+ values in the above mentioned range for every operating condition and flow rate. That's why y^+ adaptation is a powerful tool in Fluent during the numerical simulation process.

If rotating reference frames are used, a high degree of rotation introduces a large radial pressure gradient which drives the flow in the axial and radial directions, thereby setting up a distribution of the rotation in the field. This coupling may lead to instabilities in the solution process. Since the single rotating reference frame is used in the numerical simulation, PRESTO! discretisation scheme is applied for pressure which is well-suited for the steep pressure gradients involved in rotating flows. Besides second order upwind scheme is used for the momentum equation, and under-relaxation factors for the velocities are reduced to 0.3.

5. Validation of Numerical Simulations

5.1. Numerical Simulation of a Turbine Meter in Air Flow

For the validation of the correct use of Fluent, an experiment conducted by Islam et.al. [42] is simulated numerically. The experiments were conducted in New Delhi on a turbine meter provided by Rockwin Flow Meter (India) Pvt.Ltd.

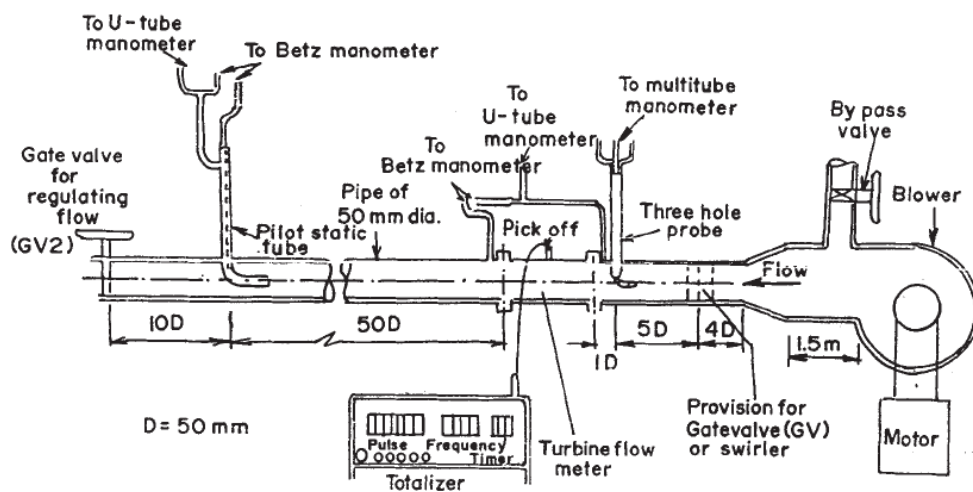


Figure 5.1. Schematic lay out of the experimental set-up for air flow [42]

The experiment actually investigates the effect of swirl and the effectiveness of a flow straightener in removing the swirl. The experimental set-up is shown in figure 5.1 The experiment is done in a flow rate range from 20 to 320 m^3/hr . The velocity measurement is done by the single point velocity measurement through a pre calibrated three hole probe. Since the actual aim of the experiment was to investigate the effects of swirl and straighteners, the set-up includes swirlers installed 6D upstream of the turbine meter, where D is the turbine meter diameter. A blower installed in the upstream of the turbine meter blows the atmospheric air through the setup. The flow entering the turbine meter ranges from 0° to 50° .

Actually most of the calibration tests for turbine meters are done in such set-ups. A blower in the upstream or a pump sucking air in the downstream of the turbine generate the pressure difference. In other words they are the flow rate sources. In the

downstream of the turbine meter a reference meter is installed and pulses from both turbine meters are compared for calibration purposes. Mostly atmospheric air which is the easiest medium to find is used for the calibration processes. It may be very expensive if air or another gas in different pressures are desired. For measurements of gases above or below atmospheric pressure, more complicated test setups should be used.

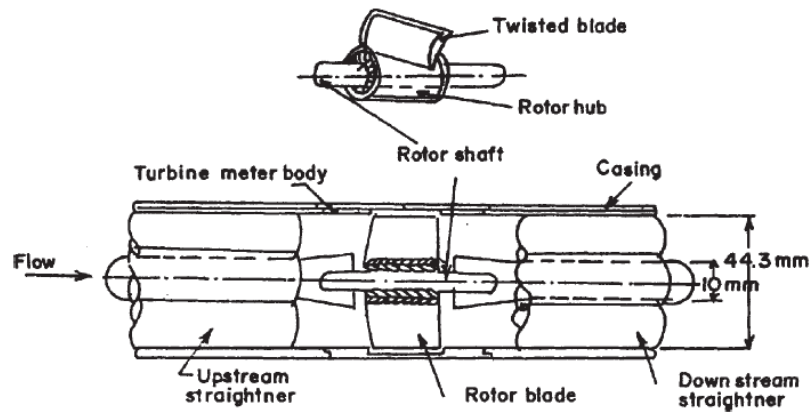


Figure 5.2. Turbine flow meter with tube type straightener [42]

The geometry of the turbine meter with tube type straighteners is given in figure 5.2. Table 5.1 shows the geometric details of the the turbine meter used in the experiments.

Table 5.1. Details of the turbine meter.

Rotor diameter	44.3 mm
Casing inner diameter at rotor	44.8 mm
No. of blades	6
Rotor shaft diameter	4 mm
Blade thickness	1.3 mm
Blade angle from axis of meter	30°
Span length of blade	15 mm

In the experiment the velocities and the rotation of the turbine meter are measured for each case both with straighteners and without them. 10 measurement points are marked which are shown in the K factor vs. Flowrate plot. Figure 5.3 shows the Flowrate vs. K factor plot for the undisturbed flow conditions.

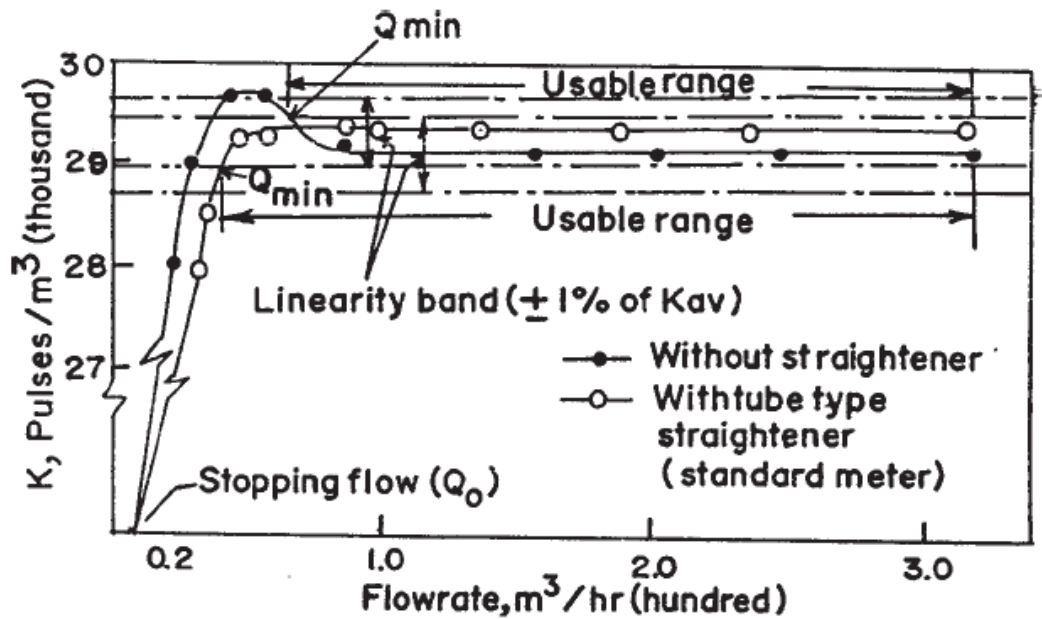


Figure 5.3. Characteristics of the turbine meter for undisturbed flow conditions [42]

Figure 5.3 shows clearly the characteristic properties of the tested turbine meter whereas Figure 5.4 shows the pressure drops across it. The stopping flow rate which is actually determined by the mechanical friction forces is shown to be around $20 \text{ m}^3/\text{hr}$. The difference between a turbine meter with and without straighteners is clear by looking at the hump that is due to the velocity profile effect in the turbine meter without a straightener. The average K factor is a value around $29000 \text{ pulses}/\text{m}^3$ for the case without the straighteners, where 6 pulses mean one revolution of the rotor for a 6 bladed rotor wheel. When the straighteners are introduced the average K factor shifts to a higher value. The usable range for a turbine meter determines the minimum flow rate of the turbine meter whereas the maximum flow rate is limited to the over-speeding limit of the rotor. The usable range is determined by the linearity error which is $\pm 1\%$ of the average K factor. As it is seen in the figure the straighteners expand the range of the turbine meter by eliminating the hump. The minimum flow rate for the case with the straighteners is around $40 \text{ m}^3/\text{hr}$.

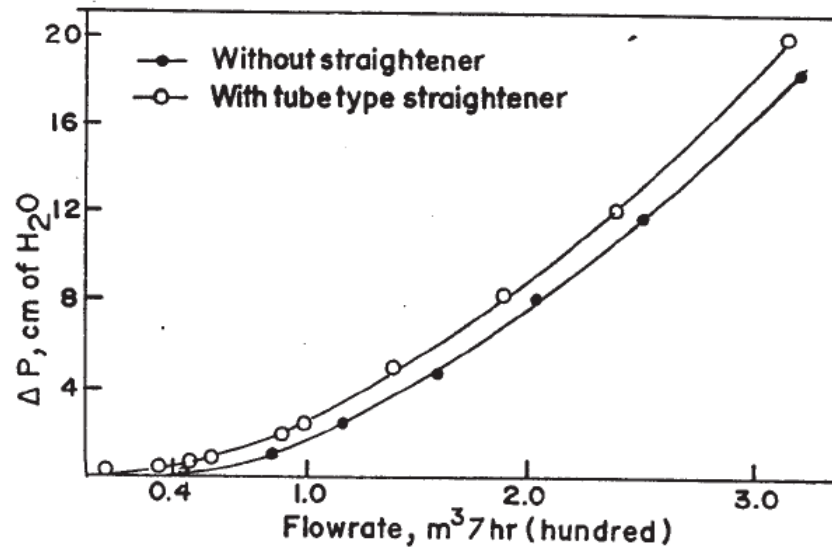


Figure 5.4. Pressure drop across turbine meter for undisturbed flow conditions. [42]

5.1.1. The Numerical Simulations

For the numerical simulations some simplifications and assumptions are done in the geometry. As it is seen in Figure 5.2 there are tolerance values between the flow conditioners and the rotor. There is also a tolerance difference between the diameters of the conditioners at the rotor side and the diameter of the rotor. The hub diameter is lower than the diameter of the conditioners at the rotor side. In the numerical model a volume around one blade is modeled. The tolerance values between the rotor and the conditioners are ignored. The tolerances between the hub and the conditioners in the radial direction are also ignored while the hub radius is taken as 7.15 mm. Hub radius can be found from the geometrical parameters given in Table 5.1. The axial distance between the conditioners and the rotor are assumed as 2.8 mm and 3.6 mm for the upstream and downstream respectively. The axial length of the volume is 26.4 mm including 2.8 mm, 3.6 mm tolerances and 20 mm axial rotor length. The hub axial length is taken as the axial length of the volume which converts the tolerances into a part of the hub. The tip clearance which is only above the rotor is expanded through the whole length of the volume. The numerical model used in the simulation is shown in Figure 5.5.

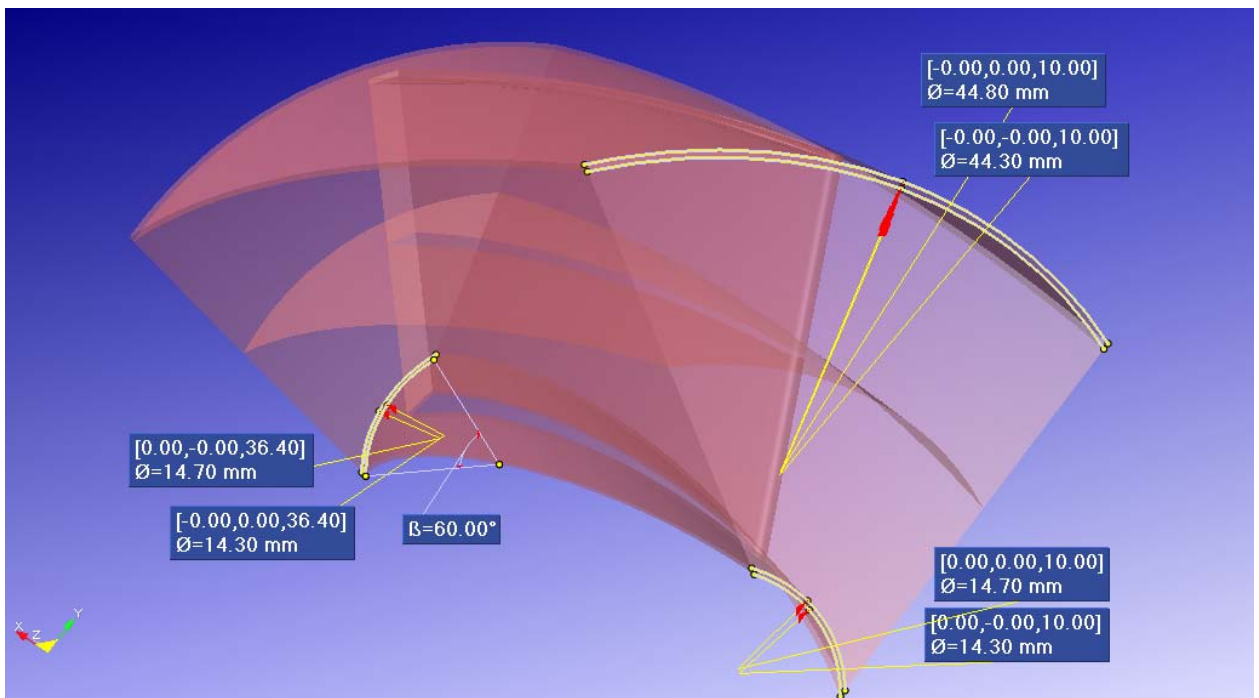


Figure 5.5. Volume around one blade used in the numerical simulation

For the numerical simulations a hybrid mesh, which is a mixture of structured and unstructured grid, is used since it is very difficult and time consuming to generate a structured mesh in 3D for a volume around a blade. In order to generate a suitable mesh for the solver, extra attention should be taken around the wall areas. For this purpose a boundary layer is used around the blades. Boundary layer is a structured mesh in Gambit that resembles the body fixed grids. The boundary layer starts with 0.01 mm and extends 20 rows with a growth rate of 1.05. It is desired to cover all the wall areas with a boundary layer, however in such a case boundary layer overlapping occurs and that causes meshing problems. In order to solve this problem the whole volume is divided into 5 volumes such that small volumes are generated around the walls. Two volumes cover the hub and the casing respectively for a finer mesh around these wall regions. Two volumes cover the blades making up the most of the overall volume. The fifth volume is the smallest volume to ensure a fine mesh above the blade tip wall in order to simulate the drag forces in the tip clearance region. The volumes are given in Figure 5.6 and the number of meshes used in those regions are shown in Table 5.2. Figure 5.7 shows the overall meshed volume. In meshing the volumes cooper scheme is used, that's why a certain order should be followed during the meshing process. Cooper scheme follows any direction but in the direction it follows

the faces should not be pre-meshed. For this reason meshing process started in the middle volumes, extending through the upper and lower volumes. Starting from the upper or lower volume could also be possible as long as one direction is followed.

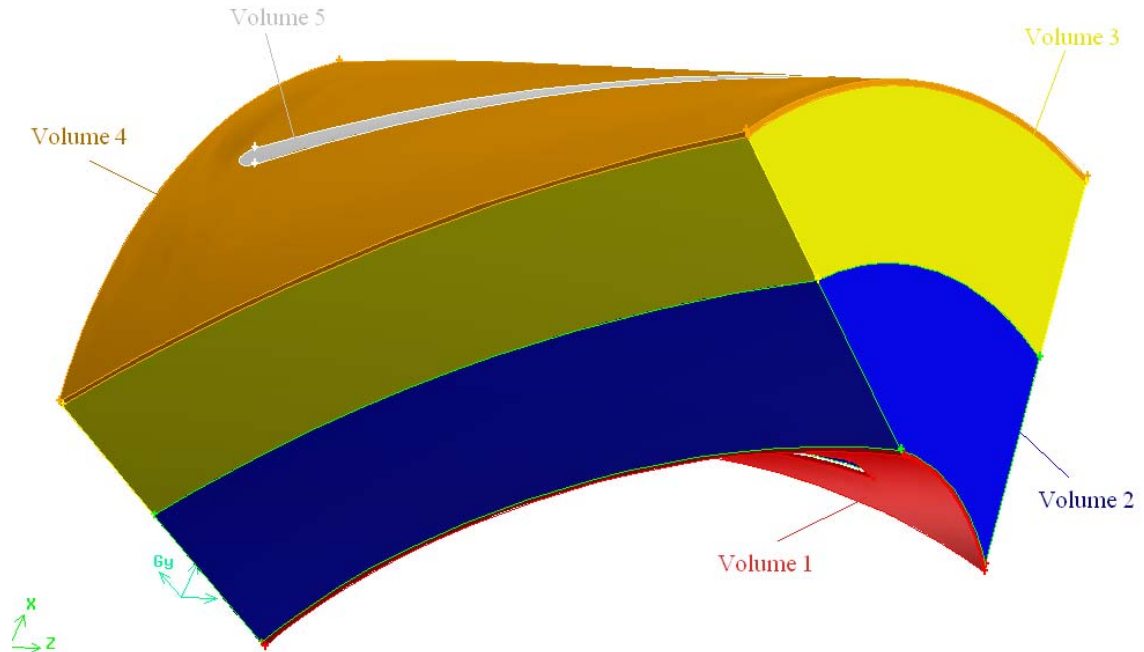


Figure 5.6. Volumes generated in the numerical model for meshing purposes

Table 5.2. Number of meshes used in the numerical model

Volumes	number of mesh elements used
Volume 1	160704
Volume 2	155520
Volume 3	98496
Volume 4	165888
Volume 5	10208

By looking at the characteristic curve of the turbine meter with straighteners, 10 measurement points are derived. According to these values, average velocity, angular speed and pipe Reynolds number are calculated. For the calculation of the Reynolds number density of air is taken as 1.1782 kg/m^3 which is the density for air as an ideal gas under 300 K temperature. The viscosity value of air is taken as $1.7894 \times 10^{-5} \text{ kg/m}\cdot\text{s}$. The hydraulic diameter at the rotor inlet is calculated to be $3.05 \times 10^{-2} \text{ m}$. The inlet area of the rotor is $1.4157 \times 10^{-3} \text{ m}^2$. It should be noted that all the measurement points show a turbulent flow where the Reynolds number values are above 4000. As the

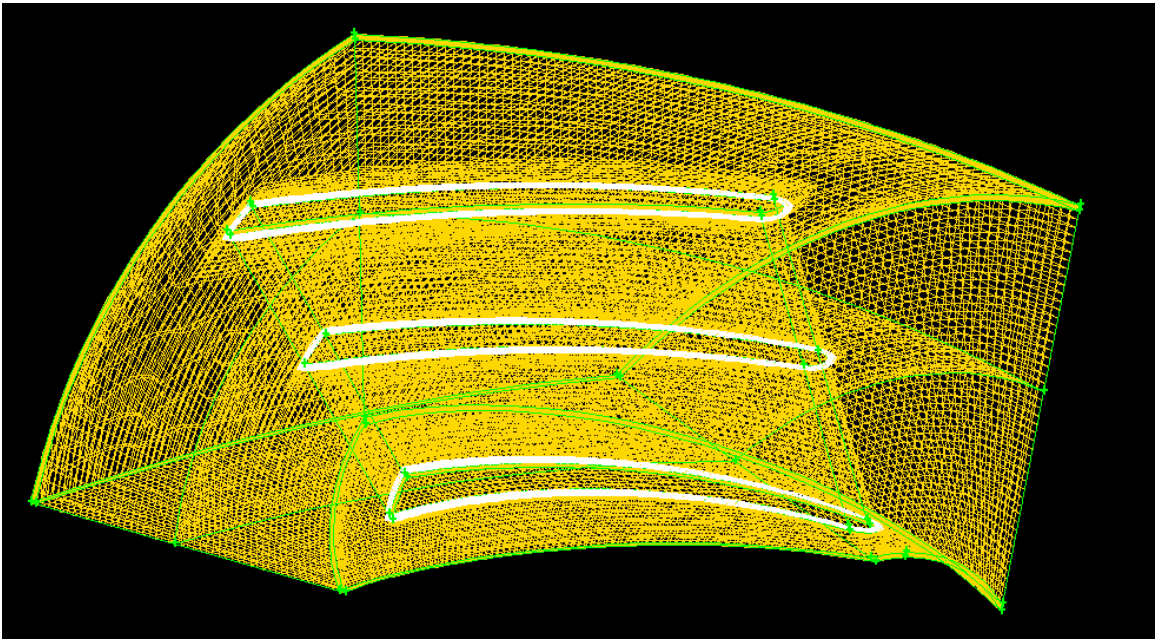


Figure 5.7. Volume meshed with 590816 hexahedral elements and the boundary layer

Reynolds number decreases the velocity profile may change into a non-uniform profile where also the mechanical friction forces can have significant effects. The table below (Table 5.3) shows the numerical values derived from the characteristic curve (Figure 5.3) of the turbine meter with the straighteners.

In numerical simulation pressure inlet boundary is used with pressure outlet. Pressure inlet values are chosen such that the volume flow rate covers the range that is shown in Figure 5.3. For this purpose an average density of 1.1782 kg/m^3 is assumed at the inlet for the temperature of 300°K . Because the flow is subsonic it is possible to get closer values of mass flow rates for the desired volume flow rate. Air is used as ideal gas at 300°K in the inlet since the experiment is assumed to be made at room temperature. Operating condition is taken as 1 atm. Outlet boundary condition is set to 0 atm gauge pressure. Rotational periodicity is used on the side walls of the volume. A single rotating reference frame model is used because only a volume around one blade is to be simulated. The casing wall is made stationary while the others are defined as rotating. The overall moment coefficient for the rotating walls around the rotation axis is monitored and the rotational speed is adjusted such that the moment coefficient is oscillating around zero. This kind of process was also used in a paddlewheel simulation which was done by Skaperdas et.al. [13]. Since the turbine rotor turns as a result of

Table 5.3. Turbine meter characteristic values derived from figure 5.3

Pressure drop	Flow rate	K factor	Angular Speed	V_{av} at inlet	Re at inlet
cm of H_2O	m^3/hr	pulse/ m^3	rpm	m/s	-
1	30	28000	2333	5.9	11821
1	40	28500	3167	7.8	15762
1.5	50	29200	4056	9.8	19702
1.5	60	29200	4867	11.8	23642
3	90	29400	7350	17.7	35463
3	100	29400	8167	19.6	39404
5	140	29400	11433	27.5	55165
8	190	29400	15517	37.3	74867
12	240	29400	19600	47.1	94569
20	320	29400	26133	62.8	126092

the flow at a constant speed, no forces should be present at the rotating parts. That's why all the moments generated on the rotating walls by the fluid should be zero.

Two different cases are simulated. In the first case all the mechanical friction forces, such as bearing friction and magnetic retarding forces, are ignored. In this case the rotational speed adjusted such that the moment coefficient converged to zero in a certain tolerance limit. In the second case the mechanical friction forces are also taken into account. For this purpose the stopping flow rate which is around $20 m^3/hr$ is used. For an average velocity of 3,9 m/s a pressure inlet of 8.7 Pa is simulated. So the stopping flow rate is assumed to be $19.825 m^3/hr$. The stopping moment under these conditions is found to be $1.19e-5 N.m$ which generates a moment coefficient of $1.95e-5$. For the simulation of the second case the rotational speed adjusted so that moment coefficient converged to $1.95e-5$ in certain tolerance limits.

Two different turbulence models are compared for a pressure inlet of 465 Pa. In both models y^+ values around the walls were under 1. The comparison is shown in Table 5.4. RSM model diverges if it is used from the very beginning of the simulation that's why realizable k- ϵ model was applied in the beginning, then switched to RSM.

Although both models have a certain level of error at 465 Pa pressure inlet case, realizable k- ϵ is closer to the actual result however it should not be forgotten that there are certain simplifications in the geometry such as hub, tip clearance expansions and also in the model. That's why it is hard to say one model is better than the other. On the other hand it is clear that realizable k- ϵ model is much faster than RSM such that realizable k- ϵ had an average iteration time of 41 seconds per iteration while that was around 57 seconds for RSM model. As long as the computational time and the closeness to the real results are concerned the rest of the simulations are done through realizable k-e model.

Table 5.4. Comparison of Realizable k- ϵ and Reynolds Stress models

		Realizable k-e	RSM
Pressure Inlet	Pa	465	465
V_{av}	m/s	24,42	22,89
Volume Flowrate	m^3/hr	124,46	116,66
Angular Speed	rpm	9979	9287
K factor	pulses/ m^3	28865	28659
C_m		1.1e-7	-1e-7

Table 5.5. Realizable k- ϵ turbulence model without stopping moment

Pressure Inlet	V_{av}	Volume Flow Rate	Angular Speed	K Factor
Pa	m/s	m^3/hr	rpm	pulses/ m^3
20	4,8	24,4	1874	27689
30	5,7	28,8	2220	27760
50	7,7	39,2	3075	28216
80	11,5	58,4	4641	28607
150	14,3	73,1	5843	28784
240	17,4	88,7	7100	28826
465	24,2	124,5	9979	28865

The numerical results of realizable k- ϵ model without stopping moment taken for 7 different pressure inlets are given in Table 5.5. The results of the model with the stopping moment is given in Table 5.6. As it can be seen from the tables, K-factor decreases when the stopping moment is introduced. Tables 5.3, 5.5, and 5.6 are

shown graphically in Figure 5.8 as a Flowrate vs K-factor plot. Although the results don't exactly match the actual ones, decreasing flowrate results in decreasing K-factor which is actually the case for the model. Decrease of the K-factor with the stopping moment is predicted also very well in the simulations. The difference with the actual results are probably caused by geometrical simplifications and unknown geometrical and experimental values. The velocity inlet profiles for the two different inlet pressures are also given in Figures 5.9 and 5.10.

Table 5.6. Realizable k- ϵ turbulence model with stopping moment

Pressure Inlet	V_{av}	Volume Flow Rate	Angular Speed	K Factor
Pa	m/s	m^3/hr	rpm	pulses/ m^3
20	4,6	23,6	1533	23418
30	5,7	29,2	1987	24485
50	7,7	39,0	2842	26209
80	11,4	58,1	4496	27858
150	14,1	71,9	5672	28415
240	17,2	87,7	6914	28394
465	24,1	122,8	9694	28413

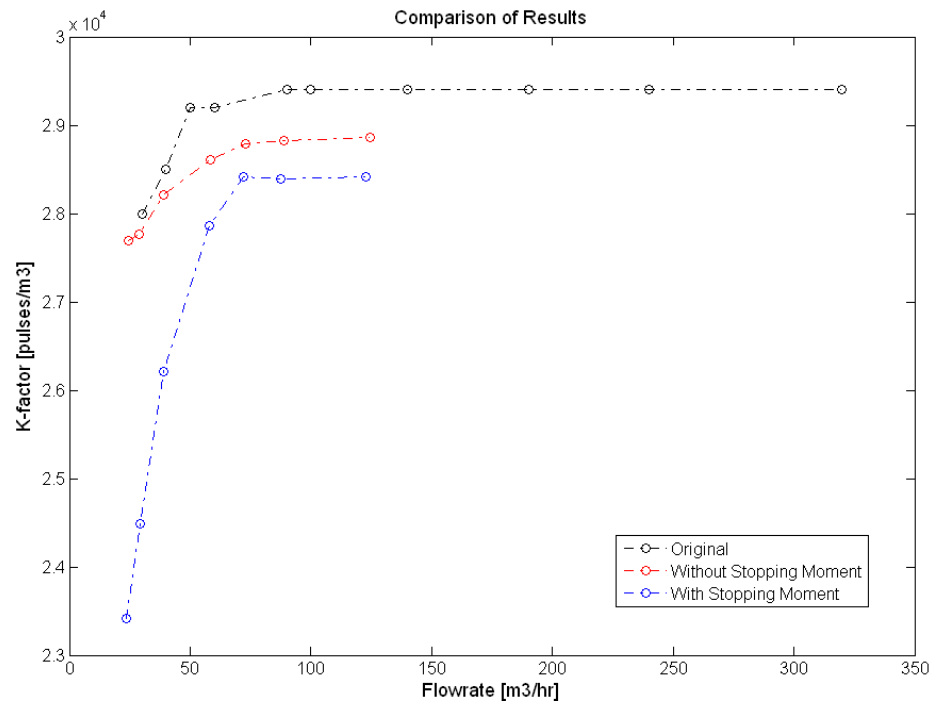


Figure 5.8. Flowrate vs. K-factor plot for realizable k- ϵ model

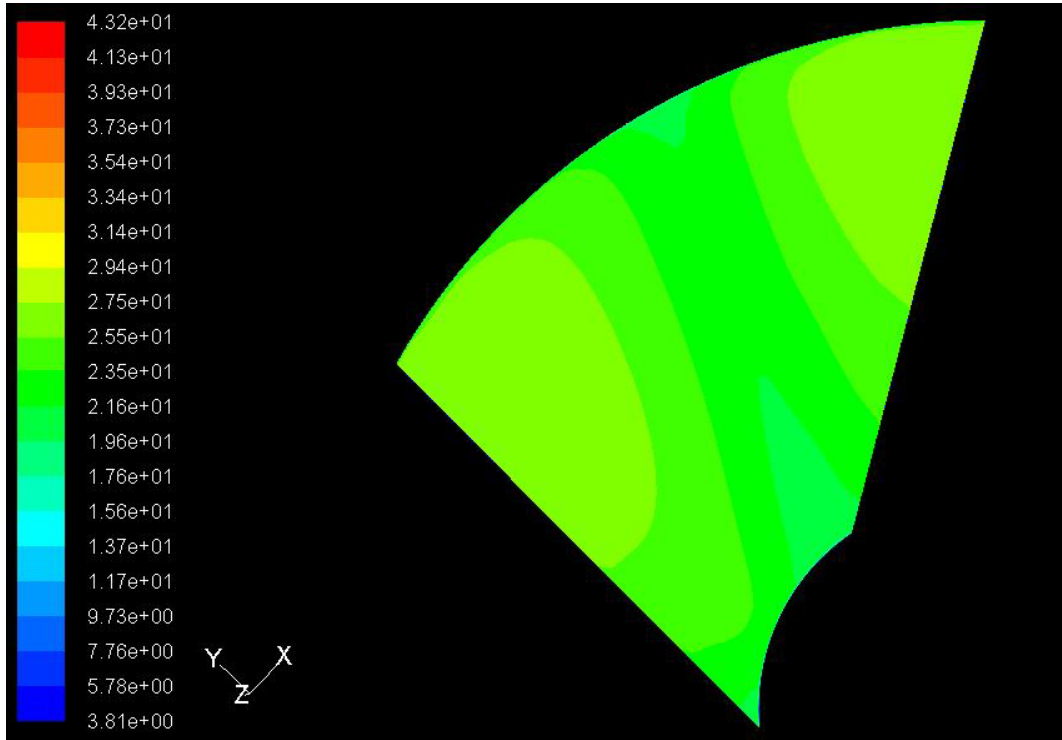


Figure 5.9. Velocity contours at the inlet for 465 Pa pressure inlet

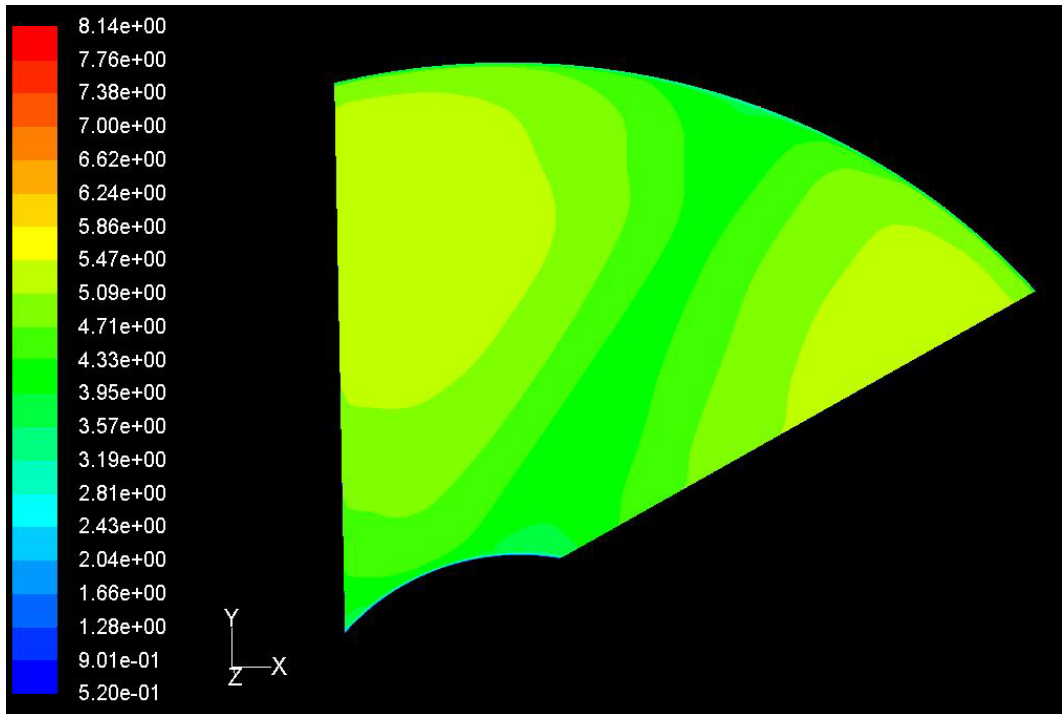


Figure 5.10. Velocity contours at the inlet for 20 Pa pressure inlet

6. The Computational Tool OptGTM3D

The computer code developed in Matlab software during this study is a controller of the CFD tools which are Gambit and Fluent for the sake of an improvement in a GTM rotor considering the blade geometry. Simple Graphical User Interfaces (GUIs) are designed in MATLAB software in order to facilitate the numerical solution from the beginning to the end, while it is designed for the fastest and the most physical convergence in Fluent. Different from Fluent it has the ability to select a laminar, transitional or a turbulent model for a specified flowrate considering the inlet Reynolds number. Moreover it acts like an external user defined function (udf) by adjusting the rotational speed for a zero moment coefficient of the rotating parts around the axis of rotation. However it should be mentioned that without batch options and journal file options in both softwares, the code wouldn't function.

Gambit is a very powerful pre-processor designed for Fluent while Fluent is a solver and post-processor. They are very commonly used and known to be user friendly CFD tools in the industry. However focusing on a GTM blade design process there are still lots of things to do using these very well known CFD tools. For this purpose the power of the user interfaces, graphics and the input-output functions of Matlab is combined with the solving and modeling properties of Gambit and Fluent. OptGTM3D user-interface computer code is brought about because of a need for a user defined function (udf) in solving the GTM models by Fluent. By learning the batch options in Fluent and Gambit, a more compact code is generated that has wider control over those CFD tools. Afterwards GUIs are added for a user-friendly environment.

The computer code is written for the 3D cases in Gambit and Fluent. For the code to work properly Gambit 2.1 and Fluent 6.1 or 6.2 should be installed on the Windows operating system with the pre-set environmental parameters which is a usual process for these CFD tools. The user-interface code consists of three main parts which are Pre-processor (Gambit), Solver (Fluent) and Post-Processor. As it can be understood from the names, it is better to follow the above mentioned order if there is

no pre-produced model available. The program is capable of producing and meshing a model for the user specified parameters and concentrates only on the rotor part of the GTM. It is also an easy task to make a model with the flow conditioners on both sides of the rotor but in most of the cases meshing becomes a problem but more important than that generating a volume for SRF becomes a problem. The code is not limited to one task at a time, instead it has the capability to solve a group of tasks for different parameters. If there was no limitation of the computer power and the time limit available for the computer to operate without any stop, it would be possible to get the characteristic curves of each GTM for different design parameters such as blade pitch angle and number of blades. Unfortunately there are time limitations of the Solver, such that sometimes it takes a whole day to complete one measurement point (which may be considered as one flowrate) for one GTM model.

The task monitor is common for three parts of OptGTM3D. It keeps the command history and the results of the commands in a historical order. In the time intervals when Gambit and Fluent are working it can not display anything, so any information given by the task monitor is done after a task is finished which is generally by reading the transcript files.

6.1. Pre-Processor (Gambit)

This part of the Matlab code is designed to model a volume around one blade for the user specified parameters. The working principle of the Pre-processor part is based on the batch modes running with journal files and the programming capabilities in Gambit. First a journal file is written by Matlab for the specified geometry parameters and run by a dos command in Matlab. Sometimes the specified parameters may not be correctly supplied, in such cases Gambit keeps executing the journal file till the end, allowing errors. A successful execution or an error during the execution is monitored through reading the transcript files which are present at any Gambit execution. A successful execution would mean a transcript file without error. In order to distinguish the files generated by OptGTM3D special variables are placed in the final .dbs file such as hub and casing diameters and number of blades. Those parameters also help

for gathering the necessary information for the meshing, solving and post-processing. Again those values are read through transcript files.

When a geometrical model is generated, it is added in the pop-up menus both in the Model Generator as an output and the Mesh Generator as an input file. The files appear in the pop-up menus with their file names. The file name specifies the root name that will be given to the generated file. The number of blades and the blade pitch angle are also other parameters included in the full name. It is possible to model a rotor with static parts. Those are generally models when some parts of the conditioners are included in the model. In these cases those parts of the hub become hub-inlet and hub-outlet as they are specified as stationary during the solution process. For such cases the check boxes should be used with the axial length specification. Leading edge and trailing edge tolerances are the axial distances between the edges and the ends of the whole volume. If the tolerances are very small it means that inlet or outlet boundary conditions are very close to the walls which mostly results in un-physical solutions. The number of blades, blade pitch angle and tip clearance values may be specified in the interface. It is also possible to give a curved or flat shape to the edges of the blade through the interface. Another important possibility of the Model Generator is to model both flat and twisted blades. For the twisted blade types, the default ideally twisted blade could be chosen with the default function or the user may enter a function between the angle and the radius. When the model is generated it appears under the Generated Models' pop-up while it also appears in the Mesh Generator's pop-up as an input.

Mesh Generator is a very critical part of the solving process. Fine enough meshes should be used for time being and better results. For this purpose special attention should be paid for the near wall regions. For this purpose the mesh is generated as 5 volumes as it is shown in Figure 6.1. Two of them cover the hub and casing regions to ensure fine meshes around them and another one covers the region above the blade tip area for predicting the tip leakage flow. The rest of the volumes are the biggest ones around the blade. They actually cover the blades and are not very fine meshed away from the blades but near the blades a very fine boundary layer is used which is 20 rows

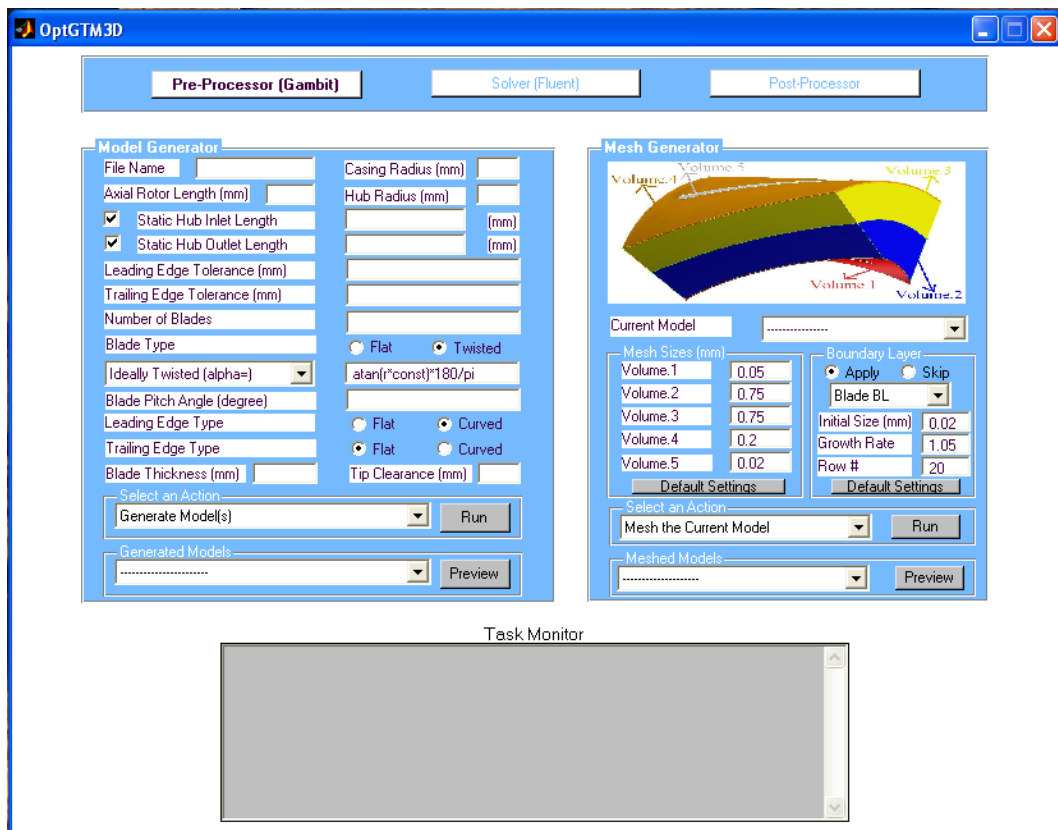


Figure 6.1. Pre-processor part of OptGTM3D

by default to ensure y^+ values of the blade sides in a certain range.

6.2. Solver (Fluent)

Solver part of the code is a controller of the Fluent. Previously meshed models appear in the pop-up window of the Solver. It is possible to choose solving one specific model or all the models using the action pop-up menu. Certain parameters like operating temperature and operating pressure should be entered. By default they are 300 K and 1 atm respectively. The maximum iteration shows the upper limit to stop the process. Moment coefficient tolerance is the limit for a moment coefficient convergence. Since rotational speed is updated for a zero moment coefficient which is never zero instead oscillating around zero, a tolerance of $1e-6$ is set by default for the process to stop. Under this value the rotational speeds generally change by very small values. There are two gas options to use in the simulation which are air and methane. It is also possible to add more materials from the Fluent Database. When the code needs some

material information like density, Fluent Database values are used. This is again the same case as it was in using Gambit. Those values are read into Matlab through the transcript files which are as an option opened in Fluent by using journal files. All the commands are given to Fluent by journal files and the results are monitored through the transcript files.

Inlet boundary is an important subject to take care of since some inlet boundary conditions may be misleading. As it was already mentioned in chapter 5, there is only one option which is the pressure inlet that allows non-uniform velocity profiles. Although it has a disadvantage of forcing uniform pressure at the outlet, it proves to be the best among the others. For large Reynolds numbers the velocity profile becomes uniform and in such cases velocity inlet may also be used. In the code for the inlet boundary a desired volume flow rate by the pressure inlet is set by default. Although the resultant volume flowrate of the solution does not match the desired one, it gets a closer value if the flowrate is concerned. The code first gives a velocity inlet which is calculated by using the inlet area and then reads the pressure difference by initialization in Fluent and that value is later given as a pressure inlet throughout the simulation. For a velocity inlet choice of boundary condition, both a velocity value directly or a flow rate value can be used. In this case instead of the ideal gas model, incompressible ideal gas model will be switched on in Fluent.

A maximum flow rate may be found by supplying a maximum rotor speed. In this case a reverse operation is used such that for a certain rotor speed the inlet conditions are adjusted to find the corresponding value. Again a zero moment coefficient is desired. If a more complete model is desired, there is also a stopping moment option with the help of which mechanical retarding forces can be taken into account in the simulations. A stopping flowrate, velocity or a direct moment value may be entered after which the moment coefficient converges to the desired moment value. If no value is entered as a stopping value then moment coefficient converges to 0. Moment coefficient iteration interval is set to 20 by default, meaning that every 20 iterations the code checks for a moment convergence. In such a case the code reads the coefficient values for the last 20 iterations, in order to decide on a convergence the difference between the average of

the first ten iterations and the last ten iterations should be in a tolerance range of %1 of the average of the last ten iteration. When this condition is supplied the rotational speed may be updated through a linear clever calculation. New value for the rotational speed is predicted by using the last two rotational speed and moment coefficient values assuming a linear relation. This ensures always updating for better values for the zero convergence of the moment coefficient. In the beginning of the iteration first value is always taken for zero rotational speed and the next one is taken for 100 rpm in the direction the moment is generated. The next value is calculated proportionally.

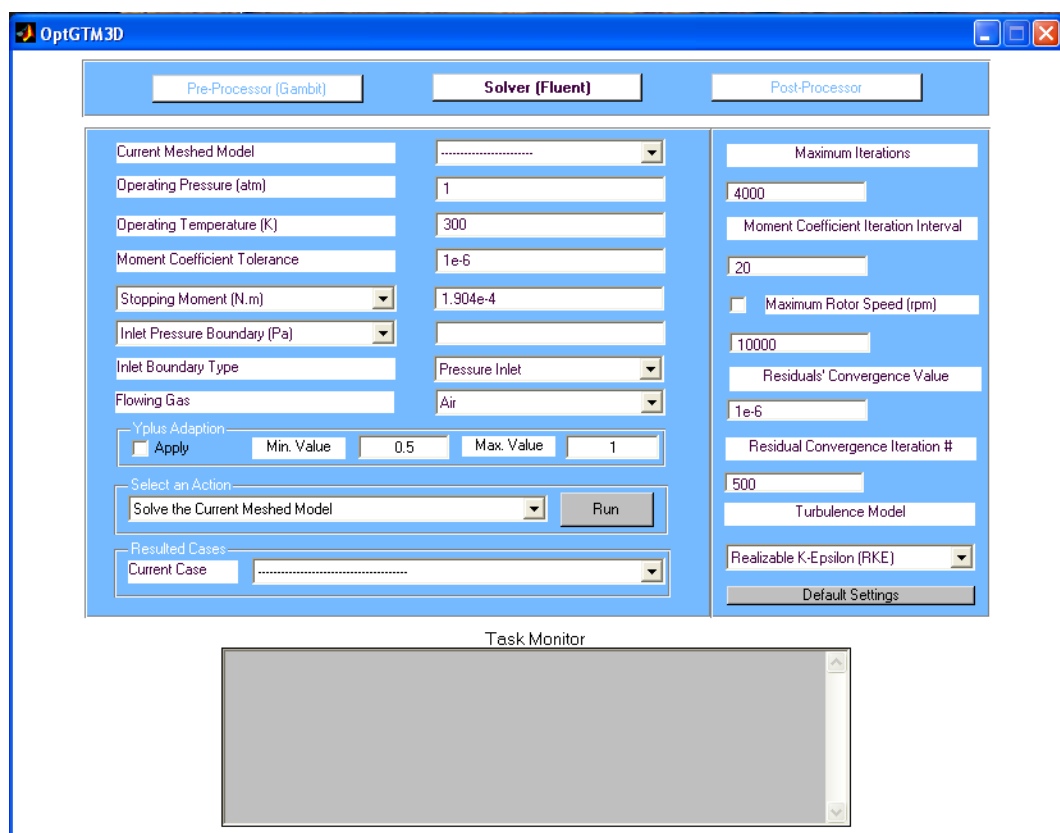


Figure 6.2. Solver part of OptGTM3D

There is also a y^+ adaption panel where the user may want to ensure y^+ values below a specified range. By default it is set off since it is always better to have a fine enough mesh without adaption but as the flow rate increases the y^+ values also increase. For a big range of flowrate values, it may be better to save time with such an approach. In such an option the code first arranges the y^+ values by adaption at the walls then the usual process begins. Adaption is also done by monitoring the transcript file. For the walls which are under the user specified values the adaption applies.

6.3. Post-Processor

After the results are generated, all the results are registered in the database which is a listbox object in Matlab. In the Post-processing part only one blade model can be processed at a time. All the case data which are calculated for different flowrates make up the database for this model. The results may be plotted in the panel called Database Graphics. The X-axis and Y-axis may be chosen by the drop-down menu above the axes. If there are enough cases available for a model then the characteristic curve may be generated through which minimum, maximum flowrates and the linearity band can be calculated. It is also possible to display contours of a property such as velocity or pressure at the boundaries through the post-processing ability of Fluent. In periodic boundaries Fluent has the option to display the results for the whole rotor. By clicking the check box below, this property can also be used. The database import from and export into a text file options are also available.

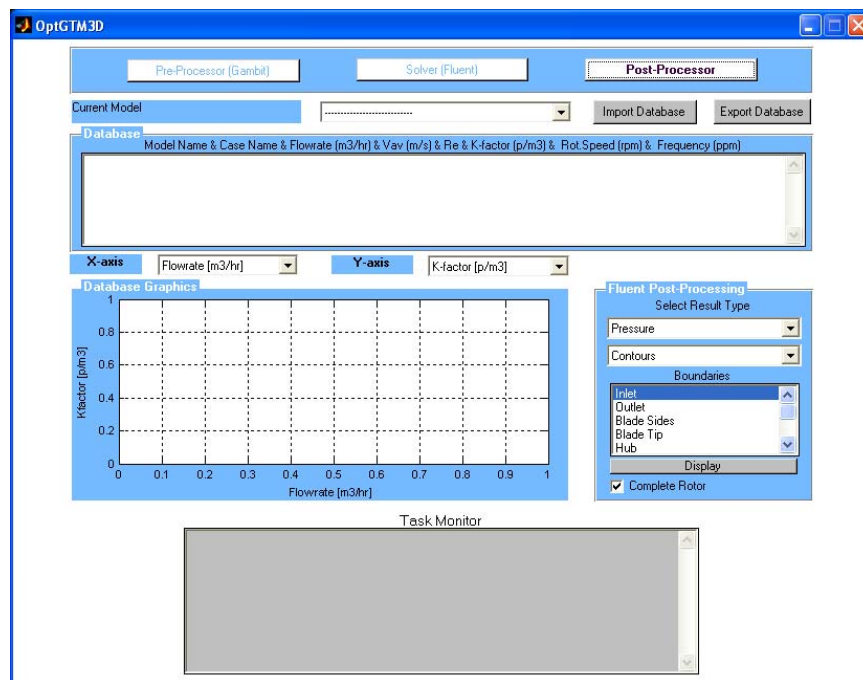


Figure 6.3. Post-processor part of OptGTM3D

7. Design of GTM

Design parameters used in this study are number of blades, blade pitch angle, tip clearance and the trailing edge shape. Those parameters are investigated independent of each other because of time being. First of all the blade angles are chosen for $30^\circ, 35^\circ, 40^\circ$ and 45° . The results are compared according to the maximum allowable flow range. After the best geometry is chosen according to the blade pitch angle, blade number is changed for the chosen blade pitch angle. Three different blade numbers are investigated as 12, 16 and 20. Again the results are taken to find out the best geometry for the maximum flow range. The same procedure applies for a trailing edge shape. Two shapes are investigated. A flat trailing edge as it is in the supplied solid model and a curved edge created by a circle are compared. After choosing the trailing edge shape the tip clearance is examined for three different distances such as 0.5 mm, 1.5 mm and 2.5 mm. The whole design process is based on a maximum flow range investigation such that the turbine meter has the maximum usable flow range among the others. This is actually done for a $\pm 0.5\%$ linearity condition. For different linearity conditions the results may be different.

For the calculation of the flow range minimum and maximum flow rates are found under some assumptions. The K-factor taken from the highest Reynolds' number is taken as the average K-factor. Assuming a maximum rotational speed limit of 10000 rpm for the rotor maximum flow rate is found. A 4th order polynomial approximation is applied on the region where the K-factor deviates from linearity. Exactly saying the K-factors taken from the cases where inlet boundary pressures of 10, 20, 60, 100, 150 Pa are applied made up the base points for the polynomial approximation. For a linearity of $\pm 0.5\%$ a K-factor range is generated with minimum and maximum values for the K-factor. The peak point of the hump is calculated through the approximated 4th order polynomial. According to the K-factor range and the peak point of the polynomial function, the minimum flowrate is found as an intersection of the polynomial and the minimum or maximum flow rate values. As a result the geometry with the maximum flow range is chosen to be the best one.

In meshing the created models the procedure described in the validation chapter is applied with an improvement. Again the model is divided into 5 different models for fine enough meshes around the wall regions. Different than the procedure described above two additional boundary layers are used in the model. First one is created around the blade region in the first volume while the second one is created in the fourth volume. The first boundary layer has the same properties as for the other boundary layers around the blade. The second boundary layer has an initial size of 0.015 mm with a growth rate of 1.05 up to 10 rows. Another improvement was using coarse meshes in the axial direction but fine meshes in the radial direction. Beside the boundary layers, this is accomplished by using coarse face meshes at the hub which is composed of hub-inlet, hub-rotor and hub-outlet parts. For all the models the above mentioned procedure is applied without changing any mesh size or boundary size value. The meshes generated were around 200,000 cells originally which was increased to 250,000 elements by y-plus adaption method in Fluent for high flow rates. When 590,000 cells used in the validation process is considered, the improved meshing method greatly reduces the time spent in the simulation process.

In the numerical simulations again the procedure described in the validation chapter is followed. In order to simulate the flow in a more realistic way a constant moment is taken as the mechanical retarding moment caused by the bearing friction and magnetic forces. Since there is no reference for such a retarding moment an assumption is made considering the stopping moment in the model used for validation. The stopping moment in that case for one blade was 1.194×10^{-5} N.m. The same moment is taken for one blade of a 16 bladed rotor since more retarding torque should be generated if the sizes are compared. Keeping the overall mechanical retarding moment which is 19.104×10^{-5} N.m constant, for 12 bladed rotors 1.592×10^{-5} N.m and for 20 bladed rotors 0.9552×10^{-5} N.m are taken for one blade. Corresponding moment coefficients are used with a moment coefficient tolerance of 1×10^{-6} . The rotational speed adjusted such that the moment coefficient is in the mentioned range. A moment convergence graph for a 5 Pa pressure inlet boundary in a 12-bladed rotor is shown in Figure 7.1. The bigger the jump is, the greater the change is in the rotational speed. The direction of the jump shows the increase or decrease of the next moment coefficient. If the moment

coefficient is greater than the desired value, the rotational speed should be increased. If it is lower than the desired value then it should be decreased. The resulting moment coefficient never converges to a fixed value but rather oscillates around a value. Those oscillations become smaller as the residuals decrease.

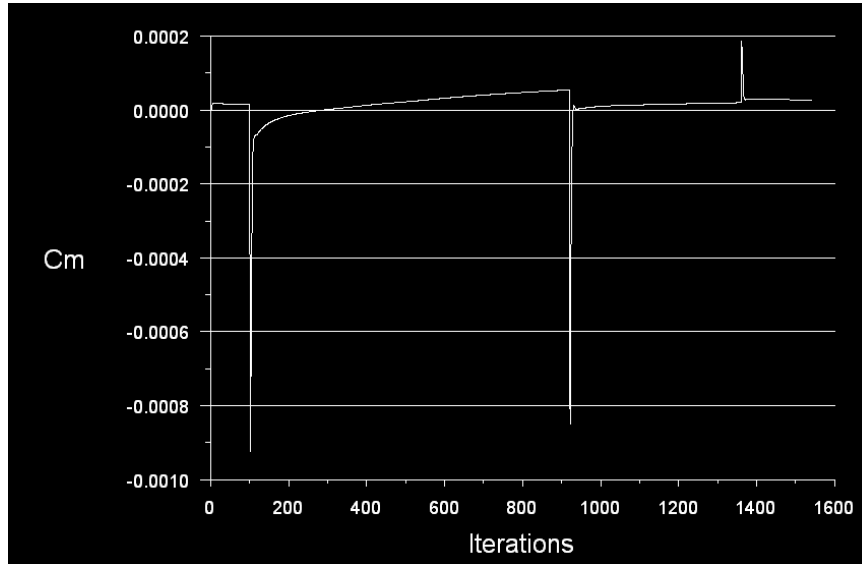


Figure 7.1. A part of the moment convergence plot for a 12 bladed rotor

All the results are taken for the residual values under $1e-5$. It should be noted that moment coefficient converges faster than the residuals, that's why such a residual tolerance is enough. For all the wall regions y -plus values are under 1. For high flow rates mostly for 100, 150, 200 and 250 Pa inlet pressure boundary conditions a y -plus adaption is applied for the desired y -plus values. For all the cases air is taken as the flowing fluid and 1 atmosphere is taken as the operating pressure. Operating temperature is set to 300 K for which the air has the density of 1.1782 kg/m^3 and a viscosity of $1.7894e-5 \text{ kg/m.s}$. The blade thickness is taken as 2.5 mm. Considering a 74 mm casing and 55.5 mm hub radius the inlet area is calculated as 0.0075265 m^2 and the hydraulic radius is taken as 0.037 m. The Reynolds numbers given in the tables are calculated according to the inlet parameters. Since all the Reynolds' numbers were above 4000 no transitional or laminar flow models were applied in the numerical simulations.

Table 7.1. Numerical results taken for 30° blade pitch angle with 16-bladed rotor

Pressure Inlet	V_{av}	Flowrate	Angular Speed	K-Factor	Reynolds number
Pa	m/s	m^3/hr	rpm	pulses/ m^3	
5	2,23	60,3	196,0	3119	5424
10	3,76	101,8	350,0	3300	9154
20	4,78	129,5	456,5	3384	11643
60	8,51	230,6	824,3	3431	20736
100	11,10	300,7	1072,4	3423	27039
150	13,69	370,9	1322,1	3422	33347
200	15,87	429,9	1532,7	3423	38655
250	17,79	482	1718,0	3422	43338

Table 7.2. Numerical results taken for 35° blade pitch angle with 16-bladed rotor

Pressure Inlet	V_{av}	Flowrate	Angular Speed	K-Factor	Reynolds number
Pa	m/s	m^3/hr	rpm	pulses/ m^3	
5	2,18	59,0	235,0	3823	5307
10	3,32	90,0	375,0	4001	8089
20	4,71	127,6	543,0	4086	11471
60	8,37	226,9	972	4111,1	20397
100	10,93	296,1	1264,2	4098,3	26626
150	13,47	365,0	1556	4093	32814
200	15,63	423,6	1803	4086,4	38084
250	17,45	472,8	2013	4087,2	42512

Table 7.3. Numerical results taken for 40° blade pitch angle with 16-bladed rotor

Pressure Inlet	V_{av}	Flowrate	Angular Speed	K-Factor	Reynolds number
Pa	m/s	m^3/hr	rpm	pulses/ m^3	
5	2,06	55,8	266	4577,7	5016
10	3,51	95,2	472	4758,5	8562
20	4,59	124,5	630	4858,2	11193
60	8,23	222,9	1135	4887,2	20046
100	10,75	291,3	1480	4875,2	26195
150	12,60	341,4	1733	4873,2	30696
200	15,85	429,5	2181	4875,3	38614
250	17,15	464,6	2359	4873,8	41769

Table 7.4. Numerical results taken for 45° blade pitch angle with 16-bladed rotor

Pressure Inlet	V_{av}	Flowrate	Angular Speed	K-Factor	Reynolds number
Pa	m/s	m^3/hr	rpm	pulses/ m^3	
5	2,01	54,4	303	5342,2	4896
10	3,46	93,7	537	5499,7	8428
20	4,44	120,2	707	5644,6	10811
60	7,89	213,7	1264	5679,0	19212
100	10,46	283,5	1671	5657,6	25494
150	13,01	352,6	2081	5664,5	31703
200	15,72	425,9	2514	5666,2	38297
250	17,52	474,7	2801	5664,4	42682

Table 7.5. Polynomial approximations for different blade pitch angles with the 16-bladed rotor

30°	$-2E-07x^4 + 0,0003x^3 - 0,1101x^2 + 19,02x + 2242,2$
35°	$-2E-07x^4 + 0,0002x^3 - 0,0707x^2 + 12,191x + 3359,8$
40°	$-4E-07x^4 + 0,0004x^3 - 0,1434x^2 + 22,993x + 3569,9$
45°	$-7E-07x^4 + 0,0007x^3 - 0,2472x^2 + 38,406x + 3568,1$

Table 7.6. Comparison of results taken for different blade pitch angles with the

16-bladed rotor				
	30°	35°	40°	45°
Average K-factor (p/hr)	3421,7	4087,2	4873,8	5664,4
K-factor max. (p/hr)	3438,8	4107,6	4898,2	5692,7
K-factor min. (p/hr)	3404,6	4066,7	4849,5	5636,1
Q min (m^3/hr)	140,5	240,7	195,3	197,3
Q max (m^3/hr)	2805,6	2348,8	1969,7	1694,8
Turndown ratio	20	9,8	10,1	8,6
Usable range (m^3/hr)	2665,1	2108,1	1774,4	1497,5

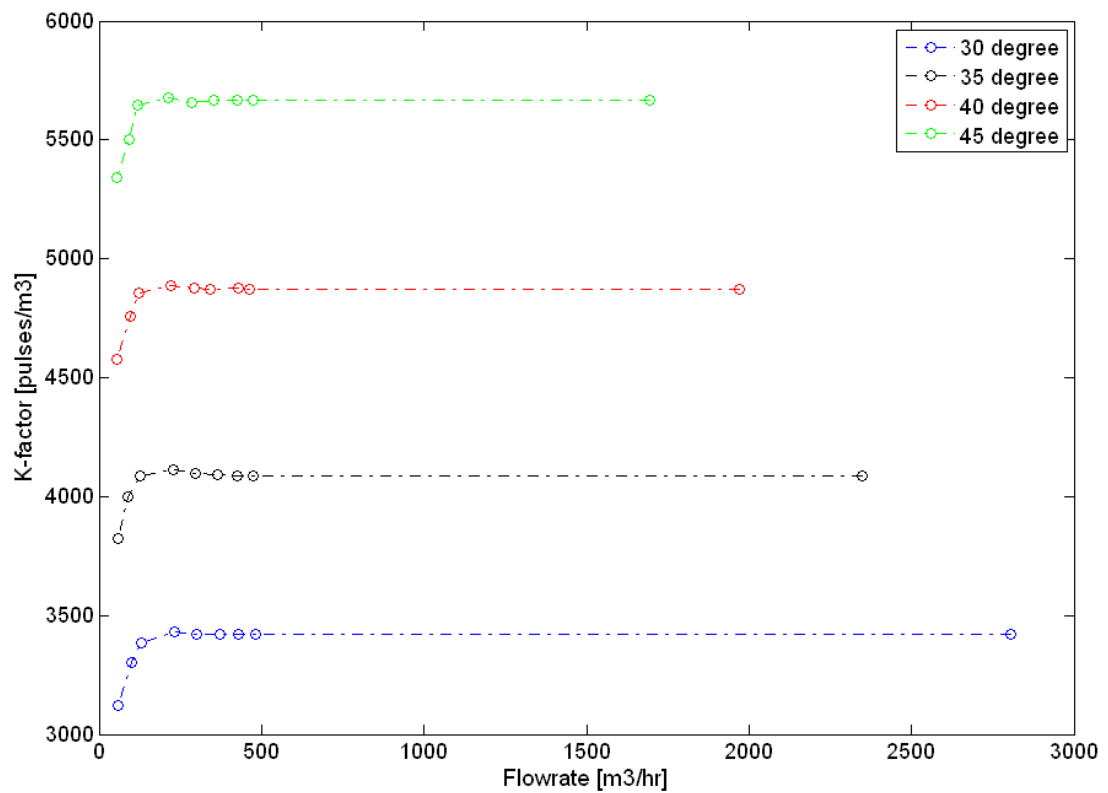


Figure 7.2. The comparison of the flowrate vs. K-factor plots for different blade pitch angles for the 16 bladed rotor

Table 7.7. Numerical results taken for 12 blades for the blade pitch angle of 30°

Pressure Inlet	V_{av}	Flowrate	Angular Speed	K-Factor	Reynolds number
Pa	m/s	m^3/hr	rpm	pulses/ m^3	
5	2,29	62,0	193	2241,4	5574
10	3,39	91,8	304	2385,1	8250
20	4,88	132,4	450	2449,9	11900
60	8,74	236,9	818	2486,2	21299
100	11,42	309,4	1066	2481,7	27815
150	14,06	380,9	1312	2480,2	34249
200	16,29	441,4	1521	2480,0	39691
250	18,27	495,0	1705	2479,8	42507

Table 7.8. Numerical results taken for 20 blades for the blade pitch angle of 30°

Pressure Inlet	V_{av}	Flowrate	Angular Speed	K-Factor	Reynolds number
Pa	m/s	m^3/hr	rpm	pulses/ m^3	
5	2,12	57,4	193	4032,7	5164
10	3,15	85,3	305	4290,1	7671
20	4,62	125,2	458	4388,8	11260
60	8,23	223,1	826	4443,2	20055
100	10,76	291,6	1076	4428,4	26216
150	13,28	359,8	1326	4420,7	32351
200	15,41	417,4	1537	4419,6	37530
250	17,28	468,1	1723	4417,7	42086

Table 7.9. Polynomial approximations for different blade numbers for the blade pitch angle of 30°

12 blades	$-6E-08x^4 + 8E-05x^3 - 0,0351x^2 + 6,8716x + 1994,6$
16 blades	$-2E-07x^4 + 0,0003x^3 - 0,1101x^2 + 19,02x + 2242,2$
20 blades	$-8E-08x^4 + 0,0001x^3 - 0,0479x^2 + 9,4973x + 3769,2$

Table 7.10. Comparison of results taken for different blade numbers for the blade pitch angle of 30°

	12 blades	16 blades	20 blades
Average K-factor (p/hr)	2479,8	3421,7	4417,7
K-factor max. (p/hr)	2492,2	3438,8	4439,8
K-factor min. (p/hr)	2467,4	3404,6	4395,6
Q min (m^3/hr)	152,4	140,5	242,5
Q max (m^3/hr)	2903,4	2805,6	2716,3
Turndown ratio	19,1	20	11,2
Usable range (m^3/hr)	2751,0	2665,1	2473,8

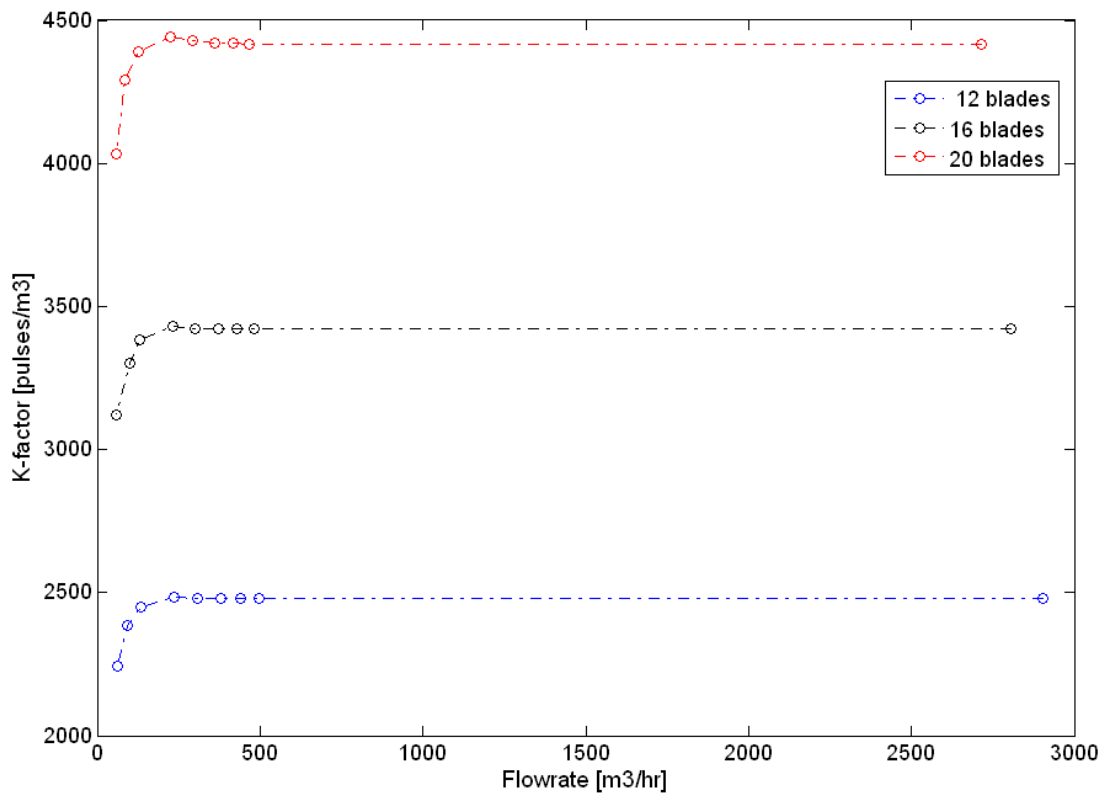


Figure 7.3. The comparison of the flowrate vs. K-factor plots for different blade numbers for the blade pitch angle of 30°

The results taken from four different blade pitch angles for a 16 bladed rotor are shown in the Tables 7.1,7.2,7.3, and 7.4. The flow range properties of the four different turbine meters are given in Table 7.6 and shown graphically in Figure 7.1.

As it is seen in Table 7.6 and Figure 7.2, the model with the blade pitch angle of 30° proves to have the largest usable flow range. For the next step different blade numbers are taken for the blade pitch angle of 30° . The numerical results for 12 and 20 blades are given in Tables 7.7 and 7.8. The comparison between different blade numbers are shown graphically in Figure 7.3. the velocity profiles for two different flowrates are shown in Figures 7.4 and 7.5.

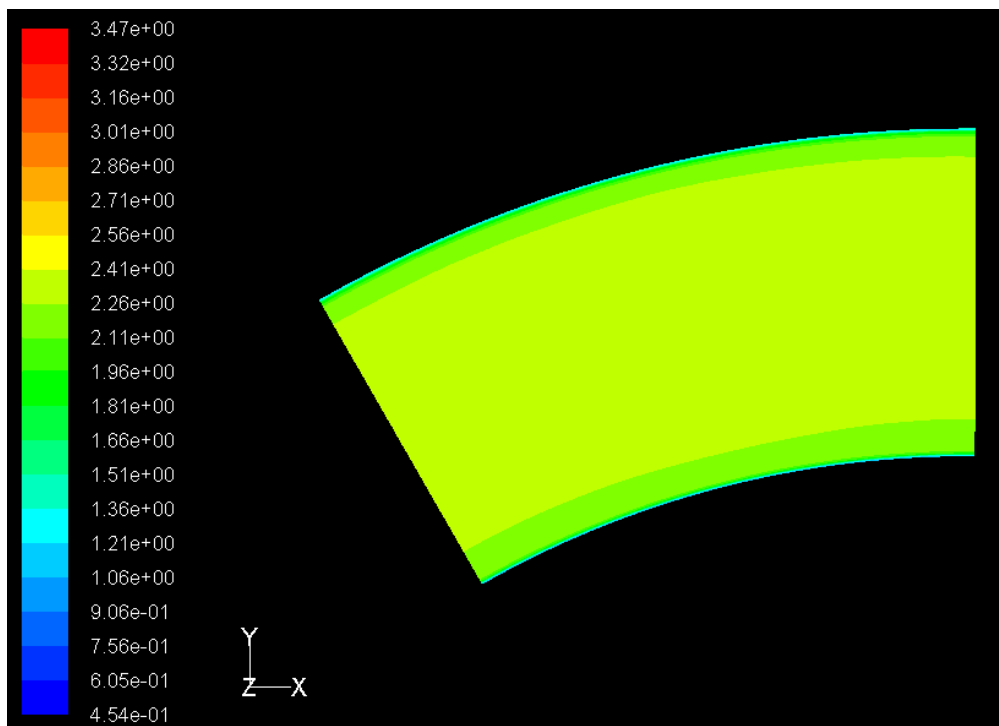


Figure 7.4. The velocity profile for a 12-bladed rotor for 5 Pa inlet pressure boundary condition

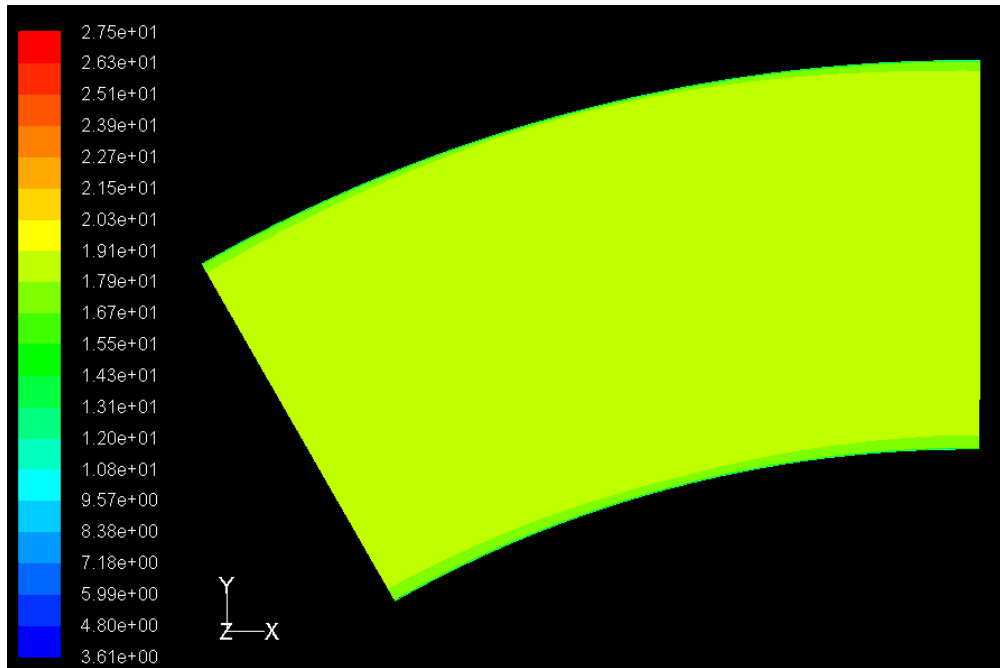


Figure 7.5. The velocity profile for a 12-bladed rotor for 250 Pa inlet pressure boundary condition

Table 7.11. Numerical results taken for the curved trailing edge with 30° blade pitch angle for the 12-bladed rotor

Pressure Inlet	V_{av}	Flowrate	Angular Speed	K-Factor	Reynolds number
Pa	m/s	m^3/hr	rpm	pulses/ m^3	
5	2,20	59,7	170	2054,3	5370
10	3,34	90,5	279	2223,1	8133
20	4,57	123,7	396	2304,1	11126
60	8,85	239,9	777	2332,9	21571
100	11,55	313,0	1015	2334,7	28144
150	14,09	381,7	1240	2339,6	34315
200	16,50	447,1	1448	2332,0	40201
250	18,36	497,4	1613	2335,0	44721

Table 7.12. Polynomial approximations for different trailing edge shapes for the 12-bladed rotor with the blade pitch angle of 30°

Flat	$-6E-08x^4 + 8E-05x^3 - 0,0351x^2 + 6,8716x + 1994,6$
Curved	$-2E-07x^4 + 0,0002x^3 - 0,0805x^2 + 13,532x + 1519$

Table 7.13. Comparison of results taken for different trailing edge shapes for the 12-bladed rotor with the blade pitch angle of 30°

	Flat	Curved
Average K-factor (p/hr)	2479,8	2335,0
K-factor max. (p/hr)	2492,2	2346,6
K-factor min. (p/hr)	2467,4	2323,3
Q min (m^3/hr)	152,4	138,8
Q max (m^3/hr)	2903,4	3083,6
Turndown ratio	19,1	22,2
Usable range (m^3/hr)	2751,0	2944,8

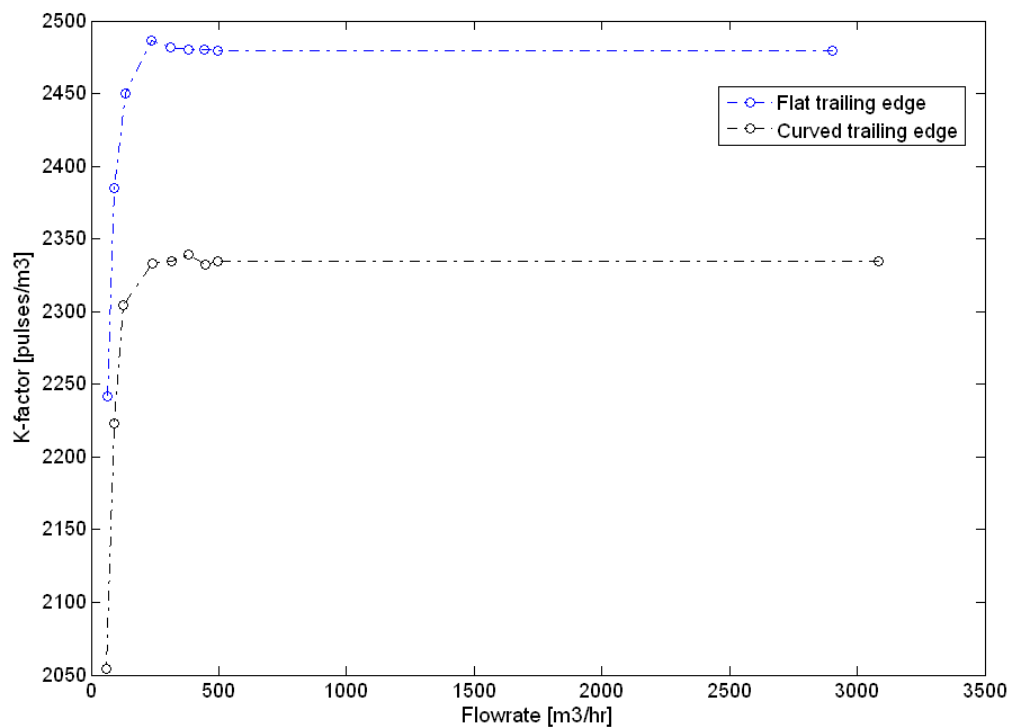


Figure 7.6. The comparison of the flowrate vs. K-factor plots for different trailing edge shapes for the 12-bladed rotor with the blade pitch angle of 30°

Table 7.14. Numerical results taken for a tip clearance of 0.5 mm for the curved trailing edge with 30° blade pitch angle for the 12-bladed rotor

Pressure Inlet	V_{av}	Flowrate	Angular Speed	K-Factor	Reynolds number
Pa	m/s	m^3/hr	rpm	pulses/ m^3	
5	2,29	62,0	192	2235,8	5573
10	3,42	92,7	302	2344,1	8338
20	4,97	134,8	447	2385,4	12119
60	8,83	239,2	793	2386,8	21505
100	11,50	311,7	1031	2381,7	28023
150	14,18	384,2	1268	2375,5	34541
200	16,44	445,5	1468	2371,7	40060
250	18,45	499,8	1644	2367,7	44937

Table 7.15. Numerical results taken for a tip clearance of 2.5 mm for the curved trailing edge with 30° blade pitch angle for the 12-bladed rotor

Pressure Inlet	V_{av}	Flowrate	Angular Speed	K-Factor	Reynolds number
Pa	m/s	m^3/hr	rpm	pulses/ m^3	
5	2,28	61,7	168	1957,5	5549
10	2,86	77,4	229	2131,4	6955
20	4,85	131,3	411	2250,8	11810
60	8,88	240,5	769	2301,2	21623
100	11,59	314,1	1006	2305,7	28241
150	14,19	384,5	1233	2308,8	34567
200	16,57	448,9	1437	2304,6	40358
250	18,52	501,9	1607	2305,1	45126

Table 7.16. Polynomial approximations for different tip clearances for the curved trailing edge with 30° blade pitch angle for the 12-bladed rotor

0.5 mm	$-9E-08x^4 + 1E-04x^3 - 0,0391x^2 + 6,5485x + 2001$
1.5 mm	$-2E-07x^4 + 0,0002x^3 - 0,0805x^2 + 13,532x + 1519$
2.5 mm	$-9E-08x^4 + 0,0001x^3 - 0,0452x^2 + 8,5653x + 1693,6$

Table 7.17. Comparison of results taken for different tip clearances for the curved trailing edge with 30° blade pitch angle for the 12-bladed rotor

	0,5 mm	1,5 mm	2,5 mm
Average K-factor (p/hr)	2367,7	2335,0	2305,1
K-factor max. (p/hr)	2379,5	2346,6	2316,7
K-factor min. (p/hr)	2355,8	2323,3	2293,6
Q min (m^3/hr)	366,7	138,8	189,0
Q max (m^3/hr)	3041,0	3083,6	3123,5
Turndown ratio	8,3	22,2	16,5
Usable range (m^3/hr)	2674,2	2944,8	2934,5

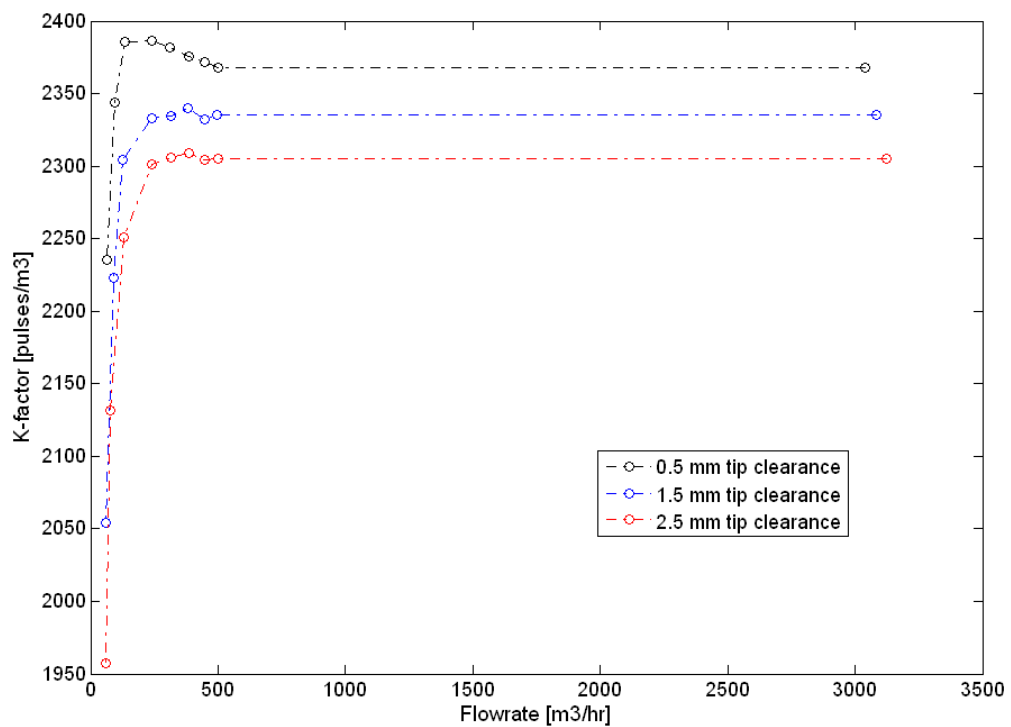


Figure 7.7. The comparison of the flowrate vs. K-factor plots for different tip clearances for the curved trailing edge with 30° blade pitch angle for the 12-bladed rotor

As a result the geometry for the 12-bladed rotor with a blade pitch angle of 30° proved to be the best among the others. If the trailing edge shape is considered, a curved shape and if the tip clearance is considered a tip clearance of 1,5 mm proved to have the maximum flow range among the other geometries. The chosen turbine meter's Reynolds' number vs. K-factor plot is given in Figure 7.8.

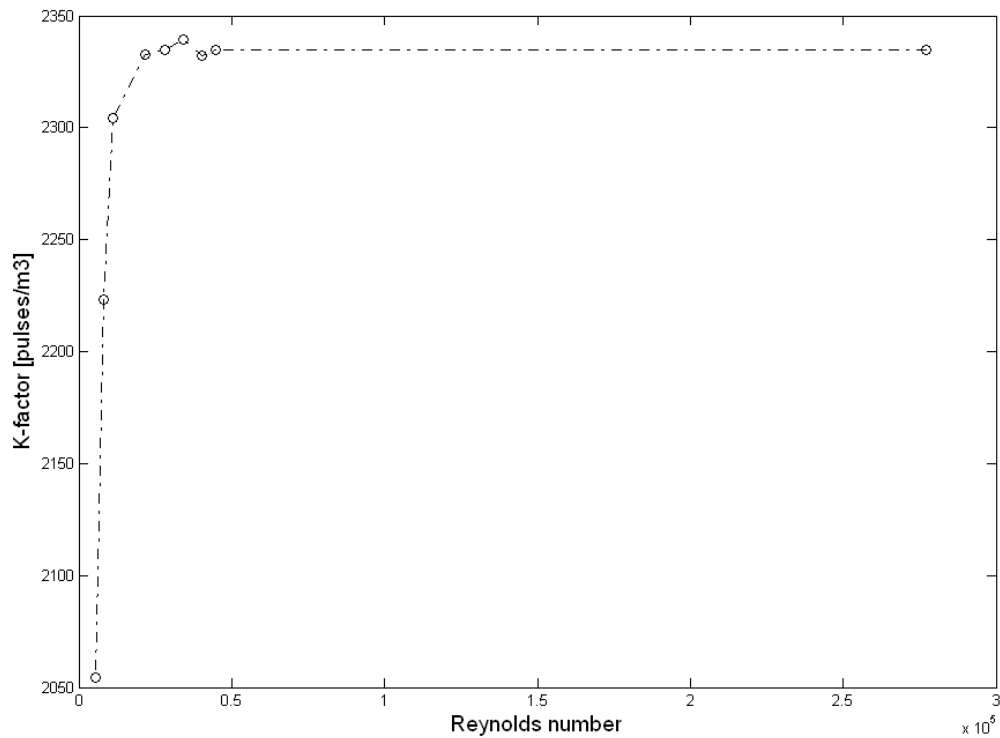


Figure 7.8. The Reynolds' number vs. K-factor plots for the chosen geometry

8. Conclusion

In this study different geometries for the rotor of a turbine meter are tested through numerical simulations in Fluent. Considering the largest flow range the best geometry is picked up among the others. The turbine meter having 12 blades, the blade pitch angle of 30 degrees, tip clearance of 1,5 mm and a curved trailing edge is chosen as the best among the others. It has a maximum flowrate of $3083,6 \text{ m}^3/\text{hr}$ and a minimum flowrate of $138,8 \text{ m}^3/\text{hr}$ with an average K-factor of 2335,0 and a turndown ratio of 22,2. It should be kept in mind that the chosen geometry is the best geometry for the maximum flow range. That's why it has one of the smallest average K-factor among the others. Because of the small K-factor maximum flowrate increases. Other design considerations may also be applied and in such cases this geometry may not be the best one. For example if the flow rate the turbine meter will operate is known, then it could be desired to design for a maximum average K-factor. Bigger K-factor brings about a better sensitivity of the flow such that small flowrates may result in considerable rotational speeds. That also causes the stopping flow and the minimum flow rate to decrease while increasing the pressure drop.

The validation chapter and the design chapter clearly shows that the numerical simulations and the methods used in the simulations result in good agreement with the real cases. The characteristic curve of a single rotor turbine meter gathered from the simulations showed close agreement with the expected curve. Even the hump which results because of the velocity profile of the flow is predicted. The hump could be more clear if more numerical simulation results around that flow rate were taken. The velocity profiles at the inlet shown in the design chapter of the thesis prove the non-uniformity of the velocity profiles for low Reynolds' numbers. If a uniform velocity profile was used as an inlet condition, probably the hump wouldn't form as it is the case when a flow conditioner is used.

An improvement in the grid number is achieved by applying the method described in the design chapter keeping fine enough mesh numbers near the wall regions. This

saves very much time in the solution process. It is clearly shown that the number of meshes used in the model is not important but their distribution for the specified model. The number of meshes greatly effect the computational time and much attention should be paid on the meshing process.

A Matlab user-interface is developed to be used in the study which makes most of the numerical simulations easier and focusing on a GTM design. The capabilities of the Matlab code shows the possibilities of controlling very powerful softwares such as Fluent and Gambit. Creating the desired geometry for the given parameters and meshing it with the least possible mesh number is possible in some minutes by just clicking a button in the interface. The resulting mesh may be solved and post-processed through the same Matlab code. If Fluent and Gambit are present, this user-interface may be easily used in further GTM optimization processes.

8.1. Suggestions for Further Study

The improvement process applied in this study bases on the widest flow range of the turbine meter. The model chosen for the largest flow range can be further improved for some other parameters. The rotor blades can be further improved taking different twisting functions for the least viscous drag forces in the axial direction and the maximum torque in the rotating direction. Another optimization process can be applied by considering an inviscid flow in the turbine meter. An inviscid flow is free of the viscous forces present in the real case. An inviscid flow actually increases the rotational speed of the rotor. In such a case since there is no viscous retarding forces in the model, the response of the turbine meter is very close to linear. The comparison of a viscous flow and inviscid flow may lead to a decision of the best turbine meter among all. It is possible to determine the slip in such a comparison and the minimum slip shows the best turbine meter among all. The closer it is to the ideal case, the better it is in such an improvement process.

As it is already described in the calibration part of chapter 2, K-factor versus Reynolds' number plot is a very common way of describing the turbine meter charac-

teristic for different pressure, temperature and viscosities. A K-factor vs. Reynolds' numbers plot is already presented in the design part of this study by changing the Reynolds' number through different velocities. However in order to prove the Reynolds' number dependence of the chosen turbine meter, it may be possible to make the numerical simulations under different pressure, temperature conditions for different fluids. The results for different operating conditions may be taken to prove the Reynolds' number dependence of the chosen turbine meter.

OptGTM3D is a very useful computer tool in GTM improvement process but there are still things to improve in it. There are some simplifications used in the modeling part of the pre-processor such as ignoring the tolerance values of the real model. This is actually because of the difficulties in meshing process. The program may be further improved into a tool which is able to model exactly the real geometries. One property of the computer tool is that it only considers the rotor part of the turbine meter. By making use of mixing plane model the flow inside the complete turbine meter could be studied. Such an improvement may be used in a study of flow straighteners or conditioners. It should be noted that in such a case realizable k-epsilon model has drawbacks so that another turbulence model should be picked up. One drawback of the simulation process is that in every moment coefficient update interval all the case and data files should be reloaded and every time the interval is over they should be saved. If big mesh files such as 500000 grid elements are considered the time spent for saving and reloading such cases may be of great importance. In order to save the above mentioned time, a user defined function may be written in C such that Fluent adjusts the rotational speed during the iteration process. This may save some time however the more attention should be paid on the mesh sizes in order to have the minimum mesh size that is fine enough for the turbulence model used during the simulations.

Lastly OptGTM3D may be developed into a better one if another section for an analytical guidance dependent on the moment theory is added. If such a guidance exist, better initial guesses could result in less computation which is enough to figure out the characteristics of the turbine meter. Moreover a comparison between the CFD results and the analytical results would exist.

APPENDIX A: Flow Meter Specification Terms

A.1. Accuracy

It is a much-abused term. Manufacturers often default to it for "selling shorthand" but those specifying and buying meters to measure flow should be aware of several caveats [7].

In the first place, no meter is absolutely accurate. there are no absolute standards of gas or liquid against which to compare a meter reading to see how closely that reading compares with what is actually flowing through the meter. Furthermore any statement of accuracy must include not only the best possible estimate of how inaccurate the measurement is but also over what flow range the estimate applies. The more diligent manufacturers usually supply such detailed information. But that is only part of the problem in determining the meter accuracy [7].

A.2. Rangeability

It expresses the flow range over which a meter operates while meeting a stated accuracy tolerance. It is often stated as "turndown" -maximum flow divided by minimum flow over the range. For example: a meter with maximum flow (100%) of 100 gallons per minute and minimum flow (within a stated tolerance such as $\pm 0.5\%$) of 10 gpm has a 10-to-1 rangeability or turndown of 10. It will be accurate $\pm 0.5\%$ from 10 to 100 gpm [7].

The meter may provide a tighter tolerance over a more limited range - say 10-to-1 within $\pm 0.5\%$ of actual flow and 3-to-1 within $\pm 0.25\%$. This means the user can select the tighter tolerance of $\pm 0.25\%$ for a range of 33% to 100% flow (33 to 100 gpm) [7].

A.3. Linearity

It defines how close to a specific accuracy the meter registers over a stated flow range. Its proof curve will approximate a straight line. It may be significantly inaccurate but quite linear [7].

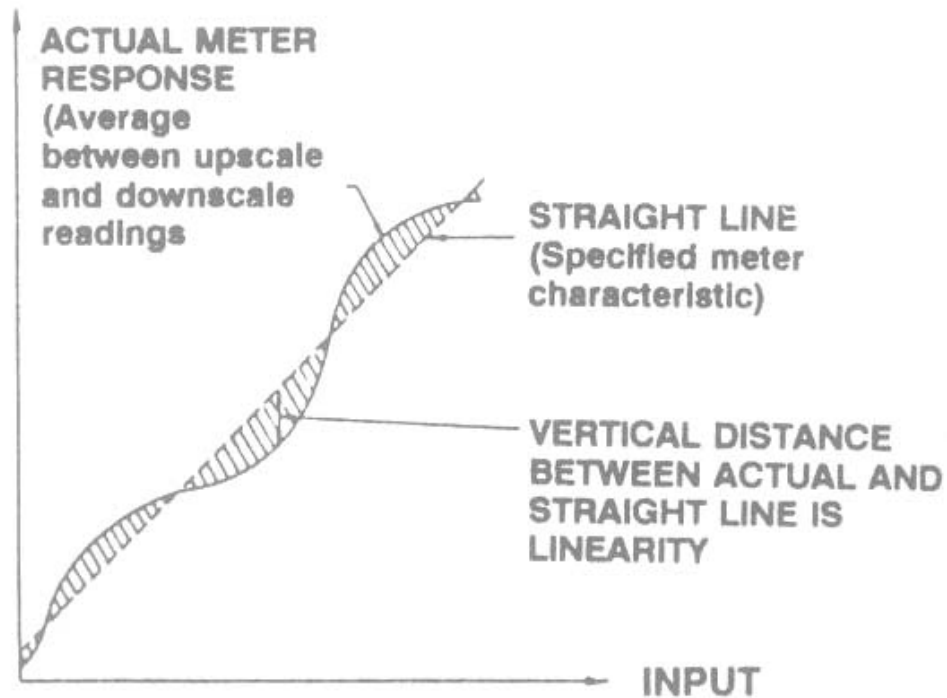


Figure A.1. Linearity error

[7]

It is important to point out that this characteristic was much more important prior to the widespread use of computers and electronic signal-conditioning equipment. With a computer correction device, it is possible to characterize a non-linear meter output curve provided the meter output is repeatable. Such curve characterization allows a closer fit of the readout system- even for a linear meter- to minimize calibration errors. The same procedure is used on "smart" transducers to minimize any non-linearity the transducer may exhibit as a result of temperature and/or pressure effects [7].

A.4. Repeatability

It means just what it says- how nearly the same reading a meter will provide for a given flow condition. As with linearity, it may be more important to always get the same reading for specific flow rates than that those readings be extremely accurate. Flow control is an example of this need [7].

A.5. Hysteresis

It is closely related to repeatability. It describes what happens to meter output as a given flow rate is approached from larger and smaller flow rates. For example suppose a flow rate of 80 gpm is increased to 100 gpm, and a meter then registers 99 gpm. Now the flow rate increases to 120 gpm and returns again to 100 gpm; the meter registers 101 gpm. Its hysteresis is ± 1 gpm, and the dead band is 2 gpm at a 100 gpm flow rate [7].

Consideration of these meter characteristics shows clearly that simply relying on a manufacturer's statement of accuracy is indeed an incomplete and inadequate way to evaluate and compare meters. And, as stated, proper determination and application of accuracy, rangeability, linearity, repeatability, and hysteresis data is basic but still only part of the job in achieving the best flow measurement; operation and maintenance must also be considered [7].

A.6. Meter Factor

It is a correction that mathematically modifies a meter's indication to a corrected "true" reading based on knowledge of the flow and flowing conditions. Corrected readings may be manually calculated periodically or the meter factor automatically applied continuously. It is normally determined from a throughput test, covering the range of flows to be measured, based on a master meter or a prover [7].

APPENDIX B: Discretization in Fluent

Fluent uses a control-volume based solution technique to convert the governing equations to algebraic equations. This control volume technique consists of integrating the governing equations about each control volume, yielding discrete equations that conserve each quantity on a control-volume basis as explained in section CFD. Below, the discretization of the governing equations for the steady-state conservation equation for transport of a scalar quantity is shown. The equation B.1 is written in integral form for an arbitrary control volume as follows:

$$\oint \rho \phi \vec{v} \cdot d\vec{A} = \oint \Gamma_\phi \nabla_\phi \cdot d\vec{A} + \int_V S_\phi dV \quad (\text{B.1})$$

where ρ is density, \vec{v} is velocity vector, \vec{A} is surface area vector, Γ_ϕ is diffusion coefficient for ϕ , ∇_ϕ is gradient of ϕ and S_ϕ is source of ϕ per unit volume. Equation B.1 is applied to each cell in the computational domain. The two-dimensional triangular cell shown in Figure B.1 is an example of such a control volume. Discretization of Equation B.1 on that cell yields

$$\sum_f^{N_{faces}} \rho_f v_f \phi_f \cdot \vec{A}_f = \sum_f^{N_{faces}} \Gamma_\phi (\nabla_\phi)_n \cdot \vec{A}_f + S_\phi V \quad (\text{B.2})$$

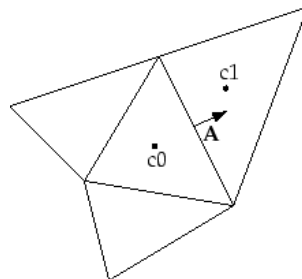


Figure B.1. Control volume used to illustrate discretization of a scalar transport equation [41]

Fluent stores discrete values of the scalar at the cell centers. However, face values are required for the convection terms in Equation B.1 and must be interpolated from the cell center values. This is accomplished using an upwind scheme. FLUENT allows you to choose from several upwind schemes: first-order upwind, second-order upwind, power law, and QUICK. Following is the explanations of first-order upwind and second-order upwind schemes since those are the only ones used in the numerical simulations [41].

B.1. First Order Upwind Scheme

When first-order accuracy is desired, quantities at cell faces are determined by assuming that the cell-center values of any field variable represent a cell-average value and hold throughout the entire cell; the face quantities are identical to the cell quantities. Thus when first-order upwinding is selected, the face value ϕ_f is set equal to the cell-center value of ϕ in the upstream cell [41].

B.2. Second Order Upwind Scheme

When second-order accuracy is desired, second order upwind scheme is used where higher-order accuracy is achieved at cell faces through a Taylor series expansion of the cell-centered solution about the cell centroid. The face value ϕ_f is computed using the following expression:

$$\phi_f = \phi + \nabla_\phi \cdot \Delta \vec{s} \quad (\text{B.3a})$$

$$\nabla_\phi = \frac{1}{V} \sum_f^{N_{faces}} \tilde{\phi}_f \vec{A} \quad (\text{B.3b})$$

where ϕ and ∇_ϕ are the cell-centered value and its gradient in the upstream cell respectively. $\Delta \vec{s}$ is the displacement vector from the upstream cell centroid to the face centroid. This formulation requires the determination of the gradient ∇_ϕ in each cell. This gradient is computed using the divergence theorem, which in discrete form is written as in equation B.3b.

Here the face values $\tilde{\phi}_f$ are computed by averaging ϕ from the two cells adjacent to the face. Finally, the gradient is limited so that no new maxima or minima are introduced [41].

B.3. Under-Relaxation

Because of the nonlinearity of the equation set being solved by FLUENT, it is necessary to control the change of ϕ . This is typically achieved by under-relaxation, which reduces the change of ϕ produced during each iteration. In a simple form, the new value of the variable ϕ within a cell depends upon the old value, ϕ_{old} , the computed change in ϕ , $\Delta\phi$, and the under-relaxation factor, α , as follows:

$$\phi = \phi_{old} + \alpha\Delta\phi \quad (\text{B.4})$$

B.4. Pressure Interpolation Schemes

The default scheme in FLUENT interpolates the pressure values at the faces using momentum equation coefficients. This procedure works well as long as the pressure variation between cell centers is smooth. When there are jumps or large gradients in the momentum source terms between control volumes, the pressure profile has a high gradient at the cell face, and cannot be interpolated using this scheme. If this scheme is used, the discrepancy shows up in overshoots/undershoots of cell velocity.

Flows for which the standard pressure interpolation scheme will have trouble include flows with large body forces, such as in strongly swirling flows, in high-Rayleigh-number natural convection and the like. In such cases, it is necessary to pack the mesh in regions of high gradient to resolve the pressure variation adequately.

Another source of error is that FLUENT assumes that the normal pressure gradient at the wall is zero. This is valid for boundary layers, but not in the presence of body forces or curvature. Again, the failure to correctly account for the wall pressure gradient is manifested in velocity vectors pointing in/out of walls [41].

Several alternate methods are available for cases in which the standard pressure interpolation scheme is not valid:

- The linear scheme computes the face pressure as the average of the pressure values in the adjacent cells.
- The second-order scheme reconstructs the face pressure in the manner used for second-order accurate convection terms . This scheme may provide some improvement over the standard and linear schemes, but it may have some trouble if it is used at the start of a calculation and/or with a bad mesh. The second-order scheme is not applicable for flows with discontinuous pressure gradients imposed by the presence of a porous medium in the domain or mixture model for multiphase flow.
- The body-force-weighted scheme computes the face pressure by assuming that the normal gradient of the difference between pressure and body forces is constant. This works well if the body forces are known a priori in the momentum equations (e.g., buoyancy and axisymmetric swirl calculations).
- The PRESTO! (PREssure STaggering Option) scheme uses the discrete continuity balance for a "staggered" control volume about the face to compute the "staggered" (i.e., face) pressure. This procedure is similar in spirit to the staggered-grid schemes used with structured meshes . Note that for triangular and tetrahedral meshes, comparable accuracy is obtained using a similar algorithm. The PRESTO! scheme is available for all meshes, including but not limited to, tetrahedral, triangular, hexahedral, quadrilateral, and hybrid meshes.

APPENDIX C: Turbulence Modeling in Fluent

The most important characteristic of the turbulent flow is the fluctuating velocity fields. These fluctuations mix transported quantities such as momentum, energy, and species concentration and cause the transported quantities to fluctuate as well. Since these fluctuations can be of small scale and high frequency, they are computationally too expensive to simulate directly in practical engineering cases. Instead of this the governing equations can be time-averaged, ensemble-averaged or changed to remove the small scales so that the modified set of equations are computationally less expensive. These modified equations will contain additional unknown variables and they have to be determined in terms of known quantities [41].

In fluid mechanics no single turbulence model is accepted universally superior for all types of problems. The flow in a pipe, the flow through a turbine or an impeller, an external flow over an airfoil or a hydrofoil can not be simulated with one single model so there are different turbulence models to simulate different cases. [41].

Fluent provides the following turbulence models:

- Spalart-Allmaras model
- $k-\epsilon$ models
 - Standard $k-\epsilon$ model
 - Renormalization-group (RNG) model
 - Realizable $k-\epsilon$ model
- $k-w$ models
 - Standard $k-w$ model
 - Shear-stress Transport (SST) $k-w$ model
- v^2-f model
- Reynolds stress model (RSM)
- Large eddy simulation (LES) model

The standard $k-\epsilon$ model requires more computational effort than the Spalart-Allmaras model since an additional transport equation is solved. The realizable $k-\epsilon$ model requires little more computational effort than the standard $k-\epsilon$ model. Because of the extra terms and functions in the governing equations and a greater degree of non-linearity, the RNG $k-\epsilon$ model takes 10-15% more CPU time than with the standard $k-\epsilon$ model. Like the $k-\epsilon$ models, the $k-w$ models are also two-equation models, and require about the same computational effort [41].

The RSM requires additional memory and CPU time because of the increased number of the transport equations for Reynolds stresses. Usually the RSM in Fluent requires 50-60% more CPU time per iteration compared to the $k-\epsilon$ and $k-w$ models. Moreover, 15-20% more memory is needed [41].

C.1. Reynolds (Ensemble) Averaging

In Reynolds averaging the variables of the Navier-Stokes equations are decomposed into a fluctuating and a mean part. The velocity is decomposed into a mean \bar{u}_i and a fluctuating part u'_i (where $i = 1,2,3$) as follows:

$$u_i = \bar{u}_i + u'_i \quad (\text{C.1})$$

For other scalar quantities the same procedure is applied, as in Equation C.2, where ϕ denotes a scalar such as pressure or energy

$$\phi = \bar{\phi} + \phi' \quad (\text{C.2})$$

Converting the flow variables in instantaneous continuity and momentum equations into this form and taking a time average (yields the drop of overbar on the mean velocity, \bar{u}_i) gives the ensemble-averaged momentum equations. They are written in

Cartesian tensor form as

$$\frac{\partial \rho}{\partial t} + \frac{\partial}{\partial x_i}(\rho u_i) = 0 \quad (\text{C.3})$$

$$\frac{\partial}{\partial t}(\rho u_i) + \frac{\partial}{\partial x_j}(\rho u_i u_j) = -\frac{\partial p}{\partial x_i} + \frac{\partial}{\partial x_j} \left[\mu \left(\frac{\partial u_i}{\partial x_j} + \frac{\partial u_j}{\partial x_i} - \frac{2}{3} \delta_{ij} \frac{\partial u_i}{\partial x_i} \right) \right] + \frac{\partial}{\partial x_j}(-\overline{\rho u'_i u'_j}) \quad (\text{C.4})$$

The equations C.3 and C.4 are called Reynolds-averaged Navier-Stokes (RANS) equations. However, the additional terms appear in Equation C.4 which represent the effect of turbulence. The Reynolds stresses $-\overline{\rho u'_i u'_j}$ should be modeled in order to model turbulence. The Reynolds stresses are related to the mean velocity gradients using the Boussinesq hypothesis [43].

$$-\overline{\rho u'_i u'_j} = \mu_t \left(\frac{\partial u_i}{\partial x_j} + \frac{\partial u_j}{\partial x_i} \right) - \frac{2}{3} \left(\rho k + \mu \frac{\partial u_i}{\partial x_i} \right) \delta_{ij} \quad (\text{C.5})$$

In Spalart-Allmaras model, $k-\epsilon$ models and the $k-w$ models, the Boussinesq hypothesis is used. It needs low computational effort associated with the computation of the turbulent viscosity which makes it favorable. In the case of the $k-\epsilon$ and $k-w$ models, two additional transport equations (for the turbulence kinetic energy, k , and either the turbulence dissipation rate, ϵ or the specific dissipation rate, w) are solved, and μ_t is computed as a function of k and ϵ . The Boussinesq hypothesis assumes μ_t as an isotropic scalar quantity which is not strictly true and a disadvantage for the hypothesis [41].

C.2. The k - ϵ Model

Since it was proposed by Launder and Spalding [44] k - ϵ is very popular in flow simulations with two separate transport equations. Its reasonable accuracy, robustness and economy makes it favorable in engineering community. Besides, it is used in a wide range of applications and it is a general and common model for almost all types of incompressible flows from turbomachinery to pipe flows, external flows and boundary layer flows [41].

C.2.1. The Realizable k - ϵ Model

Since the model satisfies certain mathematical constraints on the Reynolds stresses it is called realizable k - ϵ model. Neither the standard k - ϵ model nor the RNG k - ϵ model is realizable. It provides superior performance for flows involving rotation, boundary layers under strong adverse pressure gradients, separation, and recirculation. The Realizable k - ϵ model differs from the standard k - ϵ model in two points. First, it has a new formulation for the turbulent viscosity. Besides, a new transport equation for the dissipation rate, ϵ , has been derived from an exact equation for the transport of the mean-square vorticity fluctuation [41].

The turbulent viscosity or sometimes called eddy viscosity μ_t is computed by combining k and ϵ as follows:

$$\mu_t = \rho C_\mu \frac{k^2}{\epsilon} \quad (\text{C.6})$$

The combination of the Boussinesq relationship (Equation C.5) and the eddy viscosity definition (Equation C.6) gives the following expression for the normal Reynolds stress in an incompressible strained mean flow

$$\overline{u^2} = \frac{2}{3}k - 2\nu_t \frac{\partial U}{\partial x} \quad (\text{C.7})$$

With the use of Equation C.6 for $\nu_t \equiv \mu_t/\rho$ it is seen that the normal stress, $\overline{u^2}$, becomes negative, which should be positive by definition and now non-realizable, when the strain is large enough to satisfy the relationship

$$\frac{k}{\epsilon} \frac{\partial U}{\partial x} > \frac{1}{3C_\mu} \approx 3.7 \quad (\text{C.8})$$

The Schwarz inequality for shear stresses ($\overline{u_\alpha u_\beta^2} \leq \overline{u_\alpha^2 u_\beta^2}$) can be violated when the mean strain rate is large. The best way to ensure the realizability (positivity of normal stresses and Schwarz inequality for shear stresses) is to make C_μ by sensitizing it to the mean flow and the turbulence. The notion of variable C_μ is suggested by many modelers including Reynolds [45], and is well supported with experimental results.

The realizable k - ϵ model proposed by Shih et al. [46] was intended to address these deficiencies of traditional k - ϵ models by adopting a new eddy-viscosity formula involving a variable C_μ originally proposed by Reynolds [45] and a new model equation for dissipation (ϵ) based on the dynamic equation of the mean-square vorticity fluctuation.

The modeled transport equations for k and ϵ in the realizable k - ϵ model are:

$$\frac{\partial}{\partial t}(\rho k) + \frac{\partial}{\partial x_i}(\rho k u_j) = \frac{\partial}{\partial x_i} \left[\left(\mu + \frac{\mu_t}{\sigma_k} \right) \frac{\partial k}{\partial x_j} \right] + G_k + G_b - \rho \epsilon - Y_M + S_k \quad (\text{C.9})$$

$$\frac{\partial}{\partial t}(\rho \epsilon) + \frac{\partial}{\partial x_j}(\rho \epsilon u_j) = \frac{\partial}{\partial x_j} \left[\left(\mu + \frac{\mu_t}{\sigma_\epsilon} \right) \frac{\partial \epsilon}{\partial x_j} \right] + \rho C_1 S_\epsilon - \rho C_2 \frac{\epsilon^2}{k + \sqrt{\nu \epsilon}} + C_{1\epsilon} \frac{\epsilon}{k} C_{3\epsilon} G_b + S_\epsilon \quad (\text{C.10})$$

$$C_1 = \max \left[0.43, \frac{\eta}{\eta + 5} \right], \quad \eta = S \frac{k}{\epsilon} \quad (\text{C.11})$$

G_k , G_b , μ_t and Y_M are same with the k - ϵ standard model. S_k and S_ϵ are user defined source terms.

The difference between the realizable k - ϵ model is that C_μ is not constant. It is

computed from

$$C_\mu = \frac{1}{A_0 + A_s \frac{kU^*}{\epsilon}} \quad (\text{C.12})$$

where

$$U^* \equiv \sqrt{S_{ij}S_{ij}} + \tilde{\Omega}_{ij}\tilde{\Omega}_{ij} \quad (\text{C.13})$$

and

$$\begin{aligned} \tilde{\Omega}_{ij} &= \Omega_{ij} - 2\epsilon_{ijk}\omega_k \\ \overline{\Omega}_{ij} &= \overline{\Omega}_{ij} - \epsilon_{ijk}\omega_k \end{aligned}$$

where $\overline{\Omega}_{ij}$ is the mean rate-of-rotation tensor viewed in a rotating reference frame with the angular velocity w_k . The model constants A_s and A_0 are given by;

$$A_0 = 4.04, A_s = \sqrt{6} \cos \phi \quad (\text{C.14})$$

and

$$\begin{aligned} \phi &= \frac{1}{3} \cos^{-1}(\sqrt{6}W, W = \frac{S_{ij}S_{jk}S_{ki}}{\tilde{S}}, \tilde{S} = \sqrt{S_{ij}S_{ij}}, S_{ij} = \frac{1}{2} \left(\frac{\partial u_j}{\partial x_i} + \frac{\partial u_i}{\partial x_j} \right) \\ C_{1\epsilon} &= 1.44, C_2 = 1.9, \sigma_k = 1.0, \sigma_\epsilon = 1.2 \end{aligned}$$

C.3. Wall Treatment

C.3.1. Standard Wall Functions

One of the most widely used method of wall treatment for industrial flows is standard wall functions which are based on the proposal of Launder and Spalding. Standard wall functions work reasonably well for a wide range of wall bounded flows, but if the flow begins to diverge from ideal conditions (i.e. strong adverse pressure gradients) the accuracy of their predictions begin to degrade [41].

The law of the wall for mean velocity gives

$$U^* = \frac{1}{\kappa} \ln(Ey^*) \quad (\text{C.15})$$

where

$$U^* \equiv \frac{U_p C_\mu^{0.25} k_p^{0.5}}{\tau_w / \rho} \quad (\text{C.16})$$

$$y^* \equiv \frac{\rho C_\mu^{0.25} k_p^{0.5} y}{\mu} \quad (\text{C.17})$$

C.3.2. Non-Equilibrium Wall Functions

The non-equilibrium wall function is two layer based and sensitized to the pressure gradient effects. In order to compute the budget of turbulence kinetic energy in wall neighboring cells the two layer based concept is adopted. Briefly, the non-equilibrium wall functions extend the applicability of the wall function approach by including the effects of pressure gradient and strong non-equilibrium.

The log-law for mean velocity sensitized to pressure gradients is

$$\frac{\tilde{U} C_\mu^{0.25} k^{0.5}}{\tau_w / \rho} = \frac{1}{\kappa} \ln \left(E \frac{\rho C_\mu^{0.25} k^{0.5} y}{\mu} \right) \quad (\text{C.18})$$

where

$$\tilde{U} = U - \frac{1}{2} \frac{dp}{dx} \left[\frac{y_v}{\rho \kappa \sqrt{k}} \ln \left(\frac{y}{y_v} \right) + \frac{y - y_v}{\rho \kappa \sqrt{k}} + \frac{Y_v^2}{\mu} \right] \quad (\text{C.19})$$

$$y_v \equiv \frac{\mu y_v^*}{\rho C_\mu^{0.25} k_p^{0.5}}$$

where y_v is the physical sublayer thickness and $y_v^* = 11.225$.

C.3.3. Enhanced Wall Treatment

As the third and last option of near-wall modeling methods in Fluent enhanced wall treatment combines a two-layer model with enhanced wall functions. When the near-wall mesh is fine enough to be able to resolve the laminar sublayer or in other words $y^+ = 1$, the enhanced wall treatment will be identical to the traditional two-layer zonal model. In order to apply the model the viscosity-affected near-wall region should be completely resolved all the way to the viscous sublayer.

The two-layer approach is an integral part of the enhanced wall treatment and is used to specify both and the turbulent viscosity in the near-wall cells. Achieving this is done by division of the whole domain into a viscosity-affected region and a fully-turbulent region. The borderline of the two regions is determined by a wall-distance-based Re number which is given as

$$Re_y \equiv \frac{\rho y \sqrt{k}}{\mu} \quad (\text{C.20})$$

When the enhanced wall treatment method is used Fluent changes the way of estimation of turbulent viscosity and length scale according to the two layer model. Detailed explanation can be found in literature [41].

REFERENCES

1. International Energy Outlook 2005, Web adress:
www.eia.doe.gov/oiaf/ieo/nat_gas.html
2. Cascetta F., Scalabrini G., Flow Measurement and Instrumentation 10, (1998)
p.183-188
3. Mantilla J., Dijstelbergen H. H. and Bar H. and Rouwe J. D.; Transcanada
Calibrations High Volume High Pressure Gas Meter Testing Station; Presented
at the June 05-08, C.G.A. 2000 Gas Measurement School in Regina, SK.
4. Petrol Hatları ile Petrol Taşıma A.Ş. , Web adress: www.botas.gov.tr
5. Spitzer, D.W. (editor) (1991): "Flow measurement: practical guides for
measurement and control", Instrument Society of America, United States of
America.
6. Medlock, R.S., "Flow Measurement Special Issue," Measurement Control, June
1986.
7. Upp, E.L. (1993): "Fluid flow measurement: a practical guide to accurate flow
measurement", Daniel Industries, Gulf Publishing Company, Houston, Texas.
8. Baker, Roger C. (1991): "Turbine and related flowmeters: 1. Industrial
practice", Review, Flow Measurement and Instrumentation, Vol.2, July 1991.
9. Schieber, Richard H., Gas Turbine Meters: Evolutionary Changes Extend
Capacity Ratings, Cut O and M Costs, Pipeline and Gas Journal, July 1997.
10. Hardy, Jim Hylton, Jim O., McKnight, Tim E., Remenyik, Carl J. Ruppel,
Francis R. (1999): "Flow measurement methods and applications",
Wiley-Interscience Publication, New York.

11. Flowmeters; Catagorization, Web adress:
www.efunda.com/DesignStandards/sensors/flowmeters/flowmeter_cat.cfm
12. Wadlow, David: "Turbine flowmeters", Web adress:
www.sensors-research.com/articles/turbines.htm
13. Skaperdas E., Divinis N. and Karapantsios T. D.; 3D Transient Simulation of a Rotating Paddlewheel Flow Meter, Southeastern Europe Fluent Users Group Meeting 2002, Thessaloniki, Greece
14. Turbine Gas Meter Handbook, Web adress:
www.instromet.com/Downloads/Default.aspx
15. Turbine Gas Meter Q-Series, Web adress:
www.instromet.com/Downloads/Default.aspx
16. Wadlow, David (1999): "Turbine flowmeters: Details of the basic axial turbine flowmeter", Sensors Magazine Online, October 1999, Web adress:
www.sensorsmag.com/articles/1099/16/main.shtml
17. Universal Viscosity Curve Theory, Web adress:
www.ftimeters.com/pages/uvc.html
18. Martin Cuthbert MEng (Hons), Webster Products Ltd., A Recent Development in Flow Linearisation, Web adress:
www.webster-inst.com/techinfo/techrep/viscorr/viscorfr/visco1.htm
19. Alan Ranseth, Reynolds Number Calibration of Turbine Meters, Web adress:
<http://www.cga.ca/events/documents/ransethalan.pdf>
20. Cheremisinoff, Nicholas P. (1979): "Applied Fluid Flow Measurement: Fundamentals and Technology", Marcel Dekker Inc, New York.

21. Baker, Roger C. (1989): "An introductory guide to flow measurement", Mechanical Engineering Publications Limited, London. Flow
22. Flow Conditioning for Natural Gas Measurement, Web address:
www.flowmeterdirectory.com/flowmeter_artc/flowmeter_artc_04031102.html
23. Baker, Roger C. (1993): "Turbine flowmeters: II. Theoretical and Experimental published information", Flow Measurement and Instrumentation, Vol.4, 1993.
24. Daniel,Peace W. (1995): "Turbine meters: Proper Installation ensures Turbine Meter Accueacy", Pipeline and Gas Journal, July, 1995.
25. Munson B.R., Young D.F. and Okiishi T.H., Fundamentals of Fluid Mechanics 3rd edt., John Wiley, 1998.
26. Sancı, Selim,Design of a torpedo: Study of drag reduction using computational fluid dynamics, M.S. Thesis, Bogazici University Mechanical Engineering, 2005.
27. Secondary Flow Research at the University of Durham, Secondary Flow, Web address: www.dur.ac.uk/secondary.flow/secondaryflow.html
28. Introduction to Aerodynamics, Web address:
www.rmcs.cranfield.ac.uk/aeroxtra/dtcdragcomp2.htm
29. Andrew A. McCarter, Budugur Lakshminarayana, Xinwen Xiao, Tip Clearance Effects in a Turbine Rotor: Part IIVelocity Field and Flow Physics, Journal of Turbomachinary, Vol.123, April 2001.
30. Appel D.W. and others, Hunter Rouse (editor), Advanced Mechanics of Fluids New York : Wiley, 1959.
31. Swanson W. M., Fluid Mechanics, New York : Holt, Rinehart, and Winston 1970.

32. Fluid Dynamics and the Navier-Stokes Equations, Web address:
<http://universe-review.ca/R13-10-NSeqs.htm>
33. Blazek J., Computational Fluid Dynamics: Principles and Applications, Amsterdam ; New York : Elsevier, 2001.
34. Computational Fluid Dynamics, Web address:
<http://www.lrr.in.tum.de/Par/appls/apps/cfd.html>
35. Lee W. F. Z. and Evans H. J., Density effect and Reynolds number effect on gas turbine flowmeters, Trans. ASME, J. Basic Eng., 1987
36. Thompson R. E., and Grey J., Turbine flowmeter performance model, Trans. ASME, J. Basic Eng., 1992
37. Tsukamoto, H. and Hutton, S. P. Theoretical prediction of meter factor for a helical turbine flowmeter, Conference on Fluid Control and Measurement, Tokyo, Japan, September 1985
38. Pate M. B. , Myklebust A., and Cole J. H., A computer simulation of the turbine flow meter rotor as a drag body, Proc. Int. Comput. in Eng. Conf. and Exhibit 1984, Las Vegas: 184-191, NY, NY: ASME, 1984.
39. Hoffman Klaus A., Chiang Steve T., Computational Fluid Dynamics for Engineers Volume II, Wichita, Kansas : Engineering Education System, 1993.
40. Introduction to Computational Fluid Dynamics, Web address:
http://css.engineering.uiowa.edu/fluids/Lab/CFD_lecture_2004.ppt
41. Documentation of fluent 6.1.22 CFD software
42. Islam M., Hasana M.M., Singh S.N., Seshardi V., "The effect of swirl on a turbine meter in air flow and the effectiveness of a flow straightener in removing the swirl", Journal of Instrument Society India , 33 (4)

43. Hinze J.O., Turbulence, McGraw-Hill Publishing Co. New York, 1975.
44. Launder B.E. and Spalding D.B., Lectures in Mathematical Models of Turbulence, Academic Press London, 1972.
45. Reynolds W. C. Fundamentals of turbulence for turbulence modeling and simulation. Lecture Notes for Von Karman Institute Agard, Report No.755, 1987.
46. Shih T.-H., Liou W. W., Shabbir A., Yang Z., and Zhu J. A New Eddy-Viscosity Model for High Reynolds Number Turbulent Flows Model Development and Validation, Computers Fluids, Vol.24, p.227-238, 1995.